

---

Electronic Thesis and Dissertation Repository

---

8-20-2015 12:00 AM

## In Situ High-Pressure Study of Metal-Organic Frameworks and Their Performance for CO<sub>2</sub> Storage Probed by Vibrational Spectroscopy

Yue Hu

*The University of Western Ontario*

Supervisor

Yining Huang

*The University of Western Ontario* Joint Supervisor

Yang Song

*The University of Western Ontario*

Graduate Program in Chemistry

A thesis submitted in partial fulfillment of the requirements for the degree in Doctor of Philosophy

© Yue Hu 2015

Follow this and additional works at: <https://ir.lib.uwo.ca/etd>



Part of the [Inorganic Chemistry Commons](#), [Materials Chemistry Commons](#), and the [Physical Chemistry Commons](#)

---

### Recommended Citation

Hu, Yue, "In Situ High-Pressure Study of Metal-Organic Frameworks and Their Performance for CO<sub>2</sub> Storage Probed by Vibrational Spectroscopy" (2015). *Electronic Thesis and Dissertation Repository*. 3090. <https://ir.lib.uwo.ca/etd/3090>

This Dissertation/Thesis is brought to you for free and open access by Scholarship@Western. It has been accepted for inclusion in Electronic Thesis and Dissertation Repository by an authorized administrator of Scholarship@Western. For more information, please contact [wlsadmin@uwo.ca](mailto:wlsadmin@uwo.ca).

*IN SITU* HIGH-PRESSURE STUDY OF METAL-ORGANIC FRAMEWORKS AND  
THEIR PERFORMANCE FOR CO<sub>2</sub> STORAGE PROBED BY VIBRATIONAL  
SPECTROSCOPY

(Thesis format: Integrated Article)

by

Yue Hu

Graduate Program in Chemistry

A thesis submitted in partial fulfillment  
of the requirements for the degree of  
Doctor of Philosophy

The School of Graduate and Postdoctoral Studies  
The University of Western Ontario  
London, Ontario, Canada

© Yue Hu 2015

## Abstract

Metal-organic frameworks (MOFs) are an important class of porous materials, owing to their potential applications in a variety of areas, including gas storage, molecular separations, catalysis, sensors and so on. Most importantly, their large surface areas, tunable pore properties and potential for industrial scale production have made MOFs a promising material for clean energy applications, such as CO<sub>2</sub> storage. The chemical and mechanical stabilities of MOFs play a crucial role in their CO<sub>2</sub> storage performance, which require extreme loading pressures that are far beyond ambient pressure at times. Application of high external pressure (e.g., in gigapascal range) on MOFs can significantly alter the framework structure, pore opening and consequently the adsorption properties. This Ph.D. work focuses on the investigation of high-pressure effects on the structure and CO<sub>2</sub> adsorptive performance of MOFs. *In situ* vibrational spectroscopy was used as a primary characterization method, which allows the understanding of local structures, chemical bonding, and thus the nature of guest-host interactions between the adsorbed molecules and the framework.

Four types of MOFs with different topologies, structures and porosities have been studied under high pressures. First, we showed that ZIF-8 (ZIF = zeolitic imidazolate frameworks), a MOF with small pore size, exhibited an unusual chemical stability under extreme compression. Structural modifications were found to be reversible in a low-pressure region, but irreversible in a high-pressure region. The IR profile of CO<sub>2</sub> loaded ZIF-8 on compression provided direct evidence of the strong interactions between CO<sub>2</sub> and ZIF-8, indicating enhanced CO<sub>2</sub> storage in the framework. The flexibility of the organic linker played an important role in the CO<sub>2</sub> adsorption of ZIF-8. MIL-68(In) (MIL = Matériaux de l'Institut Lavoisier) features two types of channels with distinct pore sizes and was the next

MOF studied. The pressure-induced structural modifications in MIL-68(In) were found to be reversible for the as-made framework but irreversible for the activated framework. When loaded with CO<sub>2</sub>, the framework exhibited interesting differential binding affinities with CO<sub>2</sub> at different pressures via the hexagonal and triangular pores. The pressure enhanced CO<sub>2</sub> storage behavior and the guest-host interaction mechanism between CO<sub>2</sub> and MIL-68(In) were explored with the aid of Monte Carlo simulations. Following this, the performance of  $\alpha$ -magnesium formate [ $\alpha$ -Mg<sub>3</sub>(HCOO)<sub>6</sub>], a representative lightweight Mg-based MOF for CO<sub>2</sub> adsorption under high pressure, was investigated. Highly ordered CO<sub>2</sub> molecules were found to be aligned within the pores of  $\alpha$ -Mg<sub>3</sub>(HCOO)<sub>6</sub> due to the strong pressure-induced interactions with the formate ligand. Furthermore, a highly robust calcium-based MOF named CaSDB (SDB = 4, 4'-sulfonyldibenzoate) demonstrated high affinity towards CO<sub>2</sub> at high pressures. Additional adsorption sites were found at elevated pressures, including an interaction site on the metal center. A CO<sub>2</sub> adsorption-driven phase transition was also observed for the framework upon compression. This work demonstrates great potential for MOF-based greenhouse gas storage applications.

## Keywords

Metal-organic frameworks, high pressure, diamond anvil cell, vibrational spectroscopy, infrared spectroscopy, Raman spectroscopy, framework stability, reversibility, CO<sub>2</sub> storage, CO<sub>2</sub> adsorption site, guest-host interaction, pressure-induced phase transition, amorphization.

## Co-Authorship Statement

The following thesis contains materials from previously published manuscripts authored by Yue Hu and co-authored or edited by others mentioned below. Dr. Yining Huang and Dr. Yang Song were the corresponding authors on all the presented papers and were responsible for the supervision of Yue Hu over the course of his Ph.D. study. Both of them played a major role in the editing and revision of the materials presented in all chapters. For copyright releases see the Appendix.

*Chapter 2* is from the published communication authored by Yue Hu, Hossein Kazemian, Sohrab Rohani, Yining Huang and Yang Song (*Chemical Communications*, **2011**, 47, 12694). The majority of *Chapter 3* is from the publication authored by Yue Hu, Zhenxian Liu, Jun Xu, Yining Huang and Yang Song (*Journal of the American Chemical Society* **2013**, 135, 9287).

The ZIF-8 samples used in *Chapters 2* and *3* were supplied by Dr. Hossein Kazemian in Prof. Sohrab Rohani's group in the Department of Chemical and Biochemical Engineering. The samples of MIL-68 (In) in *Chapter 4*,  $\alpha$ -Mg<sub>3</sub>(HCOO)<sub>6</sub> in *Chapter 5* and CaSDB in *Chapter 6* were synthesized by Peng He, Yuanjun Lu and Shoushun Chen in Dr. Huang's group, respectively.

Yue Hu is responsible for a majority of the sample preparation in diamond anvil cell and data collection. All the mid-IR and Raman measurements were performed by Yue Hu in Dr. Song's lab, with the exception of the CO<sub>2</sub> loading with  $\alpha$ -Mg<sub>3</sub>(HCOO)<sub>6</sub> and their mid-IR measurements, which were completed by undergraduate student Ruilin Liang under the

supervision of Yue Hu. The far-IR data were collected by Yue Hu at National Synchrotron Light Source (NSLS) with the help of beamline scientist Dr. Zhenxian Liu.

All data analysis was done by Yue Hu except for the Grand Canonical Monte Carlo simulations in *Chapter 4*, which was performed by Bin Lin in Dr. Youyong Li's group at Soochow University.

*To my loving family*

## Acknowledgments

First and foremost, I would like to thank my two advisors, Dr. Yining Huang and Dr. Yang Song, for their patient guidance, inspiring advice and constant encouragement, without which the finish of my Ph.D. study would not have been possible. I am truly grateful to study and work under the supervision of two tremendous mentors who embody the valuable qualities of scientists: curiosity, enthusiasm, patience and dedication to work. Their strong work ethic will always inspire and impact me for the rest of my life.

I would also like to thank the members of my thesis examination board: Dr. Zhifeng Ding, Dr. François Lagugné-Labarthe, Dr. Paul Charpentier (Department of Chemical & Biomedical Engineering) and Dr. Tomislav Frišćić (McGill University) for their time. I would like to acknowledge Dr. Nicholas Payne, Dr T. K. Sham, Dr. Lyudmila Goncharova and Dr. Xueliang Sun for their excellent graduate courses. In addition, I appreciate all the input from my collaborators and synchrotron beamline scientists: Dr. Hossein Kazemian, Dr. Sohrab Rohani, Dr. Youyong Li (Soochow University) and Dr. Zhenxian Liu (NSLS). Their help and technical support have been much needed for the fulfilment of my degree.

It has been a privilege to work with my past and present colleagues in both Dr. Huang and Song's lab: Dr. Jun Xu, Dr. Lu Zhang, Dr. Margaret Hanson, Tetyana Levchenko, Adam Macintosh, Donghan Chen, Zheng (Sonia) Lin, Le Xu, Peng He, Maxwell Goldman, Dr. Wei Wang, Dr. Haiyan Mao, Dr. Farhana Gul-E-Noor, Balsam Ibrahim, Regina Sinelnikov, Dr. Bryan Lucier, Yuanjun Lu, Shoushun Chen, Yue Zhang, Xuzhao Zhao, Scott Truman, Dr. Zhaohui Dong, Ang Liu, Kamila Bladdek, Dr. Vinod Panchal, Ankang Zhao, Liang Zhou, Zhihao Yu, Ruilin Liang, Shan Jiang, Jiwen Guan, Fengping Xiao and Nilesh Shinde. I appreciate their friendly help, which makes my research smooth and life in the lab joyful.



Besides, the staff of the department are acknowledged: Darlene McDonald, Clara Fernandes, Anna Vandendries-Barr, Barakat Misk, John Vanstone, Jon Aukema and Monica Chirigel. I would also like to extend my gratitude to all my friends at Western: Xiaoxuan Guo, Yu Sun, Linda Wu, Zhiqiang Wang, Ruiping Ge, Lijia Liu, Jing Chao, Jia Jia, Jing Zhang, Ting Li, Ming Huang, Yiyi Liu, Fuyan Zhao, Dong Zhao, Jian Chen, Jiacheng Guo, Jun Li, Bo Fan, Nazhen Liu, Renjie Hou, Xiaoxiao Wang, Jinqiang Hou, Dan Guo and Kyle Jeffs.

Most importantly, I would like to thank my beloved parents for their love, encouragement and unconditional support during my graduate studies. My girlfriend Ziqing Ye deserves a special thanks for always sharing my troubles as well as joys, and going through everything together with me. Without her love and understanding, it would have been not possible to finish my Ph.D. program.

# Table of Contents

Abstract.....	ii
Co-Authorship Statement.....	iv
Acknowledgments.....	vii
Table of Contents.....	ix
List of Tables.....	xiii
List of Figures.....	xv
List of Abbreviations.....	xxi
Chapter 1.....	1
1 Introduction.....	1
1.1 Metal-organic frameworks.....	1
1.1.1 Structures of metal-organic frameworks.....	1
1.1.2 CO <sub>2</sub> storage in metal-organic frameworks.....	2
1.2 High-pressure science and technology.....	8
1.2.1 High-pressure phenomena.....	8
1.2.2 Diamond anvil cell.....	9
1.2.3 <i>In situ</i> high-pressure characterizations.....	12
1.2.4 IR and Raman spectra of CO <sub>2</sub> at high pressures.....	16
1.3 High-pressure effects on MOFs.....	18
1.3.1 Unusual elastic responses.....	19
1.3.2 Phase transitions.....	21
1.3.3 Chemical reactions.....	23
1.3.4 High-pressure guest insertion.....	24
1.4 Outline of the thesis.....	26
1.5 Reference.....	27

Chapter 2.....	34
2 <i>In Situ</i> High Pressure Study of ZIF-8 by IR Spectroscopy .....	34
2.1 Introduction.....	34
2.2 Experimental section.....	36
2.3 Results.....	37
2.3.1 IR spectra of ZIF-8 upon compression to 39 GPa.....	37
2.3.2 IR spectra of ZIF-8 upon compression to 1.6 GPa.....	40
2.4 Discussion .....	40
2.5 Conclusions .....	43
2.6 References .....	44
Chapter 3.....	46
3 Evidence of Pressure Enhanced CO <sub>2</sub> Storage in ZIF-8 Probed by FTIR Spectroscopy .....	46
3.1 Introduction.....	46
3.2 Experimental section.....	47
3.3 Results.....	48
3.3.1 IR spectrum of ZIF-8 loaded with CO <sub>2</sub> at 0.78 GPa.....	48
3.3.2 IR spectra of ZIF-8 loaded with CO <sub>2</sub> upon compression and decompression ....	52
3.4 Discussion .....	54
3.5 Conclusions .....	61
3.6 References .....	61
Chapter 4.....	63
4 The Structural Stability of and Enhanced CO <sub>2</sub> Storage in MOF MIL-68(In) under High Pressures Probed by FTIR Spectroscopy .....	63
4.1 Introduction.....	63
4.2 Experimental section.....	66
4.3 Results.....	68

4.3.1 IR spectra of as-made and activated MIL-68(In) at ambient pressure .....	68
4.3.2 IR spectra of as-made MIL-68(In) upon compression .....	72
4.3.3 IR spectra of activated MIL-68(In) upon compression .....	77
4.3.4 IR spectra of activated MIL-68(In) with PTM upon compression .....	82
4.3.5 IR spectra of activated MIL-68(In) loaded with CO <sub>2</sub> upon compression .....	87
4.4 Discussion .....	93
4.5 Conclusions .....	98
4.6 Reference .....	99
Chapter 5 .....	103
5 High Pressure Study of CO <sub>2</sub> Adsorption in MOF $\alpha$ -Mg <sub>3</sub> (HCOO) <sub>6</sub> by Vibrational Spectroscopy .....	103
5.1 Introduction .....	103
5.2 Experimental section .....	105
5.3 Results .....	106
5.3.1 IR and Raman spectra of $\alpha$ -Mg <sub>3</sub> (HCOO) <sub>6</sub> loaded with CO <sub>2</sub> .....	106
5.3.2 Mid-IR spectra of $\alpha$ -Mg <sub>3</sub> (HCOO) <sub>6</sub> loaded with CO <sub>2</sub> at high pressures .....	109
5.3.3 Raman and far-IR spectra of $\alpha$ -Mg <sub>3</sub> (HCOO) <sub>6</sub> loaded with CO <sub>2</sub> at high pressures .....	112
5.4 Discussion .....	116
5.5 Conclusions .....	124
5.6 Reference .....	124
Chapter 6 .....	127
6 Exploring the Remarkable Affinity of MOF CaSDB towards CO <sub>2</sub> at Extreme Pressure .....	127
6.1 Introduction .....	127
6.2 Experimental section .....	130
6.3 Results .....	131

6.3.1 IR and Raman spectra of activated CaSDB at ambient pressure .....	131
6.3.2 IR and Raman spectra of activated CaSDB at high pressures .....	133
6.3.3 IR spectra of CaSDB loaded with CO <sub>2</sub> at 0.39 GPa .....	139
6.3.4 IR and Raman spectra of CaSDB loaded with CO <sub>2</sub> at high pressures .....	141
6.4 Discussion .....	150
6.5 Conclusions .....	155
6.6 Reference.....	155
Chapter 7.....	159
7 Summary and Future Work.....	159
7.1 Summary .....	159
7.2 Suggestions for future work.....	161
Appendices: Copyright Permission.....	162
Curriculum Vitae .....	164

## List of Tables

Table 2-1. Pressure dependence ( $dv/dP$ , $\text{cm}^{-1}/\text{GPa}$ ) of IR modes of ZIF-8 on compression..	42
Table 3-1. Pressure dependence ( $dv/dP$ , $\text{cm}^{-1}/\text{GPa}$ ) of IR modes of $\text{CO}_2$ loaded ZIF-8 from 0 to 2.65 GPa.....	60
Table 4-1. Assignments for selected IR modes ( $\text{cm}^{-1}$ ) of MIL-68(In) at ambient pressure....	71
Table 4-2. Pressure dependence ( $dv/dP$ , $\text{cm}^{-1} \text{ GPa}^{-1}$ ) of IR modes of as-made MIL-68(In) from 0 to 9 GPa.....	76
Table 4-3. Pressure dependence ( $dv/dP$ , $\text{cm}^{-1} \text{ GPa}^{-1}$ ) of IR modes of activated MIL-68(In) from 0 to 9 GPa.....	81
Table 4-4. Pressure dependence ( $dv/dP$ , $\text{cm}^{-1} \text{ GPa}^{-1}$ ) of IR modes of activated MIL-68(In) with PTM from 0 to 18 GPa. ....	86
Table 4-5. Pressure dependence ( $dv/dP$ , $\text{cm}^{-1} \text{ GPa}^{-1}$ ) of the combination modes of $\text{CO}_2$ and the OH stretch mode of MIL-68(In) from 0.42 to 1.88 GPa.....	92
Table 5-1. Pressure dependences [ $dv/dP$ ( $\text{cm}^{-1} \cdot \text{GPa}^{-1}$ )] of the selected IR bands of $\alpha$ - $\text{Mg}_3(\text{HCOO})_6$ loaded with $\text{CO}_2$ on compression .....	118
Table 5-2. Pressure dependences [ $dv/dP$ ( $\text{cm}^{-1} \cdot \text{GPa}^{-1}$ )] of the selected Raman bands of $\alpha$ - $\text{Mg}_3(\text{HCOO})_6$ loaded with $\text{CO}_2$ on compression .....	119
Table 6-1. Pressure dependence ( $dv/dP$ , $\text{cm}^{-1} \text{ GPa}^{-1}$ ) of selected IR modes of CaSDB from ambient to 11 GPa.....	138
Table 6-2. Pressure dependence ( $dv/dP$ , $\text{cm}^{-1} \text{ GPa}^{-1}$ ) of selected Raman modes of CaSDB from ambient to 11 GPa.....	138
Table 6-3. Pressure dependence ( $dv/dP$ , $\text{cm}^{-1} \text{ GPa}^{-1}$ ) of selected IR modes of CaSDB loaded with $\text{CO}_2$ from 0.24 to 13.6 GPa.....	147

Table 6-4. Pressure dependence ( $dv/dP$ ,  $\text{cm}^{-1} \cdot \text{GPa}^{-1}$ ) of selected Raman modes of CaSDB loaded with  $\text{CO}_2$  from 0.24 to 13.6 GPa. .... 149

# List of Figures

Figure 1-1. (a) The building units and structure of MOF-5; (b) Isoreticular MOFs of MOF-5. (ref. 1, 2) ..... 2

Figure 1-2. The crystal structure of MOF-177 and comparison of the gravimetric and volumetric CO<sub>2</sub> capacity for several MOFs and other porous materials. (ref. 31) ..... 4

Figure 1-3. (a) Functionalization of Cu-BTTri through binding N,N'-dimethylethylenediamine (mmen) to the metal coordination sites; (b) the CO<sub>2</sub> (square) and N<sub>2</sub> (circle) adsorption isotherms for mmen-Cu-BTTri (green) and Cu-BTTri (blue) at 298 K. (ref. 37) ..... 5

Figure 1-4. (a) View of 1D channel of the structure of MOF M<sub>2</sub>(dobdc) adsorbed with CO<sub>2</sub>; (b) CO<sub>2</sub> sorption isotherm (296 K, 0 to 1 atm) of the MOF M<sub>2</sub>(dobdc) series. (ref. 54)..... 7

Figure 1-5. Examples of various high-pressure phenomena. (ref. 57)..... 9

Figure 1-6. Opposed diamond anvil configuration, with a metal gasket for sample confinement..... 10

Figure 1-7. Ruby R<sub>1</sub> fluorescence spectra at 0 GPa (in black) and 4.9 GPa (in red) under room temperature. .... 11

Figure 1-8. Schematic diagram of the IR micro-spectroscopy system, with major optical components labeled. (ref. 65)..... 14

Figure 1-9. Schematic of the Raman system. BPF: band path filter; IRIS: IRIS aperture; M1-7: broadband dielectric reflecting mirrors; FW1A: Six station filter wheel; BS: beam splitter; NF: notch filter; DAC: diamond anvil cell; Triple gratings: 300 lines/mm, 1200 lines/mm, and 1800 lines/mm. (ref. 66)..... 15

Figure 1-10. (a) CO<sub>2</sub> phase diagram (ref. 68); (b) IR spectrum of liquid CO<sub>2</sub> at 0.4 GPa; Raman spectrum of CO<sub>2</sub> (c) at 0.4 GPa and (d) at 1.0 GPa in the lattice region. (ref. 70)..... 17



Figure 1-11. Evolution of the cell volume (top) and lattice parameters (bottom) of MIL-53(Al) with increasing pressure. (ref. 83).....	20
Figure 1-12. Phase transitions of Zn(CN) <sub>2</sub> upon compression in different fluid media. (ref. 91) .....	22
Figure 1-13. Pressure-induced proton jump in ZAG-4 and ZAG-6. (ref. 98) .....	24
Figure 1-14. (a) Unit cell volume of Sc <sub>2</sub> BDC <sub>3</sub> in methanol and Fluorinert as a function of pressure; (b) pressure-induced methanol insertion in Sc <sub>2</sub> BDC <sub>3</sub> . (ref. 105) .....	26
Figure 2-1. Crystal structure of ZIF-8 viewed along the <i>c</i> -axis. The pink polyhedrons denote the ZnN <sub>4</sub> units. The yellow sphere indicates the space in the cage. ....	35
Figure 2-2. Selected IR spectra of ZIF-8 on compression to a highest pressure of 39.15 GPa and as recovered (a), and to another highest pressure of 1.60 GPa and as recovered (b).....	38
Figure 2-3. Pressure dependence of selected IR modes of ZIF-8 on compression in the pressure region of 0–1.6 GPa and 2–14 GPa. ....	41
Figure 3-1. (a) IR spectrum of ZIF-8 loaded with CO <sub>2</sub> (middle) compared with that of pure CO <sub>2</sub> (top) and that of pure ZIF-8 (bottom) at similar pressures. The inset shows the zoomed spectral region for the combination modes of ZIF-8 loaded with CO <sub>2</sub> (top) and pure CO <sub>2</sub> (bottom). (b) Photograph of ZIF-8 loaded with CO <sub>2</sub> taken under an optical microscope. The arrows indicate the positions of the C=C stretching mode of the imidazole ring .....	49
Figure 3-2. (a) IR spectra of pure CO <sub>2</sub> in the spectral region of the combination modes collected on compression. (b) Frequency plots of $\nu_3 + \nu_1$ mode of CO <sub>2</sub> as a function of pressure. ....	52
Figure 3-3. IR spectra of ZIF-8 loaded with CO <sub>2</sub> in the spectral region of the combination modes collected on compression (a) and decompression (b) at room temperature. ....	53
Figure 3-4. Far-IR spectra of ZIF-8 upon compression to 2.61 GPa and decompression to ambient pressure. The bands at 420 and 290 cm <sup>-1</sup> can be attributed as Zn-N stretching and	

bending modes, respectively; the lower frequency modes are assigned as framework lattice vibrations.....	57
Figure 3-5. IR spectra of ZIF-8 loaded with CO <sub>2</sub> upon compression and decompression in comparison with those of pure ZIF-8 at similar pressures. The band labeled with an asterisk indicates the position of the C=N stretching mode of the ZIF-8 framework (see text).....	58
Figure 3-6. IR frequencies of selected modes of the ZIF-8 framework loaded with CO <sub>2</sub> as a function of pressure.....	59
Figure 4-1. (a) Local structure and Indium coordination environment of MIL-68 (In). (b) View of the structure of activated MIL-68 (In) along <i>c</i> axis, showing the arrangement of hexagonal and triangular channels. The DMF molecules in the channels of as-made framework can be mostly removed upon activation. ....	64
Figure 4-2. IR spectra for as-made and activated MIL-68(In) in the frequency region (a) 600-4000 cm <sup>-1</sup> , with the inset showing the OH stretching modes in the enlarged spectral region of 3610-3700 cm <sup>-1</sup> at the top; (b) 1200-1800 cm <sup>-1</sup> .....	70
Figure 4-3. The IR spectra of as-made MIL-68(In) upon compression in the frequency region (a) 650-1250 cm <sup>-1</sup> ; (b) 1250-1750 cm <sup>-1</sup> ; (c) 3600-3800 cm <sup>-1</sup> . ....	73
Figure 4-4. Frequency of IR modes of as-made MIL-68(In) as a function of pressure from 0 to 9 GPa in the spectral region of (a) 750-3750 cm <sup>-1</sup> ; (b) 1375-1695 cm <sup>-1</sup> . ....	75
Figure 4-5. IR spectra of activated MIL-68(In) upon compression in the frequency region (a) 700-1250 cm <sup>-1</sup> ; (b) 1200-1750 cm <sup>-1</sup> ; (c) 3500-3700 cm <sup>-1</sup> .....	78
Figure 4-6. Frequency of IR modes of activated MIL-68(In) as a function of pressure from 0 to 9 GPa in the spectral region of (a) 750-3680 cm <sup>-1</sup> ; (b) 1390-1585 cm <sup>-1</sup> . ....	80
Figure 4-7. Illustration of local structure of MIL-68(In) at (a) ambient pressure; (b) high pressure (HP), showing hydrogen bonding between the OH units and carboxyl oxygens.....	82

Figure 4-8. (a) IR spectra of activated MIL-68(In) with PTM upon compression. (b) Frequency of IR modes of activated MIL-68(In) with PTM as a function of pressure from 0 to 18 GPa.....	85
Figure 4-9. IR spectra of activated MIL-68(In) and MIL-68(In) loaded with CO <sub>2</sub> at around 0.4 GPa in the frequency region (a) 600-3800 cm <sup>-1</sup> ; (b) 1325-1800 cm <sup>-1</sup> . ....	89
Figure 4-10. IR spectra of MIL-68(In) loaded with CO <sub>2</sub> upon (a) compression and (b) decompression in the frequency region 3580-3800 cm <sup>-1</sup> .....	91
Figure 4-11. Frequency of the combination modes of CO <sub>2</sub> and the OH stretch mode of MIL-68(In) as a function of pressure from 0.42 to 1.88 GPa.....	92
Figure 4-12. Simulated contour plots of the CO <sub>2</sub> probability density (in arbitrary unit) distributions along the hexagonal and triangular channels of MIL-68(In) framework at (A) 1 bar, (B) 1000 bar or 0.1 GPa and (C) 105 bar (or 10 GPa).....	96
Figure 5-1. The structure of activated $\alpha$ -Mg <sub>3</sub> (HCOO) <sub>6</sub> at ambient conditions. (a) The framework structure along <i>b</i> axis, showing the one-dimensional zigzag channels with a dimension of 4.5 Å × 5.5 Å. The green polyhedrons represent Mg-O clusters. (b) Four Different Mg coordination environments. ....	104
Figure 5-2. (a) Optical image of the sample chamber consisting of activated $\alpha$ -Mg <sub>3</sub> (HCOO) <sub>6</sub> loaded with CO <sub>2</sub> at 0.37 GPa and room temperature. (b) Selected mid-IR spectrum of $\alpha$ -Mg <sub>3</sub> (HCOO) <sub>6</sub> loaded with CO <sub>2</sub> at 0.37 GPa compared with that of the activated $\alpha$ -Mg <sub>3</sub> (HCOO) <sub>6</sub> at 0.33 GPa. The inset shows the enlarged parts of the two spectra in the region of 2650 – 2950 cm <sup>-1</sup> and 3550 – 3750 cm <sup>-1</sup> , respectively. ....	107
Figure 5-3. Selected Raman spectrum of $\alpha$ -Mg <sub>3</sub> (HCOO) <sub>6</sub> loaded with CO <sub>2</sub> at 0.42 GPa compared with the empty $\alpha$ -Mg <sub>3</sub> (HCOO) <sub>6</sub> at 0.44 GPa and $\alpha$ -Mg <sub>3</sub> (HCOO) <sub>6</sub> loaded with DMF at 0.45 GPa in the spectral region 50 – 400 cm <sup>-1</sup> (a); Empty $\alpha$ -Mg <sub>3</sub> (HCOO) <sub>6</sub> at 0.44 GPa in the spectral region 1200 – 3000 cm <sup>-1</sup> (b).....	108
Figure 5-4. Selected mid-IR spectra of $\alpha$ -Mg <sub>3</sub> (HCOO) <sub>6</sub> loaded with CO <sub>2</sub> in the spectra region of 3580–3800 cm <sup>-1</sup> upon compression from 0.30 to 9.82 GPa (a); upon decompression to	

ambient (b); in the spectra region of 1100–3000 cm<sup>-1</sup> upon compression and as recovered to 0.37 GPa (c). ..... 111

Figure 5-5. (a) Selected Raman spectra of  $\alpha$ -Mg<sub>3</sub>(HCOO)<sub>6</sub> loaded with CO<sub>2</sub> in the spectra region of 50 – 400 cm<sup>-1</sup> upon compression from 0.69 to 11.41 GPa and as recovered to 0.40 GPa and ambient pressure. (b) Selected far-IR spectra of  $\alpha$ -Mg<sub>3</sub>(HCOO)<sub>6</sub> loaded with CO<sub>2</sub> in the spectra region of 100 – 550 cm<sup>-1</sup> upon compression from 0.69 to 11.41 GPa and as recovered to 0.40 GPa and ambient pressure. .... 115

Figure 5-6. (a) IR frequencies of  $\nu_{(C-H)}$ ,  $\nu_{s(OCO)}$  and  $\delta_{(C-H)}$  mode of CO<sub>2</sub> loaded  $\alpha$ -Mg<sub>3</sub>(HCOO)<sub>6</sub> as a function of pressure; (b) Raman shifts of the lattice modes (denoted as 1- 4) of CO<sub>2</sub> loaded  $\alpha$ -Mg<sub>3</sub>(HCOO)<sub>6</sub> and the lattice modes ( $F_{g+}$ ,  $F_{g-}$  and  $E_g$ ) of solid CO<sub>2</sub> as a function of pressure; (c) IR frequencies of  $\nu_{(Mg-O)}$  and the lattice modes (denoted as 5- 9) of CO<sub>2</sub> loaded  $\alpha$ -Mg<sub>3</sub>(HCOO)<sub>6</sub> as a function of pressure. .... 117

Figure 5-7. Illustration of CO<sub>2</sub> adsorption in  $\alpha$ -Mg<sub>3</sub>(HCOO)<sub>6</sub>. The grey & red ball-stick models represent the CO<sub>2</sub> molecules adsorbed inside the pores of the framework. The dash lines symbolise the dipole-dipole interaction between CO<sub>2</sub> and the formate ligands. .... 123

Figure 6-1. (a) Local structure and Calcium coordination environment of CaSDB; (b) View of the structure of activated CaSDB along *b* axis, showing the diamond-shaped channels with the size of ~ 5.5 Å in diameter. .... 128

Figure 6-2. IR (bottom) and Raman (top) spectra of activated CaSDB at ambient pressure in the frequency region of 100- 3400 cm<sup>-1</sup>, with the inset showing the C-H stretching modes in the enlarged spectral region of 3000-3300 cm<sup>-1</sup>. .... 132

Figure 6-3. IR spectra of CaSDB upon compression from ambient to 10.93 GPa and upon recovery in the frequency region (a) 100-550 cm<sup>-1</sup> and (b) 1200-3400 cm<sup>-1</sup>. .... 134

Figure 6-4. Raman spectra of CaSDB upon compression from ambient to 10.73 GPa and recovery in the frequency region (a) 100-1250 cm<sup>-1</sup> and (b) 1400-3200 cm<sup>-1</sup>. .... 136

Figure 6-5. Frequency of selected (a) far-IR; (b) mid-IR; and (c) Raman modes of CaSDB as a function of pressure from ambient to 11 GPa. .... 137

Figure 6-6. IR spectra of CaSDB and CO<sub>2</sub> loaded CaSDB at around 0.4 GPa in the spectral region of (a) 100-525 cm<sup>-1</sup>; (b) 600-4000 cm<sup>-1</sup>. The inset shows (a) the optical image of the sample chamber of CaSDB loaded with CO<sub>2</sub>; (b) the CO<sub>2</sub> combination modes in the enlarged spectral region of 3550-3800 cm<sup>-1</sup>. ..... 140

Figure 6-7. IR spectra of CaSDB loaded with CO<sub>2</sub> upon compression from 0.24 to 13.6 GPa and recovery in the frequency region (a) 90-535 cm<sup>-1</sup>; (b) 1200-3300 cm<sup>-1</sup> and (c) 3550-3850 cm<sup>-1</sup>. ..... 144

Figure 6-8. Frequency of selected IR modes of CaSDB loaded with CO<sub>2</sub> GPa in the frequency region of (a) 150-450 cm<sup>-1</sup>; (b) 1275-1700 cm<sup>-1</sup> and (c) 3050-3800 cm<sup>-1</sup> as a function of pressure from 0.24 to 13.6 GPa..... 146

Figure 6-9. Raman spectra of CaSDB upon compression from (a) 0.24-4.08 GPa; (b) 5.39-13.6 GPa and recovery in the frequency region of 75-450 cm<sup>-1</sup> and (c) Frequency of selected Raman modes of CaSDB loaded with CO<sub>2</sub> as a function of pressure from 0.24 to 13.6 GPa. .... 148

Figure 6-10. CO<sub>2</sub> adsorption in CaSDB at (a) ambient pressure; (b) high pressures (HP). The blue balls represent CO<sub>2</sub> molecules inside the pores of CaSDB, with the oxygen atoms omitted. The dash lines symbolize the interactions between CO<sub>2</sub> and the specific adsorption sites of the framework..... 154

## List of Abbreviations

<b>1D</b>	one-dimensional
<b>3D</b>	three-dimensional
<b>APS</b>	Advanced Photon Source
<b>ANL</b>	Argonne National Laboratory
<b>BDC</b>	1,4-benzenedicarboxylate
<b>BET</b>	Brunauer–Emmett–Teller
<b>BS</b>	beam splitter
<b>BNL</b>	Brookhaven National Laboratory
<b>BTC</b>	benzene-1,3,5-tricarboxylate
<b>CCD</b>	charge coupled device
<b>DAC</b>	diamond anvil cell
<b>DMF</b>	<i>N,N</i> -dimethylformamide
<b>dobdc</b>	2,5-dioxido-1,4-benzenedicarboxylate
<b>FTIR</b>	Fourier transform infrared
<b>GCMC</b>	Grand Canonical Monte Carlo
<b>GPa</b>	gigapascal
<b>HP</b>	high pressure
<b>IR</b>	infrared
<b>IRIS</b>	infrared radiation interferometer spectrometer
<b>IRMOF</b>	isoreticular metal–organic framework
<b>MCT</b>	mercury cadmium telluride

<b>MIL</b>	Matériaux de l'Institut Lavoisier
<b>mmen</b>	N,N'-dimethylethylenediamine
<b>MOF</b>	metal-organic framework
<b>NF</b>	notch filter
<b>NLC</b>	negative linear compressibility
<b>NSLS</b>	National Synchrotron Light Source
<b>PTM</b>	pressure transmitting medium
<b>SDB</b>	4, 4'-sulfonyldibenzoate
<b>XRD</b>	X-ray diffraction
<b>ZAG</b>	zinc alkyl gate
<b>ZIF</b>	zeolitic imidazolate framework
<b>ZSM</b>	Zeolite Socony Mobil

## Chapter 1

### 1 Introduction

#### 1.1 Metal-organic frameworks

##### 1.1.1 Structures of metal-organic frameworks

Metal-organic frameworks (MOFs) are an emerging class of crystalline materials constructed by bridging metal-containing units with organic linkers to create open rigid frameworks with permanent porosity. One of the prototype and earliest-studied MOF structure is MOF-5, a cubic framework built from octahedral  $[\text{Zn}_4\text{O}(\text{CO}_2)_6]$  clusters which consist of oxygen-centered  $\text{Zn}_4$  tetrahedra linked by 1,4-benzenedicarboxylate (BDC) ligands, as illustrated in Figure 1-1 (a).<sup>1</sup> Based on the cubic skeleton of MOF-5, a large series of isorecticular MOFs (IRMOFs) that have the same framework topology but with different pore size and functionality can be produced by tuning the length and functionalities of organic linkers, as shown in Figure 1-1 (b).<sup>2</sup> Such IRMOFs have been found in other MOF families, such as  $\text{Zr}_6\text{O}_4(\text{OH})_4(\text{BDC})_6$  (UiO-66),<sup>3,4</sup>  $\text{Al}(\text{OH})(\text{BDC})$  (MIL-53),<sup>5,6</sup> and  $\text{Cu}_2(\text{BPTC})$  (BPTC=3,3',4,4'-benzophenonetetracarboxylate).<sup>7</sup> Thus a large variety of MOFs with rich structural and topological diversity can be made owing to the extraordinary degree of variability for both the organic and inorganic components. Up to date, more than 20,000 MOF structures have been reported and studied within the past decade.<sup>8</sup> Due to their permanent porosity, high thermal stability, large surface area and finely tunable chemical functionality, MOFs have wide applications in gas storage,<sup>9-11</sup> gas separation,<sup>12</sup> catalysis,<sup>13</sup> drug delivery,<sup>14</sup> chemical sensors<sup>15</sup> and so on.



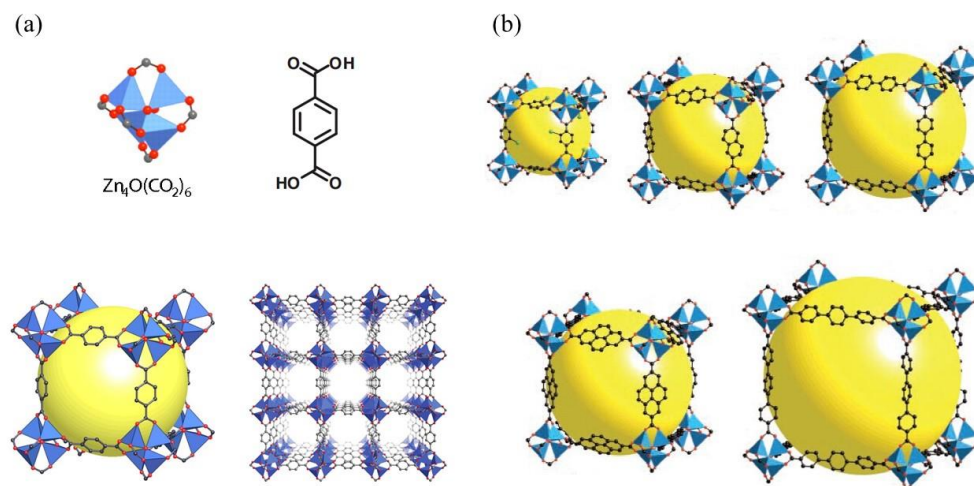


**Figure 1-1.** (a) The building units and structure of MOF-5; (b) Isoreticular MOFs of MOF-5. (ref. 1, 2)

### 1.1.2 CO<sub>2</sub> storage in metal-organic frameworks

One of the most promising applications of MOFs is gas storage, especially CO<sub>2</sub> storage. As a green-house gas, the sharply rising level of CO<sub>2</sub> in atmosphere resulting from combustion of coal, oil, and natural gas is one of the greatest environmental concerns today. Thus it is imperative to develop effective carbon capture and storage (CCS) technologies to address this issue. Current technologies involving aqueous amine absorbents to capture CO<sub>2</sub> have been extensively studied and are considered the state-of-the-art.<sup>16</sup> But it carries a large energy penalty that originates primarily from the need to heat the large quantities of the amine solutions, as well as the energy required to break the C–N bond formed in the interaction between CO<sub>2</sub> and the amine functionality.<sup>17</sup> Hence, solid porous adsorbents which have much lower heat capacities are considered as an alternative strategy for efficient CO<sub>2</sub> capture and storage, such as zeolites,<sup>18-22</sup> activated

carbons,<sup>23</sup> covalent-organic frameworks,<sup>24-27</sup> amine-grafted silica<sup>28,29</sup> and MOFs. Among these porous materials, MOFs are most promising for the applications in CO<sub>2</sub> storage, owing to their ultra-high porosity, large pore volume and surface area, and most importantly, a flexibility with which chemical functionalization and molecular-level fine-tuning can be achieved for optimized uptake capacities.

The adsorptive capacity is a critical parameter to evaluate the performance of MOFs for CO<sub>2</sub> storage. CO<sub>2</sub> capacity in MOFs can be measured by the gravimetric CO<sub>2</sub> uptake, which represents the quantity of CO<sub>2</sub> adsorbed within a unit mass of the material; or the volumetric capacity refers to how densely the CO<sub>2</sub> can be stored within the material. The high internal surface areas of MOFs make large CO<sub>2</sub> adsorption capacities in the framework possible because of the efficient packing and close approach of the guest molecules on the pore surface. For example, MOF-177 [Zn<sub>4</sub>O(1,3,5-benzenetricarboxylate)<sub>2</sub>] combines an exceptional level of surface area (4,500 m<sup>2</sup>/g) with extra-large pores (11 × 17 Å) that are desirable for CO<sub>2</sub> storage.<sup>30</sup> The volumetric CO<sub>2</sub> adsorption capacity for MOF-177 at 35 bar reaches a storage density of 320 cm<sup>3</sup>(STP)/cm<sup>3</sup> (STP= standard temperature and pressure), which is 9 times higher than the quantity stored at this pressure in a container without the adsorbent and 2 times higher than other porous materials such as zeolite 13X and activated carbon, as shown in Figure 1-2.<sup>31</sup> The high-pressure (10-50 bar) adsorption capacities are mainly dependent on the surface area of MOFs, whereas the low-pressure (<1.2 bar) adsorption capacities for MOFs are highly influenced by the chemical features of the pore surface, especially those bearing highly functionalized surfaces.<sup>10</sup> Therefore, functionalization of the frameworks to improve the CO<sub>2</sub> binding affinity is crucial for optimization of the adsorptive properties of MOFs at low pressures.

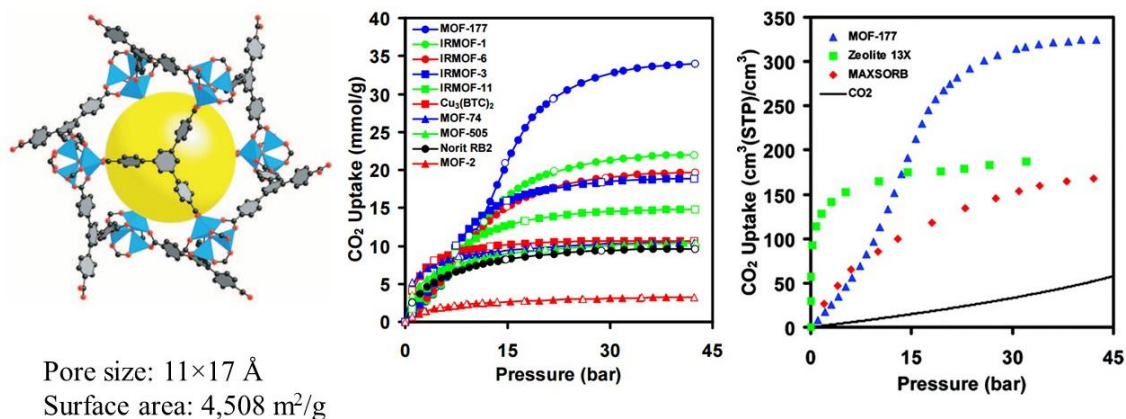


**Figure 1-2.** The crystal structure of MOF-177 and comparison of the gravimetric and volumetric  $\text{CO}_2$  capacity for several MOFs and other porous materials. (ref. 31)

Up to date, various types of functionalities in MOFs have been explored to enhance the  $\text{CO}_2$  adsorption selectivity and capacity, including amines, strongly polarizing organic functionalities, and exposed metal cation sites. MOFs functionalized with amines have been intensively studied for their  $\text{CO}_2$  adsorption properties.<sup>32-35</sup> The dispersion and electrostatic forces resulting from the interaction of the quadrupole moment of  $\text{CO}_2$  with localized dipoles generated by nitrogen incorporation are considered responsible for the enhanced  $\text{CO}_2$  adsorption. In addition, acid-base type interactions between the lone-pair of nitrogen and  $\text{CO}_2$  have been observed as well. The commercial availability of aromatic amine containing linkers, such as 2-aminoterephthalic acid ( $\text{NH}_2\text{-BDC}$ ), and the expected affinity of amino groups toward  $\text{CO}_2$  have generated significant interest in aromatic amine functionalized frameworks. For example, MOF-5 [ $\text{Zn}_4\text{O}(\text{BDC})_3$ ] adsorbs approximately 4.6 wt %  $\text{CO}_2$  at 298 K and 1.1 bar; while the amine-functionalized variant IRMOF-3

[Zn<sub>4</sub>O(NH<sub>2</sub>-BDC)<sub>3</sub>] adsorbs 5.0 wt % CO<sub>2</sub>, despite a decrease in the BET surface area from 2833 to 2160 m<sup>2</sup>/g.<sup>31</sup> Moreover, amine functionalization has been shown to enhance CO<sub>2</sub> capacity via incorporation of alkylamines into MOF pores.<sup>36,37</sup> For instance, alkylamine incorporation onto the metal sites of Cu-BTTri (H<sub>3</sub>[(Cu<sub>4</sub>Cl)<sub>3</sub>(BTTri)<sub>8</sub>; H<sub>3</sub>BTTri = 1,3,5-tri(1*H*-1,2,3-triazol-4-yl)benzene) was found to be an effective method to enhance the CO<sub>2</sub> binding through post-synthetic modifications of MOFs. At 0.15 bar, the gravimetric capacity was increased to 9.5 wt % for the functionalized Cu-BTTri framework, which is approximately 3.5 times higher than that of the original framework, as shown in Figure 1-3.<sup>37</sup>

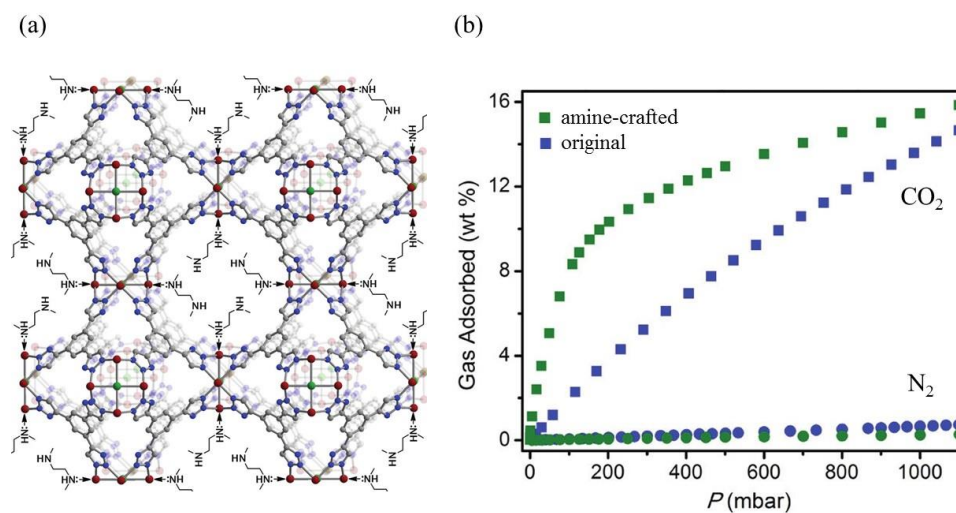


**Figure 1-3.** (a) Functionalization of Cu-BTTri through binding N,N'-dimethylethylenediamine (mmen) to the metal coordination sites; (b) the CO<sub>2</sub> (square) and N<sub>2</sub> (circle) adsorption isotherms for mmen-Cu-BTTri (green) and Cu-BTTri (blue) at 298 K. (ref. 37)

In addition to the amine functionalized MOFs, organic linkers with other functional groups have also been investigated for their effects on the CO<sub>2</sub> adsorption performance.<sup>38-47</sup> These functional groups include hydroxyl, nitro, cyano, thio, and halide groups, and the degree of how much CO<sub>2</sub> adsorption is enhanced mainly depends on the extent of ligand functionalization and the polarizing strength of the functional group. In general, more strongly polarizing groups will influence CO<sub>2</sub> adsorption more favorably.

Another important approach that has been developed to improve the affinity and selectivity of MOFs toward CO<sub>2</sub> is the generation of MOF structures with exposed metal cation sites on the pore surface.<sup>48-53</sup> The open metal sites can be obtained by desolvation of the MOFs, where one of the solvent molecules in the metal coordination sphere is removed upon heating in vacuum conditions. For the application of CO<sub>2</sub> capture and storage, the open metal cation sites serve as charge-dense binding sites for CO<sub>2</sub> which is adsorbed strongly at these sites due to its large quadrupole moment and polarizability. The earliest study of MOFs possessing exposed metal cation sites was on HKUST-1 [Cu<sub>3</sub>(BTC)<sub>2</sub>; BTC: benzene-1,3,5-tricarboxylate], in which the solvent molecules on the axial sites of the paddlewheel units can be removed to generate open Cu<sup>2+</sup> sites that interact strongly with CO<sub>2</sub>.<sup>48</sup> More recently, a series of MOFs M<sub>2</sub>(dobdc) (M = Mg, Mn, Co, Ni, and Zn; dobdc = 2,5-dioxido-1,4-benzenedicarboxylate) also known as MOF-74 or CPO-27 have drawn much attention and became one of the most well-studied MOFs with open metal sites.<sup>54</sup> Each of these MOFs is composed of M<sup>II</sup> ions generating linear, infinite building units bound by dobdc ligands resulting in a hexagonal, 1D pore structure. The pores of the as-made M<sub>2</sub>(dobdc) MOFs contain solvent molecules that complete the coordination sphere of the metal ions and can be removed upon evacuation to generate coordinately unsaturated

metal sites. Sorbent materials such as CO<sub>2</sub> are thus provided with a honeycomb structure composed of 1D channels as depicted in Figure 1-4 (a). The high density of binding sites in the hexagonal pores makes remarkably high CO<sub>2</sub> adsorption capacities in the M<sub>2</sub>(dobdc) MOFs, ranging from 19.8 to 26.0 wt % at 1 bar & 296 K, as shown in Figure 1-4 (b). So far, the gravimetric and volumetric CO<sub>2</sub> adsorption capacities in Mg<sub>2</sub>(dobdc) are the highest among all the MOFs in low-pressure range, despite its relatively low surface area (1495 m<sup>2</sup>/g). Thus functionalization of the pores with a large number of high-affinity binding sites is an effective way to substantially enhance the CO<sub>2</sub> adsorption capacity in a MOF.

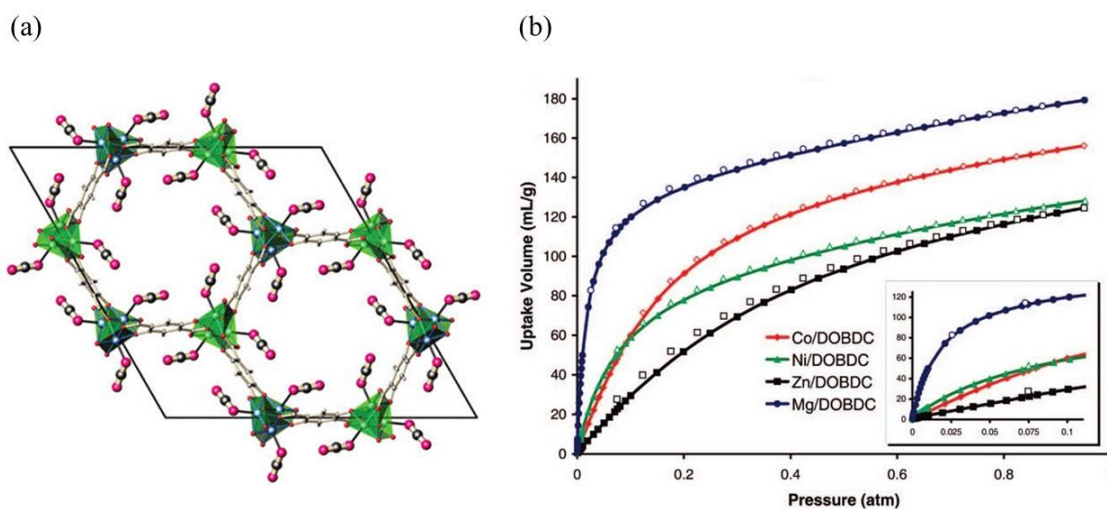


**Figure 1-4.** (a) View of 1D channel of the structure of MOF M<sub>2</sub>(dobdc) adsorbed with CO<sub>2</sub>; (b) CO<sub>2</sub> sorption isotherm (296 K, 0 to 1 atm) of the MOF M<sub>2</sub>(dobdc) series. (ref. 54)

## 1.2 High-pressure science and technology

### 1.2.1 High-pressure phenomena

It is well known that temperature, pressure and volume are three basic macroscopic parameters to describe a thermodynamic system. Among these parameters, pressure spans over 60 orders of magnitude in the universe, from  $10^{-32}$  atmosphere in intergalactic space to  $10^{32}$  atmosphere in the center of neutron star.<sup>55</sup> Under such a broad range of pressure, materials could exhibit various structures as well as novel properties. When applying pressure to materials, the general effect is to reduce the volume of the materials, as pressure can efficiently shorten the inter-molecular and intra-molecular distances, which will increase the free energy of the system.<sup>56</sup> The relation between pressure (P) and total energy (E) can be described by eq. 1.1,

$$P = -\frac{\partial E}{\partial V} \quad (1.1)$$

Consequently, an alternation of the volume will change the total energy of the system. The response of the system to retrieve a new free energy minimum will result in a number of possible processes, such as phase transformation, ionization, polymerization, amorphization, dissociation, metallization and so on. Hence, the application of high pressure on matters provides an effective method to delicately tune their electronic, magnetic, optical and mechanical properties.<sup>56</sup> Some examples of interesting phenomena and novel materials with exotic structures and properties generated under high pressure are highlighted in Figure 1-5.<sup>57</sup>

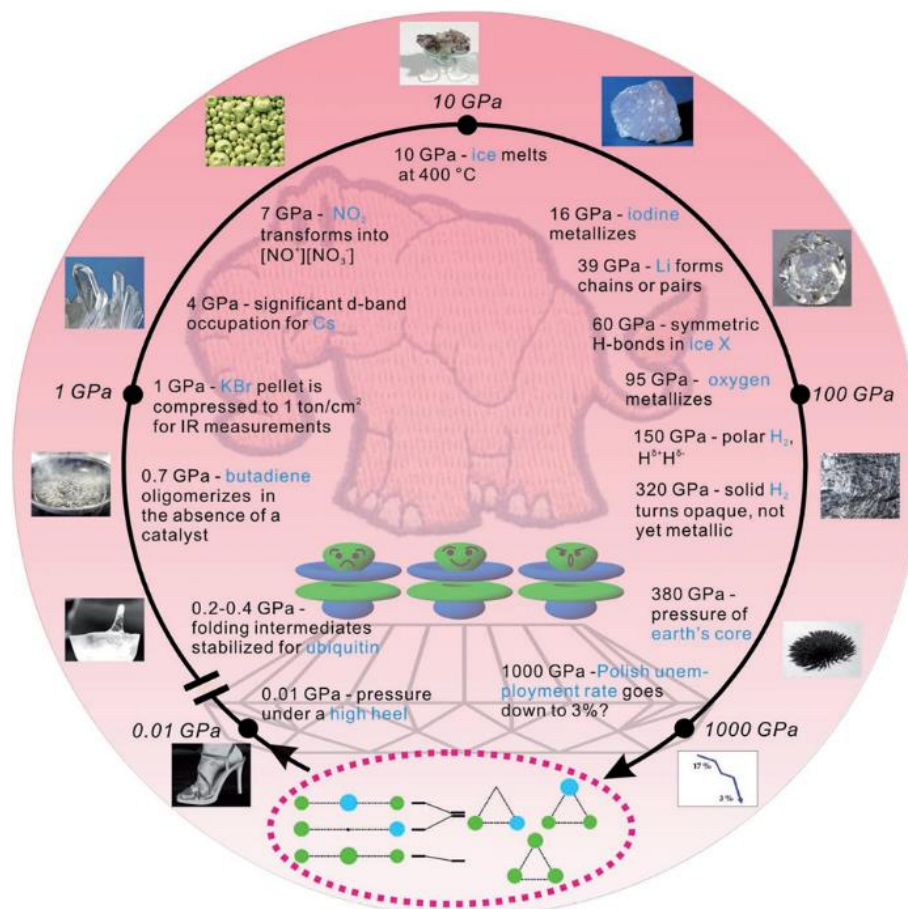


**Figure 1-5.** Examples of various high-pressure phenomena. (ref. 57)

### 1.2.2 Diamond anvil cell

In order to achieve static high pressure in gigapascal range ( $1 \text{ GPa} = 10^9 \text{ Pa} = 10^4 \text{ bar}$ ) in lab, a special device called diamond anvil cell (DAC) which can generate pressure up to  $\sim 360 \text{ GPa}$  has been used.<sup>58,59</sup> Diamonds are known as the hardest material in nature and thus suitable to be used as anvils to generate high pressure. Moreover, diamonds are transparent to a wide spectral range of electromagnetic radiation. As a result, various probes, such as vibrational spectroscopy, X-ray diffraction etc., could be utilized for *in situ* structural characterizations of materials in the DAC under high pressures.<sup>60</sup> The principle



and operation of the DAC is quite simple as shown in Figure 1-6. A stainless steel gasket, which is drilled with a hole at the center and used to contain the sample, is compressed between a pair of identical diamond anvils. The culet (the tip of diamond) size usually varies from 100 to 700  $\mu\text{m}$ , depending on the maximum pressure desired. Due to the small area of the diamond culet, high pressure can be achieved by applying a moderate force on the sample.

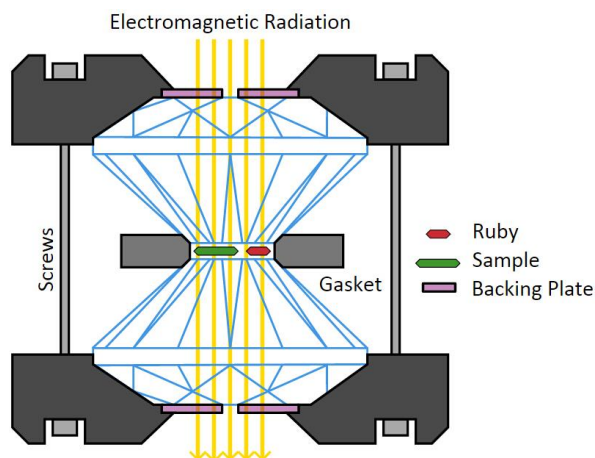


**Figure 1-6.** Opposed diamond anvil configuration, with a metal gasket for sample confinement.

The pressure inside the sample chamber can be monitored using a reference material, such as ruby ( $\text{Al}_2\text{O}_3$  doped with  $\text{Cr}^{3+}$ ) whose behavior under pressure is known. Ruby fluorescence is one of the well-established methods to measure pressure reliably and accurately.<sup>61-63</sup> When excited by laser, ruby emits luminescent peaks  $R_1$  and  $R_2$ , where the position of  $R_1$  peak is very sensitive to pressure and an equation was established to describe the relationship between pressure and the wavelength of  $R_1$  line.<sup>63</sup>

$$P = \frac{1904}{B} \left[ \left( 1 + \frac{\Delta\lambda}{694.24} \right)^B - 1 \right] \quad (1.2)$$

where  $P$  is pressure in GPa and  $\Delta\lambda$  is the difference between the wavelength of the ruby  $R_1$  line at pressure  $P$  and that at ambient pressure. The parameter  $B$  in the equation equals to 7.665 for quasi-hydrostatic conditions, and equals to 5 for non-hydrostatic conditions.<sup>63</sup> An example of using ruby fluorescence to determine pressure is shown in Figure 1-7. The resolution of the pressure can be achieved to  $\pm 0.05$  GPa by using this method.

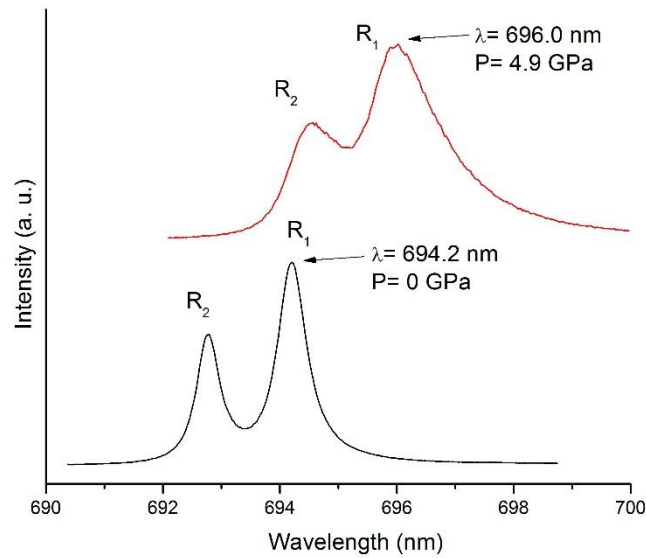


**Figure 1-7.** Ruby  $R_1$  fluorescence spectra at 0 GPa (in black) and 4.9 GPa (in red) under room temperature.

### 1.2.3 *In situ* high-pressure characterizations

Vibrational spectroscopy which allows the understanding of pressure effects on chemical bonding and especially local structures, is used as the primary characterization method in this thesis. It is known that molecules have various types of interactions with electromagnetic field, including absorption, emission, scattering and so on, which can lead to different forms of excitations. The energy transferred from the electromagnetic field to the molecule at the vibrational levels (1-1,000  $\mu\text{m}$ ) can be recorded by vibrational spectroscopy, providing information on molecular structures, chemical bonding, changes in the physical and chemical configurations (e.g. crystallinity, confirmation etc.). The most common techniques for vibrational spectroscopy are infra-red (IR) and Raman spectroscopy which provide similar information about molecule vibrations, however, with different selection rules. In general, IR absorption can be detected if the dipole moment in a molecule is changed during a normal vibration. Whereas Raman process results from the change of polarizability (the ability for a molecule to be polarized) due to the vibration.<sup>64</sup> Therefore, for non-silent molecular vibrations, IR and Raman spectroscopy are complementary to each other by providing a whole picture of molecular vibrations.

In high-pressure experiments, special consideration must be taken for interfacing the technique with DAC due to the small sample size and the presence of the diamond window. Thus, the IR and Raman system used in the local lab are both highly customized and incorporated with microscopes to allow optical observations because of the transparency of diamond windows.

A customized IR micro-spectroscopy system was used for all room-temperature IR absorption measurements. Figure 1-8 shows the schematic diagram of the system. A

commercial Fourier transform infrared (FTIR) spectrometer from Bruker Optics Inc. (Model Vertex 80v) equipped with Globar mid-IR light source constituted the main component of the micro-IR system, which was operated under a vacuum of  $< 5$  mbar, such that the absorption by  $\text{H}_2\text{O}$  and  $\text{CO}_2$  was efficiently removed. A collimated IR beam was directed into a relay box through a KBr window on the spectrometer. The beam was then focused onto the sample in the DAC by an iris optics and  $15\times$  reflective objective lens with a numerical aperture of 0.4. The size of the IR beam was set to be identical to the entire sample size (e.g.  $\sim 130 \mu\text{m}$ ) by a series of iris apertures. The transmitted IR beam was collected using another identical reflective objective as the condenser, and was directed to a wide-band mercury cadmium telluride (MCT) detector equipped with a ZnSe window that allows measurements in the spectral range of 600 to  $12000 \text{ cm}^{-1}$ . The customized spectroscopic system also allows IR measurements in the reflection mode using reflective optics via the optical path shown in Figure 1-8.<sup>65</sup>

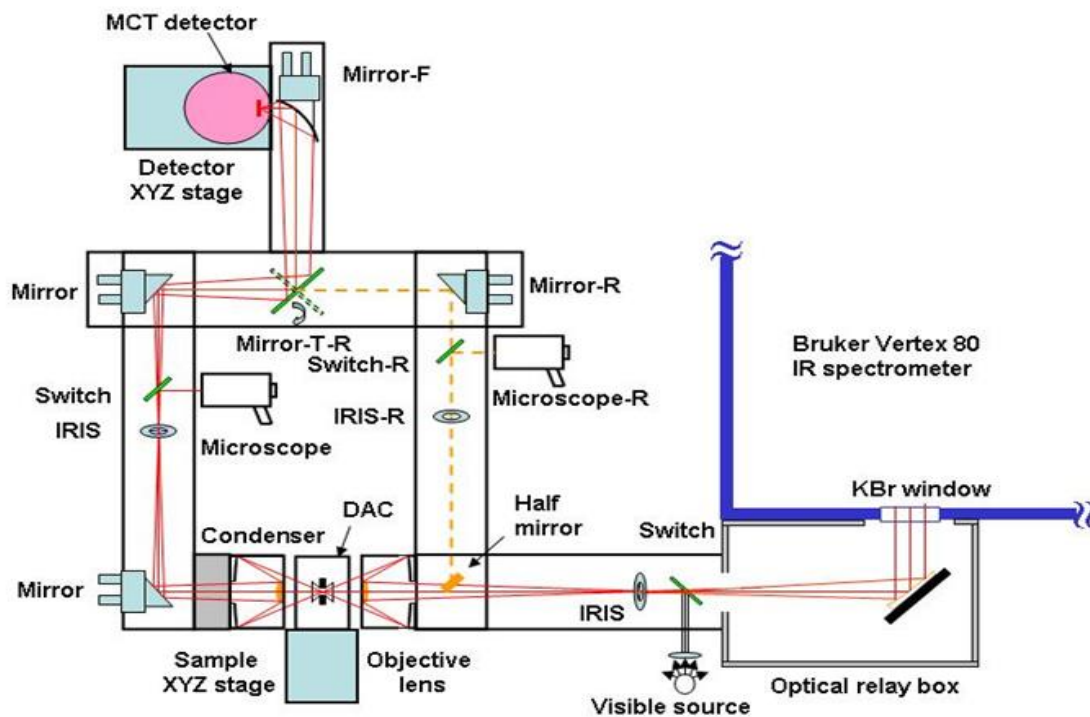


**Figure 1-8.** Schematic diagram of the IR micro-spectroscopy system, with major optical components labeled. (ref. 65)

To collect Raman spectra, a customized Raman micro-spectroscopy system was used. The schematic diagram of this Raman system is depicted in Figure 1-9. A single longitudinal mode, diode pumped solid state (DPSS) green laser with wavelength 532.10 nm was used as the excitation source. The laser was focused to  $< 5 \mu\text{m}$  on the sample by a  $20\times$  objective. The Raman signal was detected with backscattering geometry by the same objective lens. The Rayleigh scattering was removed by a pair of notch filters. The scattered light was then dispersed using an imaging spectrograph equipped with a 1200 lines/mm grating achieving a  $0.1 \text{ cm}^{-1}$  resolution. The Raman signal was recorded using

an ultrasensitive, liquid nitrogen cooled, back-illuminated, charge-coupled device (CCD) detector. The system was calibrated by neon lines with an uncertainty of  $\pm 1 \text{ cm}^{-1}$ .<sup>66</sup>

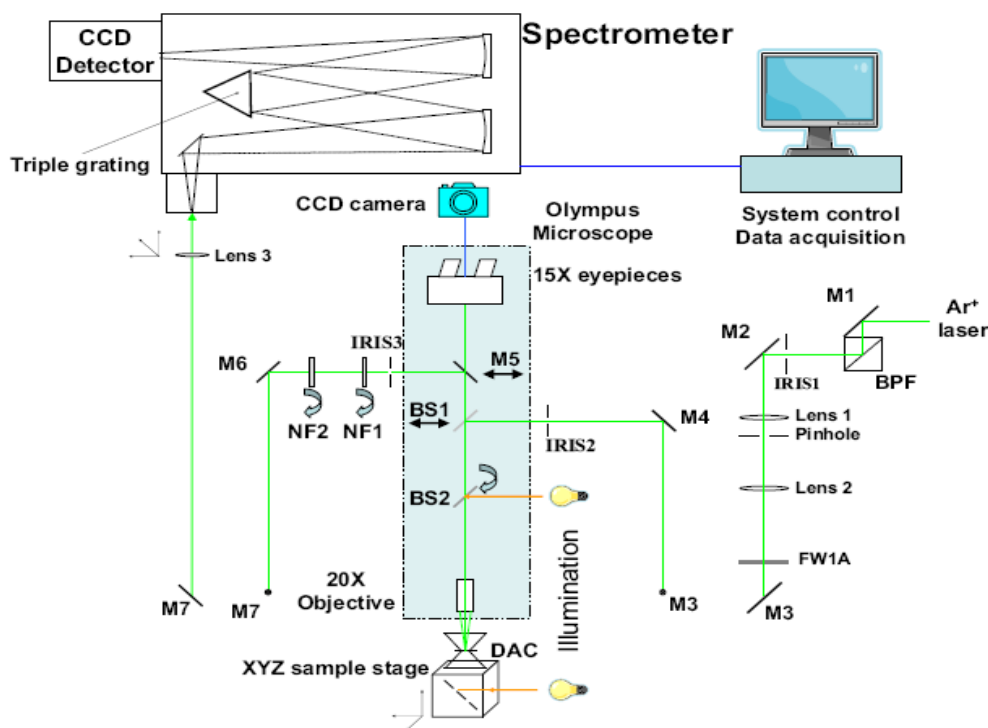


**Figure 1-9.** Schematic of the Raman system. BPF: band path filter; IRIS: IRIS aperture; M1-7: broadband dielectric reflecting mirrors; FW1A: Six station filter wheel; BS: beam splitter; NF: notch filter; DAC: diamond anvil cell; Triple gratings: 300 lines/mm, 1200 lines/mm, and 1800 lines/mm. (ref. 66)

In addition to vibrational spectroscopy, high-pressure X-ray diffraction (XRD) is another powerful technique for the characterization of materials on compression, providing information on structural evolution of the crystal lattice. In high-pressure studies, due to the bulk anvils of DAC and small sample sizes, X-ray diffraction measurements can only be performed with intense high energy X-ray beam and small beam size (e.g., tens of

microns), which can only be achieved by synchrotron radiation source due to its wide energy range, high brightness and finely tunable beam size.<sup>67</sup> The synchrotron facilities at the National Synchrotron Light Source (NSLS) in Brookhaven National Laboratory (BNL), and Advanced Photon Source (APS) in Argonne National Laboratory (ANL) provide highly collimated X-ray source with intense high energy, optimized for *in situ* high pressure XRD measurements.

#### 1.2.4 IR and Raman spectra of CO<sub>2</sub> at high pressures

CO<sub>2</sub> is the centerpiece of this work and thus it is imperative to have a comprehensive understanding of the CO<sub>2</sub> basics, especially its pressure behavior and the vibrational spectra at high pressures. Figure 1-10 (a) illustrates the CO<sub>2</sub> phase diagram in the high pressure region.<sup>68</sup> Under room temperature, CO<sub>2</sub> transforms to liquid state at pressures above 5.1 atm. At pressures higher than 0.6 GPa, it becomes solid known as dry ice. In this study, CO<sub>2</sub> was trapped with the MOF sample in the DAC upon initial loading at ~ 0.3–0.5 GPa and then compressed to higher pressures. Thus CO<sub>2</sub> experienced a phase transition from liquid to solid phase at 0.6 GPa upon compression. During all the measurements in this work, CO<sub>2</sub> was either in liquid phase at lower pressures or in solid phase I at higher pressures.

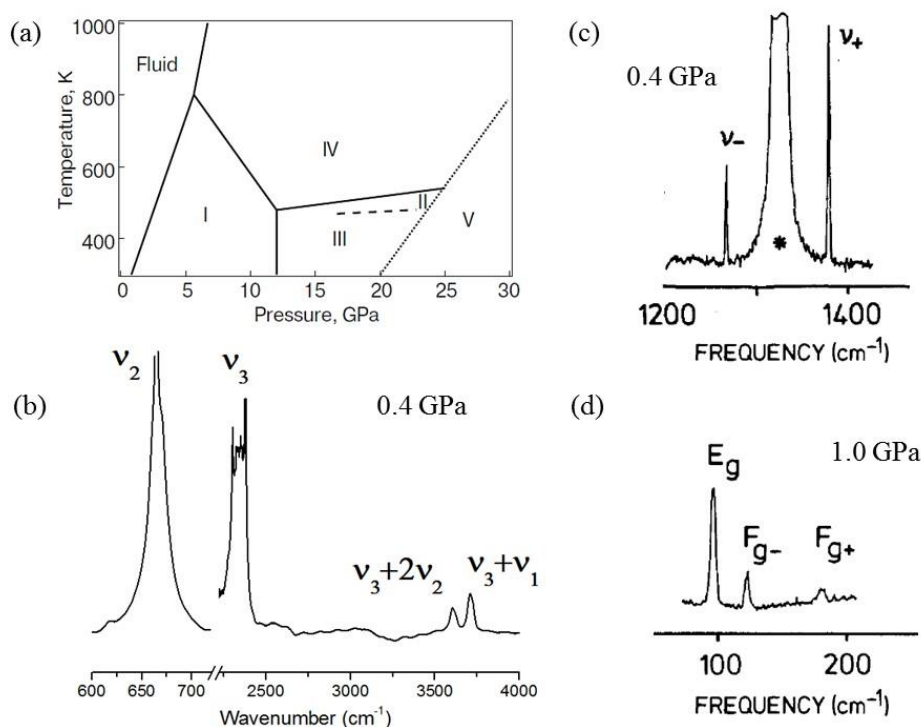


**Figure 1-10.** (a) CO<sub>2</sub> phase diagram (ref. 68); (b) IR spectrum of liquid CO<sub>2</sub> at 0.4 GPa; Raman spectrum of CO<sub>2</sub> (c) at 0.4 GPa and (d) at 1.0 GPa in the lattice region. (ref. 70)

The vibrational spectrum of liquid CO<sub>2</sub> is the same with that of gaseous CO<sub>2</sub>, which is a linear and centrosymmetric molecule. It has three normal vibrational modes, the symmetric stretching mode  $\nu_1$ , the bending mode  $\nu_2$ , and the asymmetric mode  $\nu_3$ , among which the  $\nu_2$  and  $\nu_3$  modes are infrared active, as shown in Figure 1-10 (b). IR absorption associated with the normal vibrations was too strong and thus their band positions were unable to be determined due to saturation. However, two high-frequency bands with adequate absorption intensity, which are well understood as the CO<sub>2</sub> combination modes of  $\nu_3 + 2\nu_2$  and  $\nu_3 + \nu_1$  can be observed and used to monitor the pressure behavior of CO<sub>2</sub>.<sup>69</sup> The other normal mode  $\nu_1$  is Raman active, however, anharmonic coupling between nearly



degenerate modes  $\nu_1$  and overtone  $2\nu_2$  gives rise to modes  $\nu_+$  ( $\approx \nu_1$ ) and  $\nu_-$  ( $\approx 2\nu_2$ ) in the Raman spectrum (Fermi resonance), as depicted in Figure 1-10 (c).<sup>70</sup>

Upon solidification,  $\text{CO}_2$  crystallizes in a cubic space group  $Pa\bar{3}$  (phase I), in which the molecules are oriented along the body diagonal of the cubic cell.<sup>70</sup> Each primitive unit cell contains four  $\text{CO}_2$  molecules. In addition to the three internal modes in the gas phase, solid state  $\text{CO}_2$  features external modes in the low frequency region due to the translational and rotational motions of a whole molecule within the unit cell. Figure 1-10 (d) shows the three external modes (lattice modes) of solid  $\text{CO}_2$  at  $\sim 1$  GPa under room temperature.

### 1.3 High-pressure effects on MOFs

For the application of  $\text{CO}_2$  storage, MOFs need to be mechanically stable enough to allow a dense packing of the adsorbent bed without loss of the framework structure. Even slight perturbations to the structural or chemical features of MOFs under a high mechanical pressure could have a considerable effect on their performance for  $\text{CO}_2$  adsorption. In contrast to the extensive studies of MOFs under ambient conditions, the investigations of MOFs under high external pressure in the order of gigapascal are much less. Thus it is of great interest to thoroughly explore the behavior and performance of MOFs under high pressure. So far, studies have demonstrated a wide variety of behavior of MOFs in response to the application of high external pressure, including unusual elastic responses, phase transitions, chemical reactions and high-pressure guest insertion.<sup>71</sup> In this section of the thesis, selected examples will be given for those specific high-pressure effects on MOFs.

### 1.3.1 Unusual elastic responses

The diversity of the mechanical behavior of materials as a function of topology has been well established for inorganic materials, such as zeolites.<sup>72-74</sup> However, the mechanical properties of MOFs under external stress is an aspect that has not been thoroughly explored mostly due to the difficulties in determining them reliably from relatively small crystal sizes. Nonetheless, some systematic efforts at measuring mechanical properties of MOFs, including bulk modulus (through high-pressure crystallography), directional Young's moduli and hardnesses (through nanoindentation of micro-crystals) have been made in recent years.<sup>75-80</sup> It was found that some MOFs have demonstrated unusual mechanical responses to external pressure by deformations of large amplitude or counterintuitive direction. The most representative example of counterintuitive mechanical behavior of MOFs is negative linear compressibility (NLC), in which the material expands along one or more directions while undergoing a reduction in volume under increasing pressure. The NLC has been found in MOFs with wine rack-type framework including silver(I) 2-methylimidazolate<sup>81</sup> and  $[\text{NH}_4][\text{Zn}(\text{HCOO})_3]$ ,<sup>82</sup> as well as in MOFs exhibiting a similar hinging mechanism, such as MIL-53.<sup>83,84</sup> For example, MIL-53(Al) showed an expansion in the *b* direction while contracting in the *a* and *c* directions, demonstrating NLC in one direction upon increasing pressure from 0 to 3 GPa, as illustrated in Figure 1-11. To understand the mechanism that leads to the NLC phenomenon in MIL-53(Al), the inorganic Al(OH) chains can be visualized to act as hinges in the flexible framework. Dicarboxylate linkers in the orthogonal plane connect these hinges to each other, serving as rigid struts. The rigidity of the struts in this wine-rack geometry enforces a connection between variations in the *a* and *b* lattice parameters: when

$a$  decreases,  $b$  increases, giving rise to the NLC phenomenon. The unique property of NLC in MOFs can be utilized for potential applications in pressure sensors.

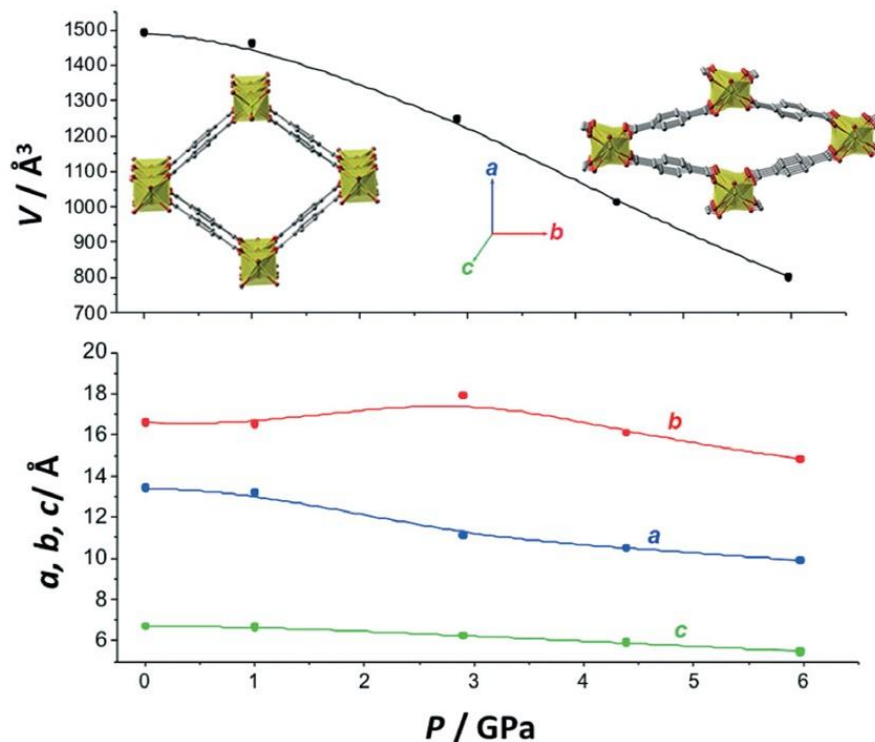


**Figure 1-11.** Evolution of the cell volume (top) and lattice parameters (bottom) of MIL-53(Al) with increasing pressure. (ref. 83)

Moreover, another class of abnormal mechanical property of MOFs is the extreme anisotropy of elastic moduli, with some crystal directions exhibiting deformations of much larger amplitude than others. This phenomenon is highly dependent on the MOF topology. In general, deformations resulting from compression of the framework's linker usually exhibit high elastic moduli, whereas the hinges of the framework involving weaker interactions have much lower stiffness. The contrast between the strong intramolecular

interactions (covalent & coordination bonds) and the weak intermolecular interactions (van der Waals forces, hydrogen bonds, etc.) in MOFs can lead to up to two orders of magnitude in difference between the highest and lowest moduli.<sup>85</sup> The extreme elastic anisotropy is a key feature of highly flexible MOFs, also known as the “breathing” MOFs.<sup>86</sup>

### 1.3.2 Phase transitions

Besides the unusual elastic responses under compression, some MOFs were found to exhibit pressure-induced phase transformations. The most commonly observed phase transitions of MOFs is the pressure-induced amorphization, which has been well-studied in the family of zeolitic imidazolate frameworks (ZIFs). For example, ZIF-8 shows an irreversible amorphization under non-hydrostatic compression at 0.3 GPa<sup>87</sup> as well as under mild ball-milling.<sup>88</sup> Under hydrostatic compression on ZIF-4, which has a lower porosity compared with ZIF-8, the amorphization was found to be reversible at a higher pressure (0.35-0.98 GPa) in the evacuated state. In addition, the presence of solvent molecules in the pores of as-made ZIF-4 shifts amorphization to higher pressure and even leads to the generation of an intermediate crystalline phase.<sup>89</sup> Therefore, the conditions for the amorphization of different ZIFs vary, depending on pressurization conditions, framework topology and porosity, presence of guest inside the pores, and so on. By measuring the elastic constants of ZIFs up to the amorphization pressure, the crystal-to-amorphous transition was found to be triggered by a mechanical instability under compression, due to shear mode softening of the materials.<sup>86,90</sup>

Furthermore, MOFs also demonstrated crystalline-to-crystalline phase transitions induced by compression. Such transitions lead to the formation of a denser phase under high pressure, usually accompanied by a distortion of the framework from the ambient phase. A distinctive example is the pressure-induced phase transition of  $\text{Zn}(\text{CN})_2$ , which transforms from a dense interpenetrated framework at ambient pressure to a series of new porous frameworks at high pressures (0.9-1.8 GPa). These phase transitions are driven by an increase in overall atomic packing density allowed by including fluid molecules in the pores of the framework and involves a buckling of the  $\text{Zn}-\text{CN}-\text{Zn}$  linkage from a linear conformation in the ambient phase to a displaced  $\text{CN}^-$  anion and shorter  $\text{Zn} \cdots \text{Zn}$  distance in the high-pressure phase, as depicted in Figure 1-12.<sup>91</sup> The crystalline-to-crystalline phase transformations under high pressure have been found among other MOFs as well, such as MIL-53 (Cr),<sup>92,93</sup> MIL-47,<sup>94</sup>  $\text{Co}_2(4,4'\text{-bipyridine})_3(\text{NO}_3)_4$ <sup>95</sup> and so on.

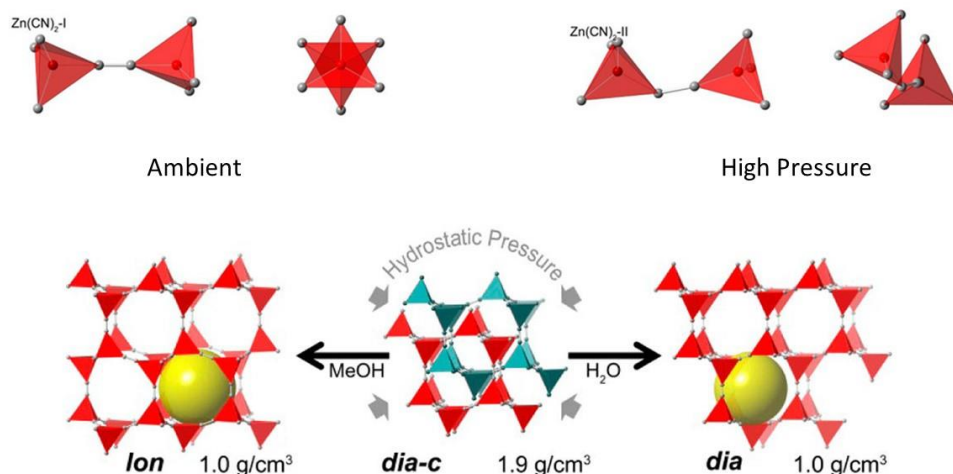


**Figure 1-12.** Phase transitions of  $\text{Zn}(\text{CN})_2$  upon compression in different fluid media. (ref. 91)

### 1.3.3 Chemical reactions

Recently, researchers found that chemical reactions of MOFs can be achieved by applying high external pressure to the frameworks, leading to bond breaking and formation. Pressure-induced bond rearrangement is very uncommon yet highly desirable in materials science and only two examples of such phenomenon in MOFs has been reported so far. The first example is a reversible pressure-induced bond rearrangement in erbium formate MOF  $[\text{Er}(\text{HCOO})_4]_2$  that undergoes a phase transition upon compression at about 0.6 GPa, in which the framework transforms from a 6-connecting uninodal *vmd* net to a new 8-connecting *vmt* net.<sup>96</sup> The second one is found in the family of zinc phosphonate MOFs, also known as zinc alkyl gates (ZAG). Two MOFs from this family, ZAG-4 and ZAG-6 have shown a pressure-induced reversible proton transfer between an included water molecule and the linker's phosphonate group, resulting negative linear compressibility of the framework at high pressure, as shown in Figure 1-13.<sup>97,98</sup> The MOFs in ZAG family provide new insight into crystal physics and properties, as well as practical applications as pressure-switchable proton conduction materials. The rare examples of pressure-induced chemical reactions show just how deep the field of pressure effects on MOFs is and encourage further studies to explore more novel and unexpected phenomena of MOFs under high pressure.

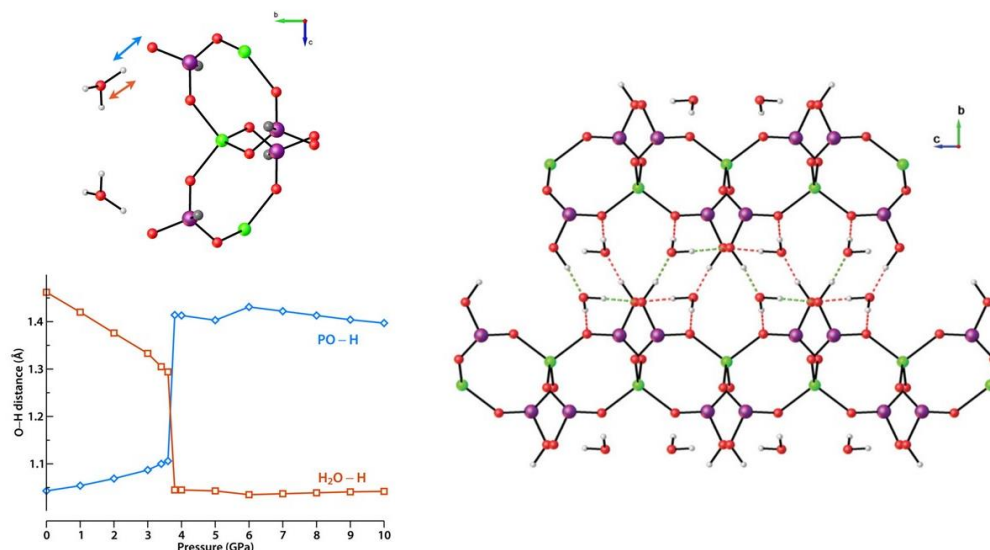


**Figure 1-13.** Pressure-induced proton jump in ZAG-4 and ZAG-6. (ref. 98)

### 1.3.4 High-pressure guest insertion

The interactions between the flexibility of MOFs and the adsorption of guests within their pores has attracted much attention in the MOF studies because such interplay is readily observed during adsorption measurements. In high-pressure range, one of the important research directions in this area is the use of high pressure to insert guest fluids into the pores of the frameworks, often triggering structural transformations of the host. Typically for such experiments, the MOFs sample is loaded with small molecular fluid or fluid mixture such as methanol, ethanol, etc., allowing the insertion of the guest into the framework. Early studies involved in HKUST-1<sup>99</sup> and ZIF-8<sup>100</sup> and more MOFs have been investigated on the high-pressure guest inclusion recently.<sup>101-105</sup> It was found that the pressure-induced insertion of fluids into the porous framework can lead to contraction, expansion, or structural transitions in the host framework as well as enhanced guest-host

interactions. In addition, the behavior of the host + guest system under compression can be very different from the host itself. The presence of guests inside the pores increases elastic moduli and diminishes compressibility, while improving resistance to delaying the onset of pressure-induced amorphization.<sup>106,107</sup> For instance, methanol can be forced into the pores of MOF  $\text{Sc}_2\text{BDC}_3$  as a pressure medium and located in two distinct sites, as illustrated in Figure 1-14.<sup>105</sup> Site 1 was filled at 0.3 GP and upon increasing pressure, the occupancy of the less favorable Site 2 increased as more methanol molecules were forced into the channels until a maximum uptake was reached at 1.1 GPa. Single crystal X-ray diffraction showed that  $\text{Sc}_2\text{BDC}_3$  maintained crystalline during methanol-mediated compression up to 3.0 GPa, in strong contrast to the amorphization of the framework at 0.4 GPa compressed with bulky pressure medium Fluorinert (fluorocarbon-based fluid). It is worth noting that the use of high pressures to saturate the pores of MOFs with guest molecules has potential applications in clean energy storage, such as pre-combustion  $\text{CO}_2$  capture which is performed at high pressures (10-100 bar).



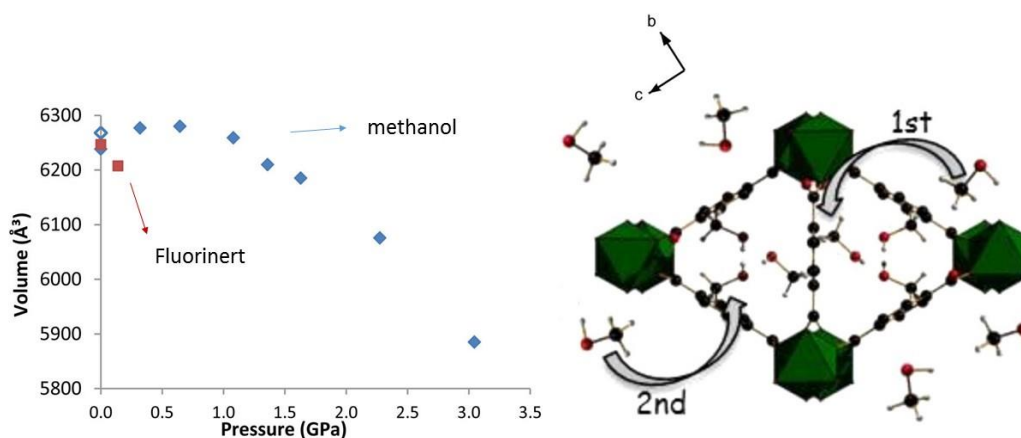


**Figure 1-14.** (a) Unit cell volume of  $\text{Sc}_2\text{BDC}_3$  in methanol and Fluorinert as a function of pressure; (b) pressure-induced methanol insertion in  $\text{Sc}_2\text{BDC}_3$ . (ref. 105)

## 1.4 Outline of the thesis

The main objectives of this thesis are to examine the chemical & structural stabilities of selected MOFs and their performance for  $\text{CO}_2$  storage under high pressures. The thesis is organized in the following way. *Chapter 2* discusses the stability of ZIF-8 in different pressure ranges probed by *in-situ* IR spectroscopy. Following *Chapter 2*, direct evidences of the interactions between  $\text{CO}_2$  and ZIF-8 as well as an enhanced  $\text{CO}_2$  storage in the framework were demonstrated in *Chapter 3*. The flexibility of the organic linker of ZIF-8 was found to play an important role in the  $\text{CO}_2$  adsorption mechanism. *Chapter 4* compares different pressure behavior among four MIL-68 (In) systems: the as-made MIL-68 (In), the activated framework, the activated sample loaded with nujol and the  $\text{CO}_2$ -loaded framework. Furthermore, the  $\text{CO}_2$  adsorption mechanism and the host-guest interactions are studied through *in-situ* IR spectroscopy as well as Grand Canonical Monte

Carlo simulations. *Chapter 5* describes the interplay between CO<sub>2</sub> and the  $\alpha$ -Mg<sub>3</sub>(HCOO)<sub>6</sub> framework, which undergoes a reversible amorphization upon compression. In *Chapter 6*, the stability and CO<sub>2</sub> storage in MOF CaSDB under high-pressure are investigated by *in situ* IR and Raman spectroscopy. The CaSDB framework shows a remarkable affinity towards CO<sub>2</sub> and an enhanced CO<sub>2</sub>-metal interaction is found as evidenced by far-IR measurements. As guest molecules, CO<sub>2</sub> substantially influences the structure of CaSDB and triggers a crystal-to-crystal phase transition of the framework at high pressures. *Chapter 7* is the final chapter, in which a brief summary of the thesis and some suggestions for future work are provided.

## 1.5 Reference

- (1) Li, H.; Eddaoudi, M.; O'Keeffe, M.; Yaghi, O. M. *Nature* **1999**, *402*, 276.
- (2) Eddaoudi, M.; Kim, J.; Rosi, N.; Vodak, D.; Wachter, J.; O'Keeffe, M.; Yaghi, O. M. *Science* **2002**, *295*, 469.
- (3) Garibay, S. J.; Cohen, S. M. *Chemical Communications* **2010**, *46*, 7700.
- (4) Cavka, J. H.; Jakobsen, S.; Olsbye, U.; Guillou, N.; Lamberti, C.; Bordiga, S.; Lillerud, K. P. *Journal of the American Chemical Society* **2008**, *130*, 13850.
- (5) Biswas, S.; Ahnfeldt, T.; Stock, N. *Inorganic Chemistry* **2011**, *50*, 9518.
- (6) Serre, C.; Millange, F.; Thouvenot, C.; Noguès, M.; Marsolier, G.; Louër, D.; Férey, G. *Journal of the American Chemical Society* **2002**, *124*, 13519.
- (7) Lin, X.; Telepeni, I.; Blake, A. J.; Dailly, A.; Brown, C. M.; Simmons, J. M.; Zoppi, M.; Walker, G. S.; Thomas, K. M.; Mays, T. J.; Hubberstey, P.; Champness, N. R.; Schröder, M. *Journal of the American Chemical Society* **2009**, *131*, 2159.
- (8) Furukawa, H.; Cordova, K. E.; O'Keeffe, M.; Yaghi, O. M. *Science* **2013**, *341*, 1230444.
- (9) He, Y.; Zhou, W.; Qian, G.; Chen, B. *Chemical Society Reviews* **2014**, *43*, 5657.
- (10) Sumida, K.; Rogow, D. L.; Mason, J. A.; McDonald, T. M.; Bloch, E. D.; Herm, Z. R.; Bae, T. H.; Long, J. R. *Chemical Reviews* **2012**, *112*, 724.

- (11) Suh, M. P.; Park, H. J.; Prasad, T. K.; Lim, D.-W. *Chemical Reviews* **2012**, *112*, 782.
- (12) Li, J.-R.; Sculley, J.; Zhou, H.-C. *Chemical Reviews* **2012**, *112*, 869.
- (13) Ranocchiari, M.; Bokhoven, J. A. v. *Physical Chemistry Chemical Physics* **2011**, *13*, 6388.
- (14) Horcajada, P.; Gref, R.; Baati, T.; Allan, P. K.; Maurin, G.; Couvreur, P.; Férey, G.; Morris, R. E.; Serre, C. *Chemical Reviews* **2012**, *112*, 1232.
- (15) Kreno, L. E.; Leong, K.; Farha, O. K.; Allendorf, M.; Van Duyne, R. P.; Hupp, J. T. *Chemical Reviews* **2012**, *112*, 1105.
- (16) Rochelle, G. T. *Science* **2009**, *325*, 1652.
- (17) Blanchon le Bouhelec, E.; Mougín, P.; Barreau, A.; Solimando, R. *Energy & Fuels* **2007**, *21*, 2044.
- (18) Ghoufi, A.; Gaberova, L.; Rouquerol, J.; Vincent, D.; Llewellyn, P. L.; Maurin, G. *Microporous and Mesoporous Materials* **2009**, *119*, 117.
- (19) Himeno, S.; Tomita, T.; Suzuki, K.; Yoshida, S. *Microporous and Mesoporous Materials* **2007**, *98*, 62.
- (20) Cavenati, S.; Grande, C. A.; Rodrigues, A. E. *Chemical Engineering Science* **2006**, *61*, 3893.
- (21) Cavenati, S.; Grande, C. A.; Rodrigues, A. E. *Journal of Chemical & Engineering Data* **2004**, *49*, 1095.
- (22) Kusakabe, K.; Kuroda, T.; Murata, A.; Morooka, S. *Industrial & Engineering Chemistry Research* **1997**, *36*, 649.
- (23) Bezerra, D.; Oliveira, R.; Vieira, R.; Cavalcante, C., Jr.; Azevedo, D. S. *Adsorption* **2011**, *17*, 235.
- (24) Dogru, M.; Sonnauer, A.; Gavryushin, A.; Knochel, P.; Bein, T. *Chemical Communications* **2011**, *47*, 1707.
- (25) Choi, Y. J.; Choi, J. H.; Choi, K. M.; Kang, J. K. *Journal of Material Chemistry* **2011**, *21*, 1073.
- (26) El-Kaderi, H. M.; Hunt, J. R.; Mendoza-Cortés, J. L.; Côté, A. P.; Taylor, R. E.; O'Keeffe, M.; Yaghi, O. M. *Science* **2007**, *316*, 268.
- (27) Côté, A. P.; El-Kaderi, H. M.; Furukawa, H.; Hunt, J. R.; Yaghi, O. M. *Journal of the American Chemical Society* **2007**, *129*, 12914.
- (28) Hicks, J. C.; Drese, J. H.; Fauth, D. J.; Gray, M. L.; Qi, G.; Jones, C. W. *Journal of the American Chemical Society* **2008**, *130*, 2902.
- (29) Xu, X.; Song, C.; Andrésen, J. M.; Miller, B. G.; Scaroni, A. W. *Microporous and Mesoporous Materials* **2003**, *62*, 29.

- (30) Chae, H. K.; Siberio-Perez, D. Y.; Kim, J.; Go, Y.; Eddaoudi, M.; Matzger, A. J.; O'Keeffe, M.; Yaghi, O. M. *Nature* **2004**, *427*, 523.
- (31) Millward, A. R.; Yaghi, O. M. *Journal of the American Chemical Society* **2005**, *127*, 17998.
- (32) Arstad, B.; Fjellvåg, H.; Kongshaug, K.; Swang, O.; Blom, R. *Adsorption* **2008**, *14*, 755.
- (33) Zeleňák, V.; Vargová, Z.; Almáši, M.; Zeleňáková, A.; Kuchár, J. *Microporous and Mesoporous Materials* **2010**, *129*, 354.
- (34) Beobide, G.; Wang, W.-g.; Castillo, O.; Luque, A.; Román, P.; Tagliabue, G.; Galli, S.; Navarro, J. A. R. *Inorganic Chemistry* **2008**, *47*, 5267.
- (35) Vaidhyanathan, R.; Iremonger, S. S.; Dawson, K. W.; Shimizu, G. K. H. *Chemical Communications* **2009**, *35*, 5230.
- (36) Demessence, A.; D'Alessandro, D. M.; Foo, M. L.; Long, J. R. *Journal of the American Chemical Society* **2009**, *131*, 8784.
- (37) McDonald, T. M.; D'Alessandro, D. M.; Krishna, R.; Long, J. R. *Chemical Science* **2011**, *2*, 2022.
- (38) Phan, A.; Doonan, C. J.; Uribe-Romo, F. J.; Knobler, C. B.; O'Keeffe, M.; Yaghi, O. M. *Accounts of Chemical Research* **2010**, *43*, 58.
- (39) Furukawa, H.; Kim, J.; Ockwig, N. W.; O'Keeffe, M.; Yaghi, O. M. *Journal of the American Chemical Society* **2008**, *130*, 11650.
- (40) Park, H. J.; Suh, M. P. *Chemical Communications* **2010**, *46*, 610.
- (41) Kim, T. K.; Suh, M. P. *Chemical Communications* **2011**, *47*, 4258.
- (42) Banerjee, R.; Furukawa, H.; Britt, D.; Knobler, C.; O'Keeffe, M.; Yaghi, O. M. *Journal of the American Chemical Society* **2009**, *131*, 3875.
- (43) Morris, W.; Leung, B.; Furukawa, H.; Yaghi, O. K.; He, N.; Hayashi, H.; Houndonougbo, Y.; Asta, M.; Laird, B. B.; Yaghi, O. M. *Journal of the American Chemical Society* **2010**, *132*, 11006.
- (44) Thallapally, P. K.; Tian, J.; Radha Kishan, M.; Fernandez, C. A.; Dalgarno, S. J.; McGrail, P. B.; Warren, J. E.; Atwood, J. L. *Journal of the American Chemical Society* **2008**, *130*, 16842.
- (45) Fernandez, C. A.; Thallapally, P. K.; Motkuri, R. K.; Nune, S. K.; Sumrak, J. C.; Tian, J.; Liu, J. *Crystal Growth & Design* **2010**, *10*, 1037.
- (46) Inubushi, Y.; Horike, S.; Fukushima, T.; Akiyama, G.; Matsuda, R.; Kitagawa, S. *Chemical Communications* **2010**, *46*, 9229.
- (47) Liang, J.; Shimizu, G. K. H. *Inorganic Chemistry* **2007**, *46*, 10449.

- (48) Chui, S. S.-Y.; Lo, S. M.-F.; Charmant, J. P. H.; Orpen, A. G.; Williams, I. D. *Science* **1999**, 283, 1148.
- (49) Vimont, A.; Goupil, J.-M.; Lavalley, J.-C.; Daturi, M.; Surblé S.; Serre, C.; Millange, F.; Férey, G.; Audebrand, N. *Journal of the American Chemical Society* **2006**, 128, 3218.
- (50) Dincă, M.; Long, J. R. *Angewandte Chemie International Edition* **2008**, 47, 6766.
- (51) Zhou, W.; Wu, H.; Yildirim, T. *Journal of the American Chemical Society* **2008**, 130, 15268.
- (52) Dietzel, P. D. C.; Besikiotis, V.; Blom, R. *Journal of Materials Chemistry* **2009**, 19, 7362.
- (53) Chen, B.; Xiang, S.; Qian, G. *Accounts of Chemical Research* **2010**, 43, 1115.
- (54) Caskey, S. R.; Wong-Foy, A. G.; Matzger, A. J. *Journal of the American Chemical Society* **2008**, 130, 10870.
- (55) Weir, C. E. L., E. R.; Valkenburg, A. V.; Bunting, E. N. *Journal of Research of the National Bureau of Standards, Section A: Physics and Chemistry* **1959**, 63, 55.
- (56) Hemley, R. J. *Annual Review of Physical Chemistry* **2000**, 51, 763.
- (57) Grochala, W.; Hoffmann, R.; Feng, J.; Ashcroft, N. W. *Angewandte Chemie International Edition* **2007**, 46, 3620.
- (58) Jayaraman, A. *Reviews of Modern Physics* **1983**, 55, 65.
- (59) Jeanloz, R. *Annual Review of Physical Chemistry* **1989**, 40, 237.
- (60) Tapper, R. J. *Reports on Progress in Physics* **2000**, 63, 1273.
- (61) MAO, H. K. *Science* **1978**, 200, 1145.
- (62) XU, J. A.; MAO, H. K.; BELL, P. M. *Science* **1986**, 232, 1404.
- (63) Mao, H. K.; Xu, J.; Bell, P. M. *Journal of Geophysical Research: Solid Earth* **1986**, 91, 4673.
- (64) Ferraro, J. R.; Nakamoto, K.; Brown, C. W. *Introductory Raman Spectroscopy (Second Edition)* **2003**, Academic Press, San Diego.
- (65) Dong, Z. H.; Song, Y. *Journal of Physical Chemistry C* **2010**, 114, 1782.
- (66) Dong, Z. H., Ph.D. Thesis **2012**.
- (67) Hemley, R. J. M., H. K.; Struzhkin, V. V. *Journal of Synchrotron Radiation* **2005**, 12, 135.
- (68) Giordano, V. M.; Gorelli, F. A.; Bini, R.; *Low Temperature Physics*, **2006**, 32, 1402.
- (69) Aoki, K.; Yamawaki, H.; Sakashita, M. *Physical Review B* **1993**, 48, 9231.

- (70) Olijnyk, H.; Däifer, H.; Jodl, H.J.; Hochheimer, H. D. *The Journal of Chemical Physics* **1988**, *88*, 4204.
- (71) Coudert, F.-X. *Chemistry of Materials* **2015**, *27*, 1905.
- (72) Gatta, G. D. In *High-Pressure Crystallography: From Fundamental Phenomena to Technological Applications*; Boldyreva, E., Dera, P., Eds.; Springer: Dordrecht, **2010**, 481.
- (73) Greaves, G. N.; Meneau, F.; Kargl, F.; Ward, D.; Holliman, P.; Albergamo, F. *Journal of Physics: Condensed Matter* **2007**, *19*, 415102.
- (74) Greaves, G. N. *Compressibility, pressure-induced amorphisation and thermal collapse of zeolites*; Springer: Dordrecht, **2001**, *48*, 53.
- (75) Su, Z.; Miao, Y.-R.; Mao, S.-M.; Zhang, G.-H.; Dillon, S.; Miller, J. T.; Suslick, K. S. *Journal of the American Chemical Society* **2015**, *137*, 1750.
- (76) Bennett, T. D.; Sotelo, J.; Tan, J.-C.; Moggach, S. A. *CrystEngComm* **2015**, *17*, 286.
- (77) Tan, J. C.; Bennett, T. D.; Cheetham, A. K. *Proceedings of the National Academy of Sciences* **2010**, *107*, 9938.
- (78) Bennett, T. D.; Tan, J. C.; Moggach, S. A.; Galvelis, R.; Mellot-Draznieks, C.; Reisner, B. A.; Thirumurugan, A.; Allan, D. R.; Cheetham, A. K. *Chemistry - A European Journal* **2010**, *16*, 10684.
- (79) Tan, J. C.; Furman, J. D.; Cheetham, A. K. *Journal of the American Chemical Society* **2009**, *131*, 14252.
- (80) Tan, J. C.; Cheetham, A. K. *Chemical Society Reviews* **2011**, *40*, 1059.
- (81) Ogborn, J. M.; Collings, I. E.; Moggach, S. A.; Thompson, A. L.; Goodwin, A. L. *Chemical Science* **2012**, *3*, 3011.
- (82) Li, W.; Probert, M. R.; Kosa, M.; Bennett, T. D.; Thirumurugan, A.; Burwood, R. P.; Parinello, M.; Howard, J. A. K.; Cheetham, A. K. *Journal of the American Chemical Society* **2012**, *134*, 11940.
- (83) Cai, W.; Katrusiak, A. *Nature communications* **2014**, *5*, 4337.
- (84) Serra-Crespo, P.; Dikhtiarenko, A.; Stavitski, E.; Juan-Alcaniz, J.; Kapteijn, F.; Coudert, F.-X.; Gascon, J. *CrystEngComm* **2015**, *17*, 276.
- (85) Ortiz, A. U.; Boutin, A.; Fuchs, A. H.; Coudert, F.-X. *Physical Review Letters* **2012**, *109*, 195502.
- (86) Ortiz, A. U.; Boutin, A.; Fuchs, A. H.; Coudert, F.-X. *The Journal of Physical Chemistry Letters* **2013**, *4*, 1861.
- (87) Chapman, K. W.; Halder, G. J.; Chupas, P. J. *Journal of the American Chemical Society* **2009**, *131*, 17546.

- (88) Cao, S.; Bennett, T. D.; Keen, D. A.; Goodwin, A. L.; Cheetham, A. K. *Chemical Communications* **2012**, *48*, 7805.
- (89) Bennett, T. D.; Simoncic, P.; Moggach, S. A.; Gozzo, F.; Macchi, P.; Keen, D. A.; Tan, J.-C.; Cheetham, A. K. *Chemical Communications* **2011**, *47*, 7983.
- (90) Bouëssel du Bourg, L.; Ortiz, A. U.; Boutin, A.; Coudert, F.-X. *APL Materials* **2014**, *2*, 124110.
- (91) Lapidus, S. H.; Halder, G. J.; Chupas, P. J.; Chapman, K. W. *Journal of the American Chemical Society* **2013**, *135*, 7621.
- (92) Beurroies, I.; Boulhout, M.; Llewellyn, P. L.; Kuchta, B.; Férey, G.; Serre, C.; Denoyel, R. *Angewandte Chemie International Edition* **2010**, *49*, 7526.
- (93) Neimark, A. V.; Coudert, F.-X.; Triguero, C.; Boutin, A.; Fuchs, A. H.; Beurroies, I.; Denoyel, R. *Langmuir* **2011**, *27*, 4734.
- (94) Yot, P. G.; Ma, Q.; Haines, J.; Yang, Q.; Ghoufi, A.; Devic, T.; Serre, C.; Dmitriev, V.; Férey, G.; Zhong, C.; Maurin, G. *Chemical Science* **2012**, *3*, 1100.
- (95) Zhou, M.; Wang, K.; Men, Z.; Sun, C.; Li, Z.; Liu, B.; Zou, G.; Zou, B. *CrystEngComm* **2014**, *16*, 4084.
- (96) Spencer, E. C.; Kiran, M. S. R. N.; Li, W.; Ramamurty, U.; Ross, N. L.; Cheetham, A. K. *Angewandte Chemie International Edition* **2014**, *53*, 5583.
- (97) Gagnon, K. J.; Beavers, C. M.; Clearfield, A. *Journal of the American Chemical Society* **2013**, *135*, 1252.
- (98) Ortiz, A. U.; Boutin, A.; Gagnon, K. J.; Clearfield, A.; Coudert, F.-X. *Journal of the American Chemical Society* **2014**, *136*, 11540.
- (99) Chapman, K. W.; Halder, G. J.; Chupas, P. J. *Journal of the American Chemical Society* **2008**, *130*, 10524.
- (100) Moggach, S. A.; Bennett, T. D.; Cheetham, A. K. *Angewandte Chemie International Edition* **2009**, *48*, 7087.
- (101) Hu, Y.; Liu, Z.; Xu, J.; Huang, Y.; Song, Y. *Journal of the American Chemical Society* **2013**, *135*, 9287.
- (102) Graham, A. J.; Tan, J.-C.; Allan, D. R.; Moggach, S. A. *Chemical Communications* **2012**, *48*, 1535.
- (103) Graham, A. J.; Allan, D. R.; Muszkiewicz, A.; Morrison, C. A.; Moggach, S. A. *Angewandte Chemie International Edition* **2011**, *50*, 11138.
- (104) Chapman, K. W.; Sava, D. F.; Halder, G. J.; Chupas, P. J.; Nenoff, T. M. *Journal of the American Chemical Society* **2011**, *133*, 18583.

- (105) Graham, A. J.; Banu, A.-M.; Duren, T.; Greenaway, A.; McKellar, S. C.; Mowat, J. P. S.; Ward, K.; Wright, P. A.; Moggach, S. A. *Journal of the American Chemical Society* **2014**, *136*, 8606.
- (106) Coasne, B.; Haines, J.; Levelut, C.; Cambon, O.; Santoro, M.; Gorelli, F.; Garbarino, G. *Physical Chemistry Chemical Physics* **2011**, *13*, 20096.
- (107) Haines, J.; Cambon, O.; Levelut, C.; Santoro, M.; Gorelli, F.; Garbarino, G. *Journal of the American Chemical Society* **2010**, *132*, 8860.



## Chapter 2

### 2 *In Situ* High Pressure Study of ZIF-8 by IR Spectroscopy\*

#### 2.1 Introduction

ZIFs, short for zeolitic imidazolate frameworks, are an emerging class of porous materials with extended 3D crystalline structures constructed from tetrahedral metal ions (Zn, Co, In, etc.) bridged by imidazolate (Im) units. Up to date, a large variety of ZIFs with rich structural and topological diversity have been made by virtue of the flexibility with which the metals and links can be varied.<sup>1,2</sup> In the ZIF family, ZIF-8 [Zn(MeIm)<sub>2</sub>, MeIm = 2-methylimidazolate] has been widely studied due to its tunable pore size, chemical stability and thermal robustness, which make it a promising candidate for gas storage,<sup>3</sup> molecular separation,<sup>4</sup> catalysis<sup>5,6</sup> and so on. The topology of ZIF-8 corresponds to the zeolite sodalite, which can be described as a space-filling packing of truncated octahedrons.<sup>2</sup> In particular, it crystallizes in a cubic lattice (space group I-43m) that contains cavities with a diameter of 11.6 Å connected via 6-ring apertures with a 3.5 Å window and 4-ring apertures (see Fig. 2-1).

---

\* The content of this chapter has been published as: Hu, Y.; Kazemian, H.; Rohani, S.; Huang Y. and Song, Y. *Chemical Communications*, **2011**, 47, 12694.

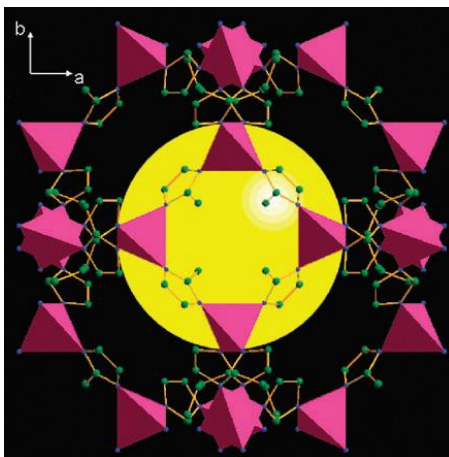


**Figure 2-1.** Crystal structure of ZIF-8 viewed along the  $c$ -axis. The pink polyhedrons denote the  $\text{ZnN}_4$  units. The yellow sphere indicates the space in the cage.

In contrast to the extensive studies under ambient conditions and at different temperatures,<sup>7</sup> ZIF-8 has only been studied under pressure in a very limited range.<sup>8-11</sup> It is well known that pressure can influence the structures, physical and chemical properties and performance of nanoporous materials.<sup>12</sup> Therefore, pressure provides a new approach to achieve structural modification which includes changes in pore size, opening and geometry, channel shape and internal surface area. Subsequently, these pressure-induced changes will affect the sorption selectivity, capacity and access to the binding sites of the porous materials. Indeed, pressure has been used to tune the sorption properties of ZIF-8. For instance, Moggach *et al.* reported that ZIF-8 undergoes a reversible crystalline-to-crystalline phase transition at around 1.5 GPa in some pressure transmitting medium (PTM).<sup>11</sup> The interaction between the PTM and ZIF-8 nanopore was believed to play an important role in the phase transition. This study demonstrated that pressure could be used to modify the pore size, shape and volume, eventually increasing the accessible surface area for gas storage materials. In parallel, Chapman *et al.* showed that compression of ZIF-

8 at very low pressures (e.g., 0.34 GPa) resulted in an irreversible structural transition and amorphization upon recovery to ambient pressure.<sup>9</sup> The amorphization behavior was found to be independent of whether a PTM was used or not. These different results not only involve guest–host interactions, but may be due to the intrinsic detailed intra-molecular chemical responses of ZIF-8 to compression. While X-ray diffraction provides information about structural evolution of the crystal lattice, vibrational spectroscopy allows the understanding of pressure effects on chemical bonding and especially local structures. Here we report the first *in situ* infrared (IR) absorption spectroscopic study of ZIF-8 under high pressures.

## 2.2 Experimental section

The ZIF-8 sample was synthesized according to the literature.<sup>13</sup> A solution of  $\text{Zn}(\text{NO}_3)_2 \cdot 6\text{H}_2\text{O}$  (2.933 g, 9.87 mmol) in 200 mL of methanol is rapidly poured into a solution of 2-methylimidazole (6.489 g, 79.04 mmol) in 200 mL of methanol under stirring with a magnetic bar. The mixture slowly turns turbid and after 1 h the nanocrystals are separated from the milky dispersion by centrifugation and washing with fresh methanol. The nanocrystals are dried at 40 °C in air. Yield is 50 % based on zinc. The solvent molecules can be removed from the as-made sample through thermal activation at 200 °C for 6 hours. The crystallinity, morphology and porosity of the activated sample were checked by XRD, SEM and BET, respectively. A diamond anvil cell (DAC) equipped with type II diamonds with culet sizes of 400 and 600  $\mu\text{m}$  was used to generate high pressures. The pure desolvated samples were loaded into the DAC without KBr or any other fluid PTM to rule out the possible guest–host interactions. The samples were 150–200  $\mu\text{m}$  in

diameter and  $\sim 30 \mu\text{m}$  thick. A few Ruby chips were inserted as the pressure calibrant. A customized IR micro-spectroscopy system with details described in *Chapter 1* was used for all IR absorption measurements.<sup>14</sup> Multiple runs were carried out for reproducibility and all measurements were performed under room temperature. During both compression and decompression and in between runs, sufficiently long time was allowed for equilibrium to rule out any kinetic effect and no time dependent behavior was observed.

## 2.3 Results

### 2.3.1 IR spectra of ZIF-8 upon compression to 39 GPa

Fig. 2-2 (a) shows the selected IR spectra of ZIF-8 on compression to 39.15 GPa and then decompression to ambient pressure. As a starting point, our ambient pressure IR measurement is in excellent agreement with that reported by Ordonez *et al.*<sup>15</sup> The complete assignment of the observed IR bands is difficult due to the complex nature of the ZIF-8 framework. However, most of the absorption bands are associated with the vibrations of the imidazole units and thus can be described based on the origin of the bonds. For example, the bands at 3135 and 2929  $\text{cm}^{-1}$  are attributed to the aromatic and the aliphatic C–H stretch of the imidazole, respectively. The peak at 1584  $\text{cm}^{-1}$  can be assigned as the C=N stretch mode specifically,<sup>15</sup> whereas the intense and convoluted bands at 1350–1500  $\text{cm}^{-1}$  are associated with the entire ring stretching. The bands in the spectral region from 900 to 1350  $\text{cm}^{-1}$  are for the in-plane bending of the ring while those below 800  $\text{cm}^{-1}$  are assigned as out-of-plane bending. Due to the limitation of our IR apparatus (i.e., for mid-IR measurements only), the bonding between the metal and organic ligand, i.e., the Zn–N stretch mode which is expected at 421  $\text{cm}^{-1}$  was not observed.

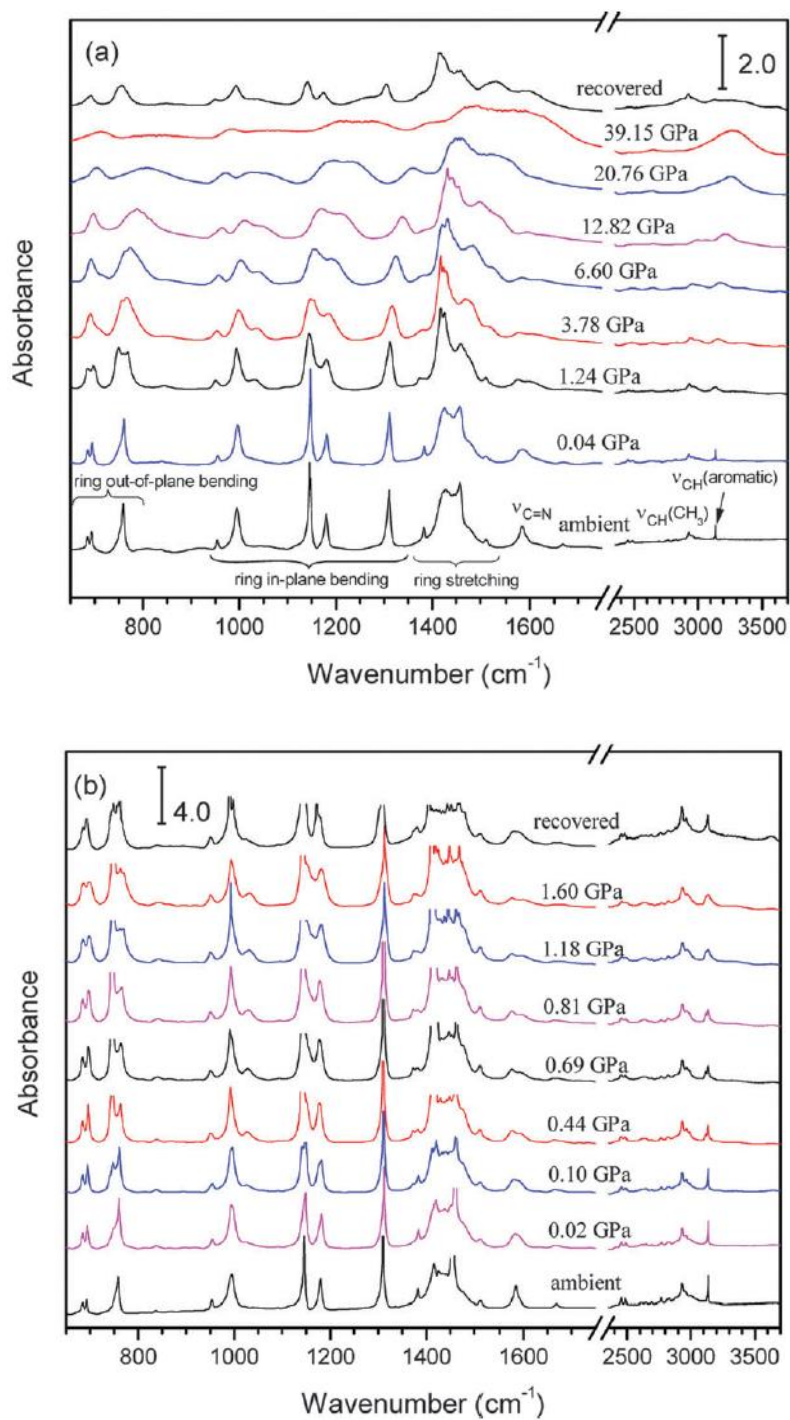


**Figure 2-2.** Selected IR spectra of ZIF-8 on compression to a highest pressure of 39.15 GPa and as recovered (a), and to another highest pressure of 1.60 GPa and as recovered (b)

Upon compression to 1.24 GPa, most of the IR absorption bands exhibited significant changes. For example, the aromatic C–H stretch mode at  $3135\text{ cm}^{-1}$ , the C=N stretch mode at  $1584\text{ cm}^{-1}$ , and an out-of-plane bending mode at  $760\text{ cm}^{-1}$  were all broadened and split. Band splitting typically suggests enhanced intermolecular interactions, in this case, the ring-ring interaction of the ZIF-8 framework within the unit cell. Other changes include the significant enhancement of one of the ring stretch modes at  $1420\text{ cm}^{-1}$  and the appearance of a new IR band at  $1031\text{ cm}^{-1}$ . Further compression resulted in continuous broadening accompanied by mode merging. At the highest pressure of 39.15 GPa, the IR profile can be characterized by an extremely broadened pattern, indicating the transformation to disordered or amorphous structure, in accord with Chapman *et al.*'s observation above 0.3 GPa.<sup>9</sup> Then the IR spectra of ZIF-8 were collected upon decompression all the way back to ambient pressure. The pressure evolutions were observed in the reverse sequence as expected. Upon complete decompression, however, the spectrum of the recovered sample only resembles that at around 4 GPa instead of the initial ambient-pressure spectrum before compression especially in the ring stretch region as well as the C=N and the C–H stretch regions, indicating that the framework has been partially modified. Nonetheless, all other major IR bands of the recovered sample are still characteristic of the imidazole ring, indicating that the entire ZIF-8 framework has survived a compression pressure of 39.15 GPa without a permanent breakdown although the local structures might have been modified.

### 2.3.2 IR spectra of ZIF-8 upon compression to 1.6 GPa

We then focused on a lower and narrower pressure region where the modification might be completely reversible. Fig. 2-2 (b) shows the selected IR spectra of ZIF-8 on compression to a highest pressure of 1.60 GPa followed by decompression. In this pressure region, although pressure-induced band broadening was also observed, there was no significant change of the entire IR profile in general, except that an out-of-plane bending mode (band 3) exhibited a splitting at 0.1 GPa. The recovered material exhibited a very similar profile to, but not exactly the same as the original sample, in strong contrast to that compressed to 39.15 GPa. In particular, the C=N stretch mode and both the aromatic and the aliphatic C–H stretch modes were clearly recovered. These observations suggest that the structural modifications of ZIF-8 were mostly reversible in the lower pressure region in which the crystallinity and framework structure are highly preserved, consistent with the structure and reversibility of the phase below 1.47 GPa reported by Moggach *et al.*<sup>11</sup> using X-ray methods.

## 2.4 Discussion

The above two runs established that different highest compression pressures resulted in different reversibilities. Thus we monitored the pressure dependence of IR modes of ZIF-8 in the respective two compression regions, i.e., 0–1.6 GPa and 2–14 GPa, as shown in Fig. 2-3. The pressure coefficients were analyzed by least-square fitting of the experimental data and are reported in Table 2-1. In general, the pressure coefficients are extremely small in magnitude (i.e.,  $< 5 \text{ cm}^{-1}/\text{GPa}$ ), indicating that the bond strength is not very sensitive to compression in a broad pressure region. In the pressure region of  $> 2 \text{ GPa}$ ,

the IR modes exhibited regular pressure-induced blue shifts, consistent with that the bonds become stiffened upon compression. In contrast, some of the IR modes (e.g., bands 4, 5, 6 and 9) exhibited a significant red shift in the pressure region below 1.6 GPa. The soft behavior (i.e., negative pressure coefficients) is typically associated with bond weakening processes that may ultimately lead to a phase transition. The largest negative pressure dependence of the C=N stretching mode as well as other soft in-plane ring bending modes most likely originates from the weakening of the  $\pi$  bonds, resulting from a slight ring distortion.

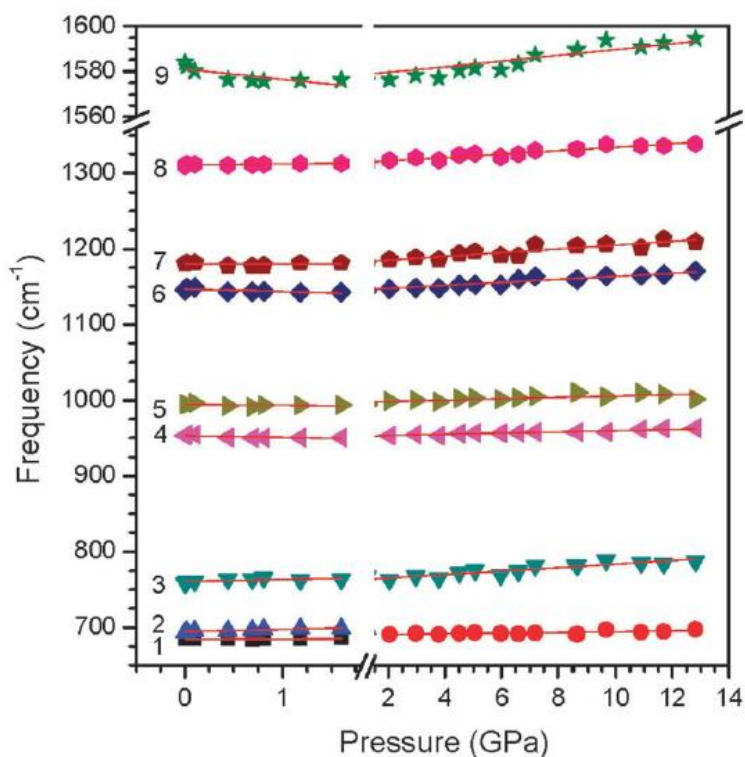


**Figure 2-3.** Pressure dependence of selected IR modes of ZIF-8 on compression in the pressure region of 0–1.6 GPa and 2–14 GPa.



**Table 2-1.** Pressure dependence ( $dv/dP$ ,  $\text{cm}^{-1}/\text{GPa}$ ) of IR modes of ZIF-8 on compression

<b>Mode</b>	<b>Frequency (<math>\text{cm}^{-1}</math>)</b>	<b>0-1.6 GPa</b>	<b>1.6-12.8 GPa</b>
<b>1</b>	684	0.72	0.47
<b>2</b>	693	2.89	
<b>3</b>	758	2.40	2.32
<b>4</b>	953	-2.57	0.79
<b>5</b>	995	-1.00	0.95
<b>6</b>	1146	-3.34	1.98
<b>7</b>	1180	-0.02	2.48
<b>8</b>	1310	1.23	2.27
<b>9</b>	1584	-4.42	1.27

Finally, when combined with previous X-ray studies of high-pressure behavior, our results provide interesting implications about the stabilities of ZIF-8 and thus its potential applications. First of all, all the high-pressure studies so far suggest that the lattice stabilities were greatly reduced without a penetrating PTM. However, the chemical stability probed by the current IR study seems independent of the crystalline state and surprisingly high compared to isolated aromatic systems that typically break down at even very moderate pressures.<sup>16</sup> This property makes ZIF-8 a promising storage material for applications that require extreme loading pressures. Furthermore, the pressure effect on the pore size of ZIF-8 is of great interest for its storage capacity. Moggach *et al.* showed that the pore size of ZIF-8 can be enlarged with the incorporation of the PTM molecules by free rotation of the imidazole rings, whereas Chapman *et al.* reported a monotonic decrease in unit cell volume upon compression. Our IR results in the pressure region of  $< 1.6$  GPa, however, suggest that even without a PTM, the pore size may remain constant with enough rigidity despite the ring weakening upon compression. Even in the amorphous phase, the small pressure coefficients nonetheless suggest that the nanopores are not sensitive to and may survive extreme compressions. This is especially desirable to extend the storage applications of ZIF-8 to much broader physical conditions.

## 2.5 Conclusions

In summary, we obtained the first in situ IR spectra of ZIF-8 under high pressures up to  $\sim 39$  GPa. Upon compression to 1.6 GPa followed by decompression, the pressure effects on the ZIF-8 framework were found to be reversible. Further compression to higher pressures resulted in irreversible structural transitions to a disordered or amorphous phase.

However, the chemical structure of the framework was found to sustain extreme compression without breaking down. The compression behavior and especially the surprising chemical stability probed by *in situ* IR spectroscopy provide new insight into the storage applications of ZIF-8.

## 2.6 References

- (1) Park, K. S.; Ni, Z.; Cote, A. P.; Choi, J. Y.; Huang, R. D.; Uribe-Romo, F. J.; Chae, H. K.; O'Keeffe, M.; Yaghi, O. M. *Proceedings of the National Academy of Sciences of the United States of America* **2006**, *103*, 10186.
- (2) Phan, A.; Doonan, C. J.; Uribe-Romo, F. J.; Knobler, C. B.; O'Keeffe, M.; Yaghi, O. M. *Accounts of Chemical Research* **2010**, *43*, 58.
- (3) Morris, R. E.; Wheatley, P. S. *Angewandte Chemie International Edition* **2008**, *47*, 4966.
- (4) Li, K.; Olson, D. H.; Seidel, J.; Emge, T. J.; Gong, H.; Zeng, H.; Li, J. *Journal of the American Chemical Society* **2009**, *131*, 10368.
- (5) Jiang, H.-L.; Liu, B.; Akita, T.; Haruta, M.; Sakurai, H.; Xu, Q. *Journal of the American Chemical Society* **2009**, *131*, 11302.
- (6) Tran, U. P. N.; Le, K. K. A.; Phan, N. T. S. *ACS Catalysis* **2011**, *1*, 120.
- (7) Zhou, W.; Wu, H.; Udovic, T. J.; Rush, J. J.; Yildirim, T. *The Journal of Physical Chemistry A* **2008**, *112*, 12602.
- (8) Bennett, T. D.; Tan, J. C.; Moggach, S. A.; Galvelis, R.; Mellot-Draznieks, C.; Reisner, B. A.; Thirumurugan, A.; Allan, D. R.; Cheetham, A. K. *Chemistry-A European Journal* **2010**, *16*, 10684.
- (9) Chapman, K. W.; Halder, G. J.; Chupas, P. J. *Journal of the American Chemical Society* **2009**, *131*, 17546.
- (10) Fairen-Jimenez, D.; Moggach, S. A.; Wharmby, M. T.; Wright, P. A.; Parsons, S.; Duren, T. *Journal of the American Chemical Society* **2011**, *133*, 8900.
- (11) Moggach, S. A.; Bennett, T. D.; Cheetham, A. K. *Angewandte Chemie International Edition* **2009**, *48*, 7087.
- (12) Fu, Y. Q.; Song, Y.; Huang, Y. I. *Journal of Physical Chemistry C* **2012**, *116*, 2080.
- (13) Isimjan, T. T.; Kazemian, H.; Rohani, S.; Ray, A. K. *Journal of Material Chemistry* **2010**, *20*, 10241.

- (14) Dong, Z. H.; Song, Y. *Journal of Physical Chemistry C* **2010**, *114*, 1782.
- (15) Ordoñez, M. J. C.; Balkus Jr, K. J.; Ferraris, J. P.; Musselman, I. H. *Journal of Membrane Science* **2010**, *361*, 28.
- (16) Zhuravlev, K. K.; Traikov, K.; Dong, Z.; Xie, S.; Song, Y.; Liu, Z. *Physical Review B* **2010**, *82*, 064116.

## Chapter 3

### 3 Evidence of Pressure Enhanced CO<sub>2</sub> Storage in ZIF-8 Probed by FTIR Spectroscopy\*

#### 3.1 Introduction

Zeolitic imidazolate frameworks (ZIFs) are an emerging class of metal-organic framework (MOF) materials that could serve as an effective platform for the capture and storage of CO<sub>2</sub> due to their ordered structures, high thermal stability, very high porosity and adjustable chemical functionality.<sup>1-4</sup> In the large ZIF family, ZIF-8 [Zn(MeIm)<sub>2</sub>, MeIm = 2-methylimidazolate] is one of the most studied ZIFs featuring a cubic lattice (space group *I*-43m) and sodalite (SOD) topology that contains cavities with a diameter of 11.6 Å connected via 6-ring apertures with a 3.4 Å window and 4-ring apertures.<sup>3</sup> Adsorption studies of various gases (e.g., CO<sub>2</sub>, CH<sub>4</sub> and N<sub>2</sub>) in ZIF-8 have been documented both experimentally and theoretically.<sup>5-9</sup>

Among these studies, it is suggested that the framework stability and flexibility play an important role in the mechanism and performance of gas adsorptions. Application of high external pressure (*e.g.*, in the gigapascal range) on the framework far beyond the practical gas adsorption pressure (*e.g.*, up to 100 bar) may significantly alter the framework topology and thus the adsorption properties.<sup>10-14</sup> For instance, Chapman *et al.*<sup>10</sup> showed that compression of ZIF-8 to 0.34 GPa either in non-penetrating fluid or without pressure

---

\* The content of this chapter is based on the publication: Hu, Y.; Liu, Z.; Xu, J.; Huang, Y. and Song, Y. *Journal of the American Chemical Society* **2013**, *135*, 9287.

transmitting medium (PTM) resulted in an irreversible structural transition and amorphization. Using in-situ high-pressure single crystal X-ray diffraction, however, Moggach *et al.*<sup>11</sup> observed a reversible crystalline-to-crystalline phase transition at around 1.5 GPa in some penetrating PTM. Thus the interaction between the PTM and ZIF-8 framework was believed to play an important role in the phase transition and have a significant influence on the framework stability. While X-ray diffraction was extensively used in these studies to provide the information about structural evolution of crystal lattice with pressure, vibrational spectroscopy allows the understanding of local structures, chemical bonding and, thus the nature of host-guest interaction between the adsorbed molecules and the framework. Given the facts that kinetic diameter of CO<sub>2</sub> (3.3 Å) is slightly smaller than the size of the hexagonal channels of ZIF-8 (3.4 Å) and that the ZIF-8 framework has relatively high stability, it should be possible to insert more CO<sub>2</sub> into the framework at pressures of gigapascal range to substantially enhance the storage capacity. So far no study has addressed the CO<sub>2</sub> storage capacity and CO<sub>2</sub>-ZIF-8 interaction at the above mentioned pressure range, despite extensive adsorption studies and simulations at lower pressures. Here, using *in-situ* FTIR spectroscopy, we investigate the CO<sub>2</sub> adsorptive performance of ZIF-8 and provide the first evidence of the enhanced CO<sub>2</sub>-framework interactions at high external pressures.

## 3.2 Experimental section

The ZIF-8 sample was synthesized according to the literature.<sup>15</sup> A diamond anvil cell (DAC) equipped with type II diamonds with culet sizes of 600 μm was used to generate high pressures. The pure desolvated ZIF-8 powder samples were loaded into the DAC

together with solid CO<sub>2</sub> in a cryogenic bath of liquid nitrogen at a temperature below the melting point of dry ice (i.e., < -78 °C) by introducing the pure gaseous CO<sub>2</sub>. Then the cell was carefully sealed with minimal possible pressure (e.g., 0.4 GPa) at low temperature before warming up to room temperature. A customized IR micro-spectroscopic system with details described in *Chapter 1* was used for all mid-IR absorption measurements.<sup>16</sup> Far-Infrared measurements were performed at the U2A beamline at the National Synchrotron Light Source (NSLS), Brookhaven National Laboratory (BNL).

### 3.3 Results

#### 3.3.1 IR spectrum of ZIF-8 loaded with CO<sub>2</sub> at 0.78 GPa

Figure 3-1b shows the optical image of the loaded sample where transparent areas are mainly solid CO<sub>2</sub> outside the ZIF-8 framework. From top to bottom, representative IR absorption spectra of pure CO<sub>2</sub>, ZIF-8 loaded with CO<sub>2</sub> and pure ZIF-8 collected at a similar pressure (~0.8-1 GPa) are shown in Figure 3-1a. The IR spectrum of pure ZIF-8 is consistent with that previously reported in the literature.<sup>13</sup> The two strong absorption bands at 671 and 2325 cm<sup>-1</sup> in the pure CO<sub>2</sub> spectrum are attributed to the bending mode ( $\nu_2$ ) and asymmetric stretching mode ( $\nu_3$ ), respectively. In addition, two high-frequency bands were observed at around 3600 and 3700 cm<sup>-1</sup>, which are well understood as the CO<sub>2</sub> combination modes of  $\nu_3 + 2\nu_2$  and  $\nu_3 + \nu_1$ , respectively, due to the strong Fermi resonance effect.<sup>17-20</sup>

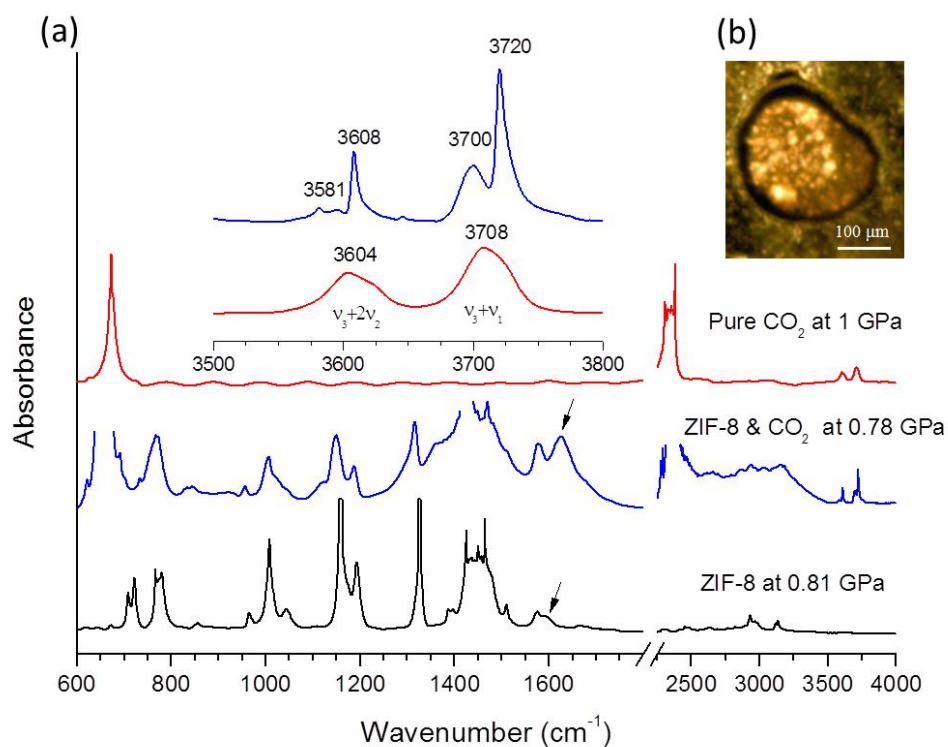


**Figure 3-1.** (a) IR spectrum of ZIF-8 loaded with CO<sub>2</sub> (middle) compared with that of pure CO<sub>2</sub> (top) and that of pure ZIF-8 (bottom) at similar pressures. The inset shows the zoomed spectral region for the combination modes of ZIF-8 loaded with CO<sub>2</sub> (top) and pure CO<sub>2</sub> (bottom). (b) Photograph of ZIF-8 loaded with CO<sub>2</sub> taken under an optical microscope. The arrows indicate the positions of the C=C stretching mode of the imidazole ring.

The IR spectrum of ZIF-8 loaded with CO<sub>2</sub> not only indicates the successful CO<sub>2</sub> loading, but also provides strong evidences for guest-host interactions between ZIF-8 framework and CO<sub>2</sub>. First, the IR spectrum exhibits a composite characteristic profile that comprises the contributions from individual pure CO<sub>2</sub> and pure ZIF-8 framework with some modifications (discussed later). Due to the extremely intense IR absorptions of  $\nu_2$  and  $\nu_3$  modes of CO<sub>2</sub>, their behavior is difficult to monitor directly. A previous work



demonstrated that the CO<sub>2</sub> overtone/combination bands can be used to follow the insertion of CO<sub>2</sub> into the pores of zeolites.<sup>21</sup> In the present case, the most striking observation is the drastically different absorption profile of the overtone/combination bands as shown in Figure 3-1 inset. Each of these two bands splits into a doublet: the  $\nu_3 + \nu_1$  band originally at 3708 cm<sup>-1</sup> displays a doublet at 3700 and 3720 cm<sup>-1</sup>, while the  $\nu_3 + 2\nu_2$  band also splits into two peaks. For each doublet, the low-frequency component resembles the original profile of pure CO<sub>2</sub>, while the high-frequency component is much sharper and intense. The strongly contrasting intensity and linewidth for the two components for each doublet indicate that there are two different types of CO<sub>2</sub> molecules, i.e. the CO<sub>2</sub> outside the ZIF-8 framework and the CO<sub>2</sub> included in the pores of the framework. In order to determine the exact assignments of the doublet, we must understand the pressure behavior of pure CO<sub>2</sub> first.

Figure 3-2a shows the evolution of the pure CO<sub>2</sub> combination modes as a function of pressure from 0.33 to 2.23 GPa. It can be seen clearly that upon compression to 0.61 GPa, both of the combination modes of CO<sub>2</sub> became much sharper, accompanied with an increase of intensity. Previous studies revealed that CO<sub>2</sub> solidifies at the pressure of 0.6 GPa under room temperature.<sup>18</sup> Consequently, the sudden changes of the CO<sub>2</sub> combination modes on compression is due to the phase change of CO<sub>2</sub> from liquid to solid. The sharper and narrower band shape is due to the fact that the solid CO<sub>2</sub> is in a highly crystalline phase (phase I, *Pa3*),<sup>18</sup> which provides homogenous chemical surroundings for the CO<sub>2</sub> molecules, in contrast of the fluid CO<sub>2</sub>. In this case, CO<sub>2</sub> was loaded with the sample initially at 0.47 GPa and room temperature, under which the CO<sub>2</sub> was in liquid state. Thus the ZIF-8 framework was immersed in a liquid bath of CO<sub>2</sub>, which can diffuse into the

pores of the framework. Further compression resulted in the solidification of CO<sub>2</sub> outside the framework, whereas the CO<sub>2</sub> trapped inside the framework remained fluid. As a result, the low-frequency component with similar profile to the overtones of pure liquid CO<sub>2</sub> can be interpreted as a substantial portion of CO<sub>2</sub> molecules being inserted into the ZIF-8 framework under the current pressure-temperature conditions. The higher-frequency component can be assigned as the solid crystalline CO<sub>2</sub> outside the framework. This assignment can be further evidenced by the frequency plots of the  $\nu_3 + \nu_1$  modes as a function of pressure, compared with those of pure CO<sub>2</sub> from experiment and solid CO<sub>2</sub> from calculation,<sup>18</sup> as shown in Figure 3-2b. Clearly, the component with higher frequency (red square) behaves more like solid CO<sub>2</sub> on compression. In addition, in a previous IR study of CO<sub>2</sub> trapped in solid N<sub>2</sub> matrix, a similar splitting behavior for the  $\nu_3 + \nu_1$  combination mode was reported by McCluskey and Zhuravlev.<sup>22</sup> These observations provide strong evidence that CO<sub>2</sub> are trapped and constrained in the SOD cages of ZIF-8 at high pressures.

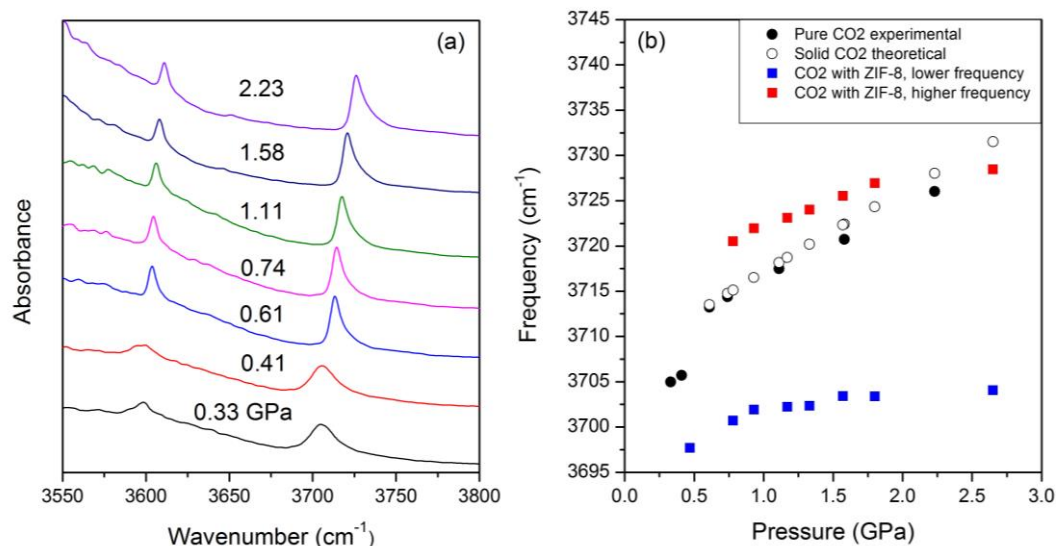


**Figure 3-2.** (a) IR spectra of pure CO<sub>2</sub> in the spectral region of the combination modes collected on compression. (b) Frequency plots of  $\nu_3 + \nu_1$  mode of CO<sub>2</sub> as a function of pressure.

### 3.3.2 IR spectra of ZIF-8 loaded with CO<sub>2</sub> upon compression and decompression

The pressure effects on the CO<sub>2</sub> storage in ZIF-8 were further investigated. Figure 3-3 shows the IR absorption spectra of the combination modes of CO<sub>2</sub> loaded with ZIF-8 upon compression and decompression. When initially loaded at 0.47 GPa, the IR spectrum shows a regular profile of pure CO<sub>2</sub>. When compressed to above 0.78 GPa, a splitting of the combination modes was observed as the CO<sub>2</sub> outside the framework became solid, whereas the CO<sub>2</sub> trapped inside the framework remained fluid. Continuously compressing to higher pressures (e.g., 2.65 GPa or higher) resulted in the blue shift of all modes (Figures 3-3a). However, the splitting of the combination modes can be observed in the entire

pressure range from 0.78 to 2.65 GPa, indicating that the ZIF-8 framework still remained the porosity for CO<sub>2</sub> storage at high pressures that are in the order of GPa. Upon releasing the pressure, the doublet starts to merge into a singlet at 0.47 GPa (Figure 3-3b), indicating that the CO<sub>2</sub> outside the framework became liquid. When the pressure is completely released, the CO<sub>2</sub> molecules inside the framework have escaped from the cages completely, leaving only the signals due to the CO<sub>2</sub> outside the framework in the spectrum (see the bottom spectrum in Figure 3-3b). Furthermore, based on the absorption intensity of the two components of the  $\nu_3 + \nu_1$  mode, we estimated that up to ~33.5 % of the loaded CO<sub>2</sub> was inserted in the framework. These results indicate an interesting, pressure-enhanced CO<sub>2</sub> storage behavior in the ZIF-8 framework.

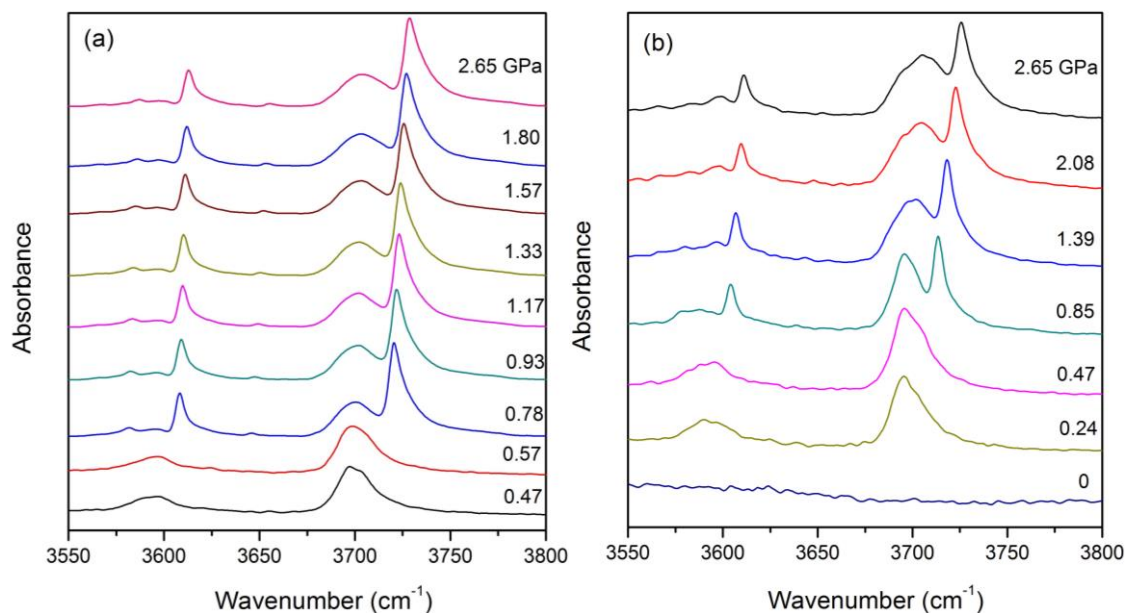


**Figure 3-3.** IR spectra of ZIF-8 loaded with CO<sub>2</sub> in the spectral region of the combination modes collected on compression (a) and decompression (b) at room temperature.

### 3.4 Discussion

The nature of the interaction between CO<sub>2</sub> and ZIF-8 framework as well as the migration mechanism is of great interest, which may be understood from previous studies. For instance, Lee *et al.*<sup>23</sup> observed a similar reversible insertion behavior of CO<sub>2</sub> into a small-pore zeolite natrolite under a pressure of 1.5 GPa, which results in the expansion of unit cell volume of the host framework. However, the insertion must be triggered at elevated temperatures, in contrast to the room-temperature behavior of ZIF-8 observed here. The work by Haines *et al.*<sup>24</sup> and Coasne *et al.*<sup>25</sup> showed that at room temperature, CO<sub>2</sub> can be incorporated into the framework of completely siliceous zeolite ZSM-5 (silicalite-1) with a pore size slightly larger than that of natrolite and that the presence of CO<sub>2</sub> in the pore stabilizes the zeolitic framework.<sup>24</sup> The pore size of ZIF-8 is in between natrolite and silicalite-1. Other contributing factors that must be considered to fully understand the insertion mechanism of CO<sub>2</sub> into the framework at high pressures include: (1) The pressure for the CO<sub>2</sub> insertion with respect to the ZIF-8 framework is significantly lower (lower than the gigapascal level at room temperature) compared to that for natrolite (1.5 GPa at high temperature), suggesting that CO<sub>2</sub> must be in fluid state for effective diffusion under stressed conditions.<sup>23</sup> (2) The unique pressure characteristics of ZIF-8 in terms of framework flexibility and pressure-induced enlargement of pore opening and volume plays an important role in the facilitation of CO<sub>2</sub> insertion at high pressures. At high pressures, Moggach *et al.*<sup>11</sup> observed a new phase with the same space group symmetry as the ambient ZIF-8, but with a twisted conformation of the imidazolate linkers, resulting in total opening of the 6-member ring window. Thus methanol molecules as the PTM can be reversibly inserted into the pores even at 1.5 GPa, leading to the expansion of

the unit cell volume as well. Using molecular dynamics simulations, Pantatosaki *et al.*<sup>9</sup> investigated the mobility of the imidazolate ligands of ZIF-8 framework together with diffusivity of CO<sub>2</sub> in comparison with experimental data. Their results further confirmed that the flexibility of the imidazolate linkers plays a critical role in the guest transportation dynamics. More recently, the framework flexibility of ZIF-8 was found to facilitate the N<sub>2</sub> adsorption<sup>7</sup> by adopting the high pressure structure via the swing effect of the imidazolate linker<sup>7,8</sup> even though the loading pressure is substantially lower than the gigapascal level. Based on these studies, our IR spectroscopic data consistently suggest that pore opening, framework flexibility and diffusivity of CO<sub>2</sub> all play an important role in the migration of CO<sub>2</sub> with respect to the ZIF-8 framework.

The interaction between CO<sub>2</sub> and the framework is further evidenced by the different IR features of ZIF-8 loaded with CO<sub>2</sub> compared to that of empty framework (Figure 3-1a). The most prominent difference, for example, is the appearance of an intense absorption band at around 1620 cm<sup>-1</sup> in the spectrum of the ZIF-8 loaded with CO<sub>2</sub>, which can be assigned to the C=C stretching mode of the imidazole ring. The enhancement of this mode, which is otherwise lacking in the pure ZIF-8, strongly suggests the interaction between CO<sub>2</sub> and the framework on the specific site of the imidazole ring. The adsorption site of gaseous CO<sub>2</sub> in the ZIF framework has been extensively investigated both by experiments and simulations. Most studies established that preferential adsorption sites are located in specific regions close to the organic imidazolate linkers rather than the zinc atoms.<sup>6,9,26</sup> Thus our spectroscopic observations are consistent with previous interpretations that the major interaction sites of ZIF-8 framework for CO<sub>2</sub> are the organic linkers. *In situ* X-ray diffraction measurements at high pressure on the ZIF-8 and CO<sub>2</sub>

system would be helpful to elucidate the exact interaction mechanism between CO<sub>2</sub> and the framework.

Being guest molecules, CO<sub>2</sub> can, in turn, influence the stability of ZIF-8 under high pressure substantially. Using synchrotron far-IR spectroscopy, the structural stability of the empty ZIF-8 framework was examined in the lattice region (Figure 3-4). Pressure-induced distortion of [ZnN<sub>4</sub>] tetrahedral as well as irreversible amorphization was observed as evidenced by the splitting and broadening of the Zn-N stretching and bending modes and the depletion of the lattice modes. In addition, our previous mid-IR measurements on empty ZIF-8 framework showed that the C=N stretching mode at 1584 cm<sup>-1</sup> was very sensitive to compression, first by exhibiting a significant red shift in the pressure region below 1.6 GPa,<sup>13</sup> and subsequently being weakened at higher pressures, indicating the distortion of imidazolate ring. When ZIF-8 and CO<sub>2</sub> mixture was compressed to higher pressures (e.g., 2.65 GPa, Figure 3-5), however, no obvious change in the IR bands of the framework was observed (see Figure 3-6 and Table 3-1), in strong contrast to the pressure behavior of the pure empty ZIF-8 framework. Furthermore, the near zero pressure dependence of the C=N mode (Table 3-1) was observed for the ZIF-8 loaded with CO<sub>2</sub>, and its constant IR intensity (Figure 3-5) indicates that when CO<sub>2</sub> is inserted into the framework, the imidazolate rings are much less distorted and thus the rigidity of the entire framework is substantially enhanced. Overall, the chemical and mechanical robustness of the framework formed by the relatively stiffer metal centered tetrahedrons as joints but with flexible linkers makes ZIF-8 an interesting and promising agent for the storage of CO<sub>2</sub> (and perhaps other gases) at high pressures conditions.

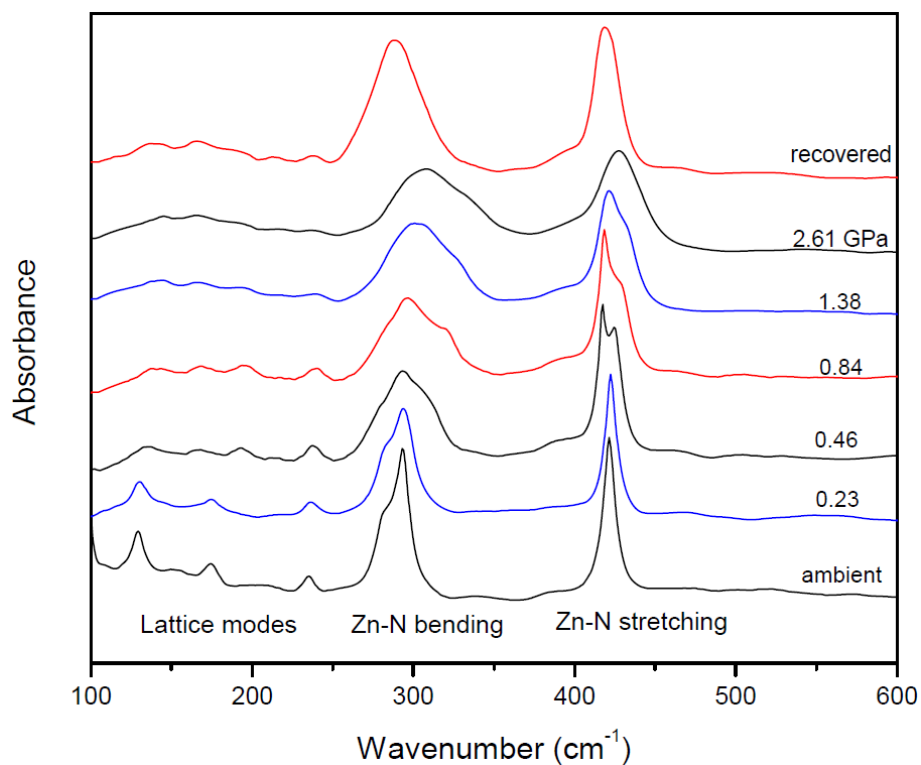


**Figure 3-4.** Far-IR spectra of ZIF-8 upon compression to 2.61 GPa and decompression to ambient pressure. The bands at 420 and 290 cm<sup>-1</sup> can be attributed as Zn-N stretching and bending modes, respectively; the lower frequency modes are assigned as framework lattice vibrations.



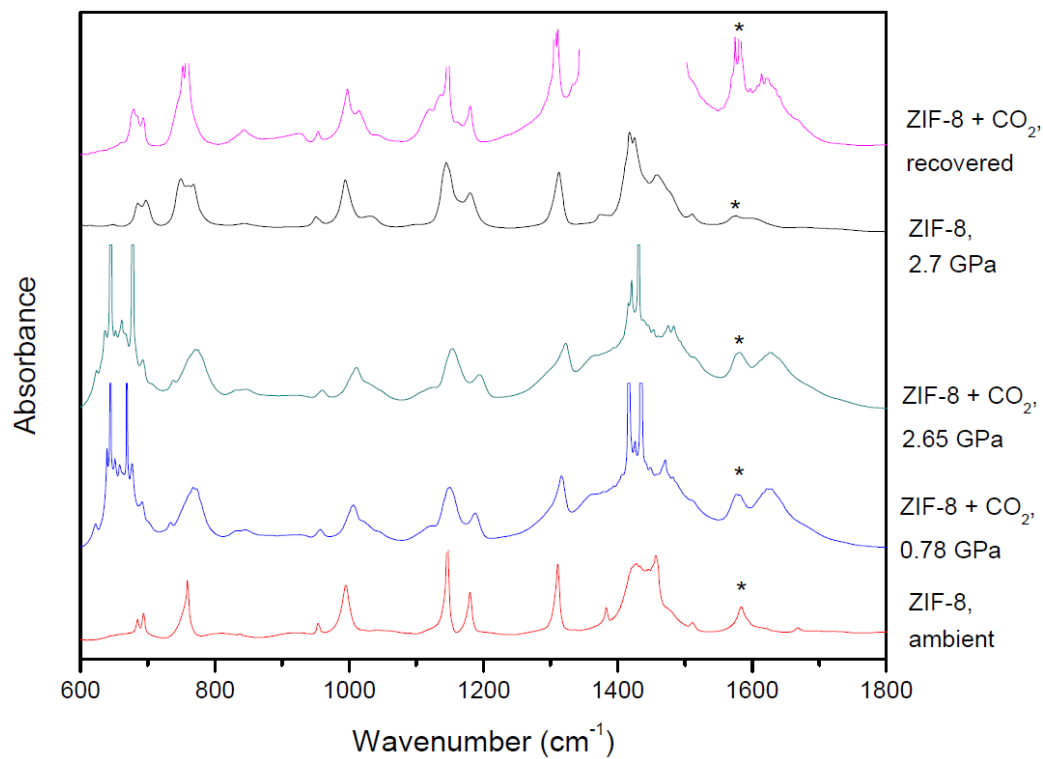


**Figure 3-5.** IR spectra of ZIF-8 loaded with CO<sub>2</sub> upon compression and decompression in comparison with those of pure ZIF-8 at similar pressures. The band labeled with an asterisk indicates the position of the C=N stretching mode of the ZIF-8 framework (see text).

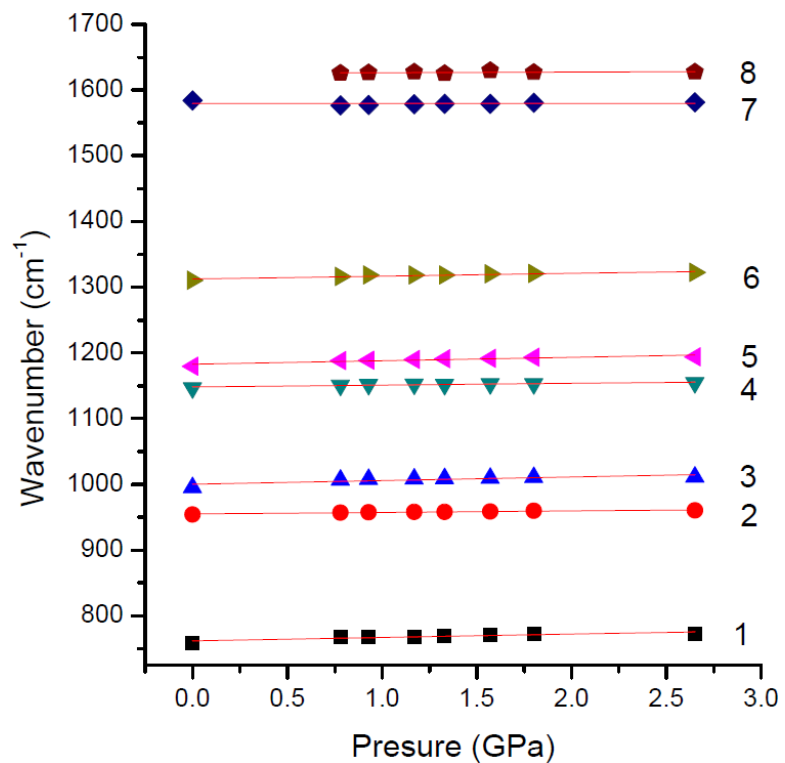


**Figure 3-6.** IR frequencies of selected modes of the ZIF-8 framework loaded with CO<sub>2</sub> as a function of pressure.

**Table 3-1.** Pressure dependence ( $dv/dP$ ,  $\text{cm}^{-1}/\text{GPa}$ ) of IR modes of  $\text{CO}_2$  loaded ZIF-8 from 0 to 2.65 GPa

Mode	Frequency ( $\text{cm}^{-1}$ )	Pressure dependence ( $\text{cm}^{-1}/\text{GPa}$ )
1	759.0	5.2
2	953.9	2.3
3	995	5.5
4	1146.4	2.8
5	1179.8	5.2
6	1310.4	4.3
7	1584	-0.1
8	1625.5	1.0

### 3.5 Conclusions

In summary, we demonstrated a pressure-enhanced CO<sub>2</sub> storage in ZIF-8 using *in situ* FTIR spectroscopy. Two types of CO<sub>2</sub> molecules (inside the framework and outside as bulk medium) can be differentiated by the combination IR bands of CO<sub>2</sub> unambiguously due to the CO<sub>2</sub> adsorption in the framework. Strong interactions between CO<sub>2</sub> and framework are apparent from the IR features of the framework in the C=C stretching region, providing consistent information about the possible interaction site. As guest molecules, CO<sub>2</sub> can substantially influence the structural stability of the ZIF-8 framework. The enhanced CO<sub>2</sub> storage capacity of ZIF-8 at high pressure provides new insight into the gas capture and storage applications of ZIFs.

### 3.6 References

- (1) Park, K. S.; Ni, Z.; Cote, A. P.; Choi, J. Y.; Huang, R. D.; Uribe-Romo, F. J.; Chae, H. K.; O'Keeffe, M.; Yaghi, O. M. *Proceedings of the National Academy of Sciences of the United States of America* **2006**, *103*, 10186.
- (2) Wang, B.; Cote, A. P.; Furukawa, H.; O'Keeffe, M.; Yaghi, O. M. *Nature* **2008**, *453*, 207.
- (3) Phan, A.; Doonan, C. J.; Uribe-Romo, F. J.; Knobler, C. B.; O'Keeffe, M.; Yaghi, O. M. *Accounts of Chemical Research* **2010**, *43*, 58.
- (4) Sumida, K.; Rogow, D. L.; Mason, J. A.; McDonald, T. M.; Bloch, E. D.; Herm, Z. R.; Bae, T. H.; Long, J. R. *Chemical Reviews*. **2012**, *112*, 724.
- (5) Nune, S. K.; Thallapally, P. K.; Dohnalkova, A.; Wang, C. M.; Liu, J.; Exarhos, G. J. *Chemical Communications*. **2010**, *46*, 4878.
- (6) Perez-Pellitero, J.; Amrouche, H.; Siperstein, F. R.; Pirngruber, G.; Nieto-Draghi, C.; Chaplais, G.; Simon-Masseron, A.; Bazer-Bachi, D.; Peralta, D.; Bats, N. *Chemistry-A European Journal* **2010**, *16*, 1560.
- (7) Fairen-Jimenez, D.; Moggach, S. A.; Wharmby, M. T.; Wright, P. A.; Parsons, S.; Duren, T. *Journal of American Chemical Society* **2011**, *133*, 8900.

- (8) Fairen-Jimenez, D.; Galvelis, R.; Torrisci, A.; Gellan, A. D.; Wharmby, M. T.; Wright, P. A.; Mellot-Draznieks, C.; Duren, T. *Dalton Transactions* **2012**, 41, 10752.
- (9) Pantatosaki, E.; Megariotis, G.; Pusch, A. K.; Chmelik, C.; Stallmach, F.; Papadopoulos, G. K. *Journal of Physical Chemistry C* **2012**, 116, 201.
- (10) Chapman, K. W.; Halder, G. J.; Chupas, P. J. *Journal of American Chemical Society* **2009**, 131, 17546.
- (11) Moggach, S. A.; Bennett, T. D.; Cheetham, A. K. *Angewandte Chemie International Edition* **2009**, 48, 7087.
- (12) Bennett, T. D.; Tan, J. C.; Moggach, S. A.; Galvelis, R.; Mellot-Draznieks, C.; Reisner, B. A.; Thirumurugan, A.; Allan, D. R.; Cheetham, A. K. *Chemistry-A European Journal* **2010**, 16, 10684.
- (13) Hu, Y.; Kazemian, H.; Rohani, S.; Huang, Y. N.; Song, Y. *Chemical Communications* **2011**, 47, 12694.
- (14) Fu, Y. Q.; Song, Y.; Huang, Y. I. *Journal of Physical Chemistry C* **2012**, 116, 2080.
- (15) Shi, Q.; Chen, Z.; Song, Z.; Li, J.; Dong, J. *Angewandte Chemie International Edition* **2011**, 50, 672.
- (16) Dong, Z.; Song, Y. *Journal of Physical Chemistry C* **2010**, 114, 1782.
- (17) Hanson, R. C.; Jones, L. H. *Journal of Chemical Physics* **1981**, 75, 1102.
- (18) Aoki, K.; Yamawaki, H.; Sakashita, M. *Physical Review B* **1993**, 48, 9231.
- (19) Giordano, V. M.; Gorelli, F. A.; Bini, R. *Low Temperature Physics* **2006**, 32, 1067.
- (20) Martin, P. E.; Barker, E. F. *Physical Review* **1932**, 41, 291.
- (21) Santoro, M.; Gorelli, F.; Haines, J.; Cambon, O.; Levelut, C.; Garbarino, G. *Proceedings of the National Academy of Sciences of the United States of America* **2011**, 108, 7689.
- (22) McCluskey, M. D.; Zhuravlev, K. K. *Journal of Chemical Physics* **2002**, 116, 1607.
- (23) Lee, Y.; Liu, D.; Seoung, D.; Liu, Z. X.; Kao, C. C.; Vogt, T. *J. Am. Chem. Soc.* **2011**, 133, 1674.
- (24) Haines, J.; Cambon, O.; Levelut, C.; Santoro, M.; Gorelli, F.; Garbarino, G. *Journal of American Chemical Society* **2010**, 132, 8860.
- (25) Coasne, B.; Haines, J.; Levelut, C.; Cambon, O.; Santoro, M.; Gorelli, F.; Garbarino, G. *Physical Chemistry Chemical Physics* **2011**, 13, 20096.
- (26) Garberoglio, G.; Taioli, S. *Microporous and Mesoporous Materials* **2012**, 163, 215.

## Chapter 4

### 4 The Structural Stability of and Enhanced CO<sub>2</sub> Storage in MOF MIL-68(In) under High Pressures Probed by FTIR Spectroscopy

#### 4.1 Introduction

Metal-organic frameworks (MOFs) are crystalline porous materials that consist of metal ions / clusters bridged by organic linking groups to form one-, two-, or three-dimensional coordination networks. Over the past decade, more than 20,000 MOFs with diverse structures and functionalities have been reported and studied,<sup>1,2</sup> owing to their potential applications in a variety of areas, including gas storage,<sup>3-6</sup> molecular separations,<sup>7-9</sup> heterogeneous catalysis,<sup>10-13</sup> and drug delivery.<sup>14-17</sup> In the large MOF family, one series of MOF material denoted MIL-68 has attracted much recent attention because of its distinctive structure which contains two types of channels with different opening sizes. The first MIL-68 material (with metal ion V) was synthesized by Ferey and coworkers<sup>18</sup> in 2004 and several other analogs with different metal-ions (Ga,<sup>19</sup> In,<sup>19</sup> Fe<sup>20</sup> and Al<sup>21</sup>) were further reported later. All these isostructures of MIL-68, which crystallizes in *Cmcm* space group, are built up from the connection of corner-sharing metal-centered octahedral units, MO<sub>4</sub>(OH)<sub>2</sub> with the terephthalate ligands, in which the metal center is six coordinated with four oxygens from carboxylate groups and two hydroxyl oxygens. The adjacent octahedral units are linked together via two hydroxyl groups located in trans positions and connected through carboxylate functions (Figure 4-1a). If the octahedra are considered as nodes, their connections with the terephthalate groups give rise to the formation of the so-called Kagome´net, composed of hexagonal rings delimited by six triangular rings, with an opening diameter of 6.0-6.4 and 16-17 Å respectively (Figure 4-1b).<sup>19</sup> Such a structural

topology containing two distinct pore sizes makes MIL-68 a promising candidate for applications such as gas storage and separation.<sup>21,22</sup>

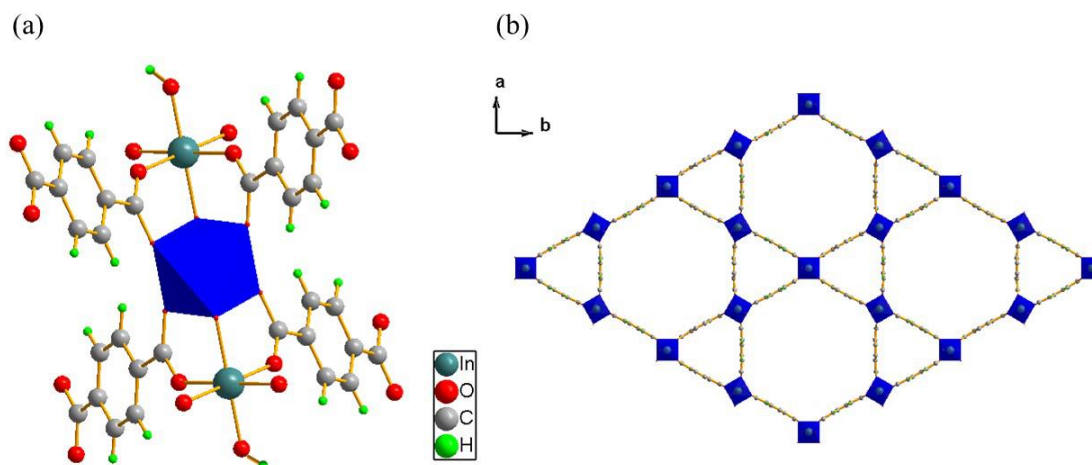


**Figure 4-1.** (a) Local structure and Indium coordination environment of MIL-68 (In). (b) View of the structure of activated MIL-68 (In) along  $c$  axis, showing the arrangement of hexagonal and triangular channels. The DMF molecules in the channels of as-made framework can be mostly removed upon activation.

The structural stability of MOFs is crucial to their applications. In previous studies of MIL-68, sorption measurements were performed at pressures up to 50 bar,<sup>21</sup> however the effect of higher external pressures (e.g., in the gigapascal range) on the framework has not been examined so far. In fact, only a handful of MOFs have been studied under high pressures previously. Much of the early work has mainly focused on (1) the mechanical properties in response to pressure;<sup>23-31</sup> (2) the pressure-induced phase transitions / amorphizations upon compression and their reversibilities upon decompression<sup>32-38</sup> and (3) the pressure-enhanced interactions between host frameworks and guest molecules.<sup>39-44</sup>

Take a few examples from the latter two directions, since the interest of our study lays in the enhanced sorption properties of MOFs under high pressure. Moggach *et al.*<sup>33</sup> observed a reversible crystalline-to-crystalline phase transition of ZIF-8 in pressure transmitting medium (PTM) at around 1.5 GPa, which increased the volume of the unit cell. Lapidus *et al.*<sup>36</sup> demonstrated that external pressure (0.9-1.8 GPa) can be exploited to provide a novel and unexpected means to transform a dense interpenetrated framework system  $\text{Zn}(\text{CN})_2$  into a new porous material, in the presence of small molecule pressure-transmitting fluids. Our prior work<sup>42</sup> suggested that pressure can play a regulating role in the insertion and extrusion of  $\text{CO}_2$  with respect to the ZIF-8 framework, even at room temperature. These work and high pressure studies on other nano-porous materials (e.g. zeolites)<sup>45-47</sup> demonstrate that pressure can provide a new approach to achieve structural modifications for the framework including changes in pore size, opening and geometry, channel shape and internal surface area. Subsequently, application of external pressure on the frameworks far beyond the practical gas adsorption pressure may significantly enhance their adsorption properties. Therefore, exploring the high-pressure behavior of MIL-68 is important for its gas storage and separation applications. Herein, we report the first *in situ* high-pressure investigation of MIL-68(In) and its performance for  $\text{CO}_2$  storage by FTIR spectroscopy. Particular attention is focused on (1) the differences in stability and reversibility of the structural modifications between MIL-68(In) with and without solvent molecules; (2) the role of encapsulated guest molecules (PTM) in the stability and transformation of the framework under high pressure; (3) the pressure dependence of  $\text{CO}_2$  storage in the framework and the host-guest interaction between the framework and  $\text{CO}_2$



and (4) understanding the structural origin of the MOF framework promoting CO<sub>2</sub> storage under high pressures with the aid of Monte Carlo simulations.

## 4.2 Experimental section

The as-made MIL-68(In) sample was prepared by hydrothermal synthesis from a mixture of indium nitrate (1.05 mmol, 408.2 mg), terephthalic acid (1.2 mmol, 200 mg) and dimethylformamide (DMF, 70 mmol, 5 mL).<sup>19</sup> Specifically, the reactants were placed in a Teflon-lined autoclave and heated for 48 h at 100 °C in an oven. The resulting white powder was filtered off and washed with DMF and consisted of elongated needlelike crystallites of 20-200 µm size. The yield was 83% based on indium. The activated MIL-68(In) was obtained by heating the as-made sample in a vacuum gas manifold at 250 °C for 6 hours to remove the solvent molecules encapsulated inside the framework. The crystallinity of the samples were checked by powder X-ray diffraction (XRD).

A diamond anvil cell (DAC) equipped with type II diamonds with culet sizes of 600 µm was used to generate high pressures. A hole with a diameter of 200 µm was drilled in the center of “pre-indented” stainless steel gaskets and used as a sample chamber. Ruby chips (Al<sub>2</sub>O<sub>3</sub> doped with Cr<sup>3+</sup>) were added in the sample chamber as the pressure calibrant, and the pressure was determined from the well-established ruby R<sub>1</sub> fluorescence line shift. Spectral grade KBr was added in the sample chamber when necessary to resolve strong IR peaks. The samples with 30 µm in thickness were loaded into the DAC. In order to focus on the intrinsic pressure behavior of MIL-68 (In), both the as-made and activated sample were loaded without PTM. In the entire pressure region (0-11 GPa), no significant

nonhydrostatic effect was observed from the ruby fluorescence profile. In addition, the activated sample was loaded with nujol as PTM to study the possible interactions between the sample and the PTM that may enter the channels of the framework during compression. In order to study the performance for CO<sub>2</sub> storage, the activated MIL-68(In) powder samples were loaded into the DAC together with solid CO<sub>2</sub> in a cryogenic bath of liquid nitrogen at a temperature below the melting point of dry ice (i.e., < -78 °C) by introducing pure gaseous CO<sub>2</sub>. Then the cell was carefully sealed with minimal possible pressure (~0.5 GPa) at low temperature before warming up to room temperature. Upon loading the sample, in situ IR spectra were obtained using a customized IR micro-spectroscopy system with details described in *Chapter 1*.<sup>48</sup> Multiple runs were carried out for reproducibility and all measurements were performed under room temperature. During both compression and decompression and in between runs, sufficiently long time was allowed for equilibrium to rule out any kinetic effect and no time dependent behavior was observed.

The framework structures and CO<sub>2</sub> storage properties were studied using first principle and molecular mechanics simulations. Firstly, the geometry optimizations of MIL-68(In) framework are performed by Dmol3<sup>49,50</sup> at the DFT-PBE level with a double numerical basis set plus dynamic polarization functions (DNP).<sup>51</sup> The convergence threshold values are specified as  $1 \times 10^{-5}$  Ha for energies,  $2 \times 10^{-3}$  Ha/ Å for gradients, and  $5 \times 10^{-3}$  Å for displacements, respectively. The self-consistent field (SCF) convergence tolerance is set to  $1 \times 10^{-6}$  Ha. The gas adsorption properties were simulated using the Grand Canonical Monte Carlo (GCMC) method<sup>52</sup>, which was implemented in the sorption module in Materials Studios 7.0. During GCMC simulations, the MIL-68(In) framework was assumed to be rigid with constrained atoms. The vdW interactions between the CO<sub>2</sub>

molecule and the MIL-68(In) are described by the Dreiding force field<sup>53</sup> but with the revised Lennard-Jones (LJ) parameters<sup>54</sup> obtained from our first-principle calculations. A series of fixed pressure simulations were carried out at room temperature (298 K) from 1 to  $10^5$  bar. At each pressure, the GCMC simulation consisted of  $1 \times 10^6$  steps to allow equilibration, followed by  $1 \times 10^7$  steps to sample the configuration space.

## 4.3 Results

### 4.3.1 IR spectra of as-made and activated MIL-68(In) at ambient pressure

Figure 4-2 shows the IR spectra of as-made and activated MIL-68(In) at ambient conditions, which are consistent with those reported previously.<sup>19</sup> Most of the absorption bands for the two samples are associated with the vibrations of the organic units (i.e. terephthalate acid). For example, the bands in the spectral region of  $700 - 900 \text{ cm}^{-1}$  are associated with the out-of-plane bending of the benzene ring, while those between  $1000$  and  $1200 \text{ cm}^{-1}$  are assigned as benzene ring in-plane bending. The peaks at around  $1400$  and  $1560 \text{ cm}^{-1}$  are attributed to symmetric and asymmetric stretch modes of the carboxylate groups attached to indium centers. The detailed assignments for the selected IR bands<sup>55</sup> are listed in the supporting information Table 4-1. In addition, both the spectra present a main band ( $\nu_1$ ) at  $\sim 3700 \text{ cm}^{-1}$  characteristic of the bridging structural OH units. A weaker shoulder can be found at slightly lower wavenumber. It is well established that the frequency of  $\nu_{\text{OH}}$  decreases with the pore size, as already reported in the case of zeolites. Jacob *et al.* reported that when OH groups vibrate in the 6- and 8-membered rings, a red shift occurs compared to the frequency at which their vibration would occur in larger

pores.<sup>56</sup> Indeed, in the MIL-68(In) framework, 1/3 of the hydroxyl groups point towards the voids of the triangular channels while 2/3 are orientated towards the hexagonal ones.<sup>19,20</sup> Thus, the band with the higher frequency can be assigned to OH groups in the large pores (hexagonal channels), and that with lower frequency being thus characteristic of the OH groups in the small pores (triangular channels). The frequency difference (19  $\text{cm}^{-1}$ ) of the OH units in the triangular pores between the as-made and activated framework is likely due to a fraction of the hydroxyl groups experiencing a weak perturbation with DMF molecules before activation.<sup>57</sup> Besides these common IR features, some differences in the IR spectrum can be observed upon activation of the sample. Firstly, in contrast to the intense and broad band assigned to water in the region 3000 – 3500  $\text{cm}^{-1}$  of the as-made sample, the spectrum for the activated sample indicates that most of the adsorbed water were removed. Secondly, the sharp decrease of the intensity of the band at 1667  $\text{cm}^{-1}$  ( $\nu_2$ ) corresponding to C=O bonds of DMF inside the as-made framework suggests the elimination of most of the solvent molecules. Furthermore, the disappearance of the band around 780  $\text{cm}^{-1}$  ( $\nu_{12}$ ) which is due to the residual terephthalate acid in the as-made framework indicates that the free acid was detached from the framework. All these observations of the differences in the spectra suggest that the guest molecules including water, solvent and free acid were mostly removed upon activation.

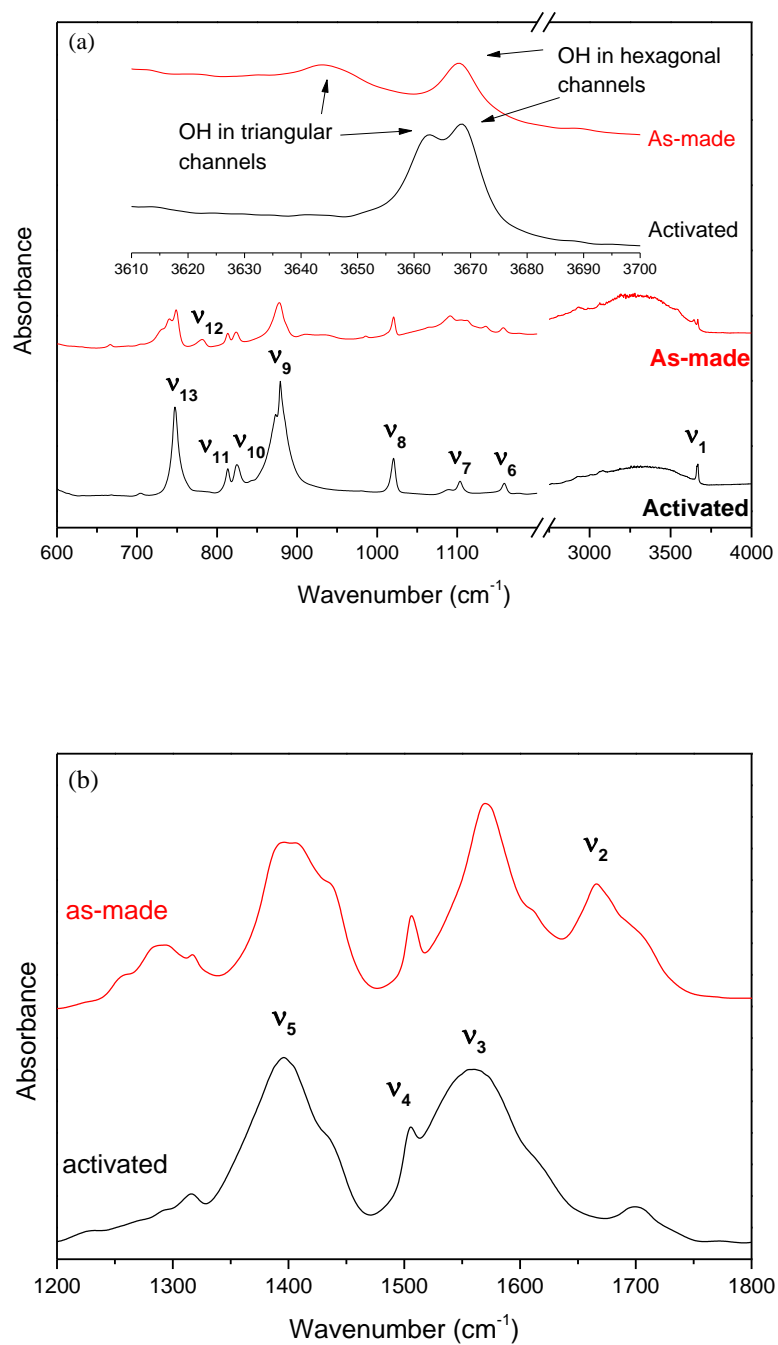


**Figure 4-2.** IR spectra for as-made and activated MIL-68(In) in the frequency region (a) 600-4000  $\text{cm}^{-1}$ , with the inset showing the OH stretching modes in the enlarged spectral region of 3610-3700  $\text{cm}^{-1}$  at the top; (b) 1200-1800  $\text{cm}^{-1}$ .

**Table 4-1.** Assignments for selected IR modes ( $\text{cm}^{-1}$ ) of MIL-68(In) at ambient pressure

Mode	Frequency ( $\text{cm}^{-1}$ )			Assignments
	as-made MIL-68	activated MIL-68	terephthalic acid <sup>55</sup>	
v <sub>1</sub>	3667	3668	3665	OH stretching (in hexagonal channel)
	3643	3662		OH stretching (in triangular channel)
v <sub>2</sub>	1666			C=O stretching (DMF)
v <sub>3</sub>	1570	1559	1576	Asymmetric OCO stretching
v <sub>4</sub>	1506	1505	1509	CCH bending + C=C stretching
v <sub>5</sub>	1400	1395	1424	Symmetric OCO stretching
v <sub>6</sub>	1157	1158	1168	CCH bending + COO bending
v <sub>7</sub>	1091	1103	1136	CCH bending + C=C bending
v <sub>8</sub>	1020	1020	1019	CCC out-of-plane bending + CCH bending
v <sub>9</sub>	877	877		CH out-of-plane bending
v <sub>10</sub>	823	824	832	
v <sub>11</sub>	813	813	819	
v <sub>12</sub>	781		784	OH out-of-plane bending (terephthalate acid)
v <sub>13</sub>	748	747	735	C-COO out-of-plane bending

### 4.3.2 IR spectra of as-made MIL-68(In) upon compression

The *in situ* IR spectra of the as-made MIL-68(In) were acquired as a function of pressure up to 9.7 GPa, followed by complete decompression at room temperature. The selected IR absorption bands of as-made MIL-68(In), shown in Figure 4-3, exhibit significant changes even upon slight compression below 1 GPa. For example, both the intensity of  $\nu_{13}$  and  $\nu_{12}$  modes experience a major enhancement at a low pressure of 0.13 GPa. The  $\nu_{11}$  and  $\nu_{10}$  mode begin to merge whereas the  $\nu_9$  mode begins to split. The initial compression also lead to the appearance of two new IR bands labeled as  $\nu_A$  at  $938\text{ cm}^{-1}$  and  $\nu_B$  at  $986\text{ cm}^{-1}$ , owing to the interaction between DMF and the framework. Moreover, the most remarkable change is the  $\nu_{O-H}$  mode in the hexagonal channels at  $3667\text{ cm}^{-1}$ , which totally disappears during compression. This could be due to the formation of hydrogen bonds between OH units and the solvent molecules DMF in the hexagonal pores. At the pressure of 0.75 GPa, the  $\nu_{11}$  and  $\nu_{10}$  modes merge into one peak and the  $\nu_9$  mode further splits. Besides, the O-H stretch mode in the triangular channels at  $3643\text{ cm}^{-1}$  vanishes as well, indicating the enhanced interaction between the OH units and DMF within the triangular pores. Further compression results in continuous broadening of the IR bands, including the gradual broadening of the O-C-O stretch modes at  $\sim 1400$  and  $1570\text{ cm}^{-1}$  and the C=O stretch mode of DMF. At the highest pressure of 9.73 GPa, even though the IR profile is much broadened compared to ambient spectrum, most of the bands are still characteristic of the organic ligand, suggesting that the framework is still intact under pressure up to 9.73 GPa. In particular, the gentle change of O-C-O modes which are directly linked to the metal center indium indicates the metal-linker bond (In-O) are not broken with increasing pressure.

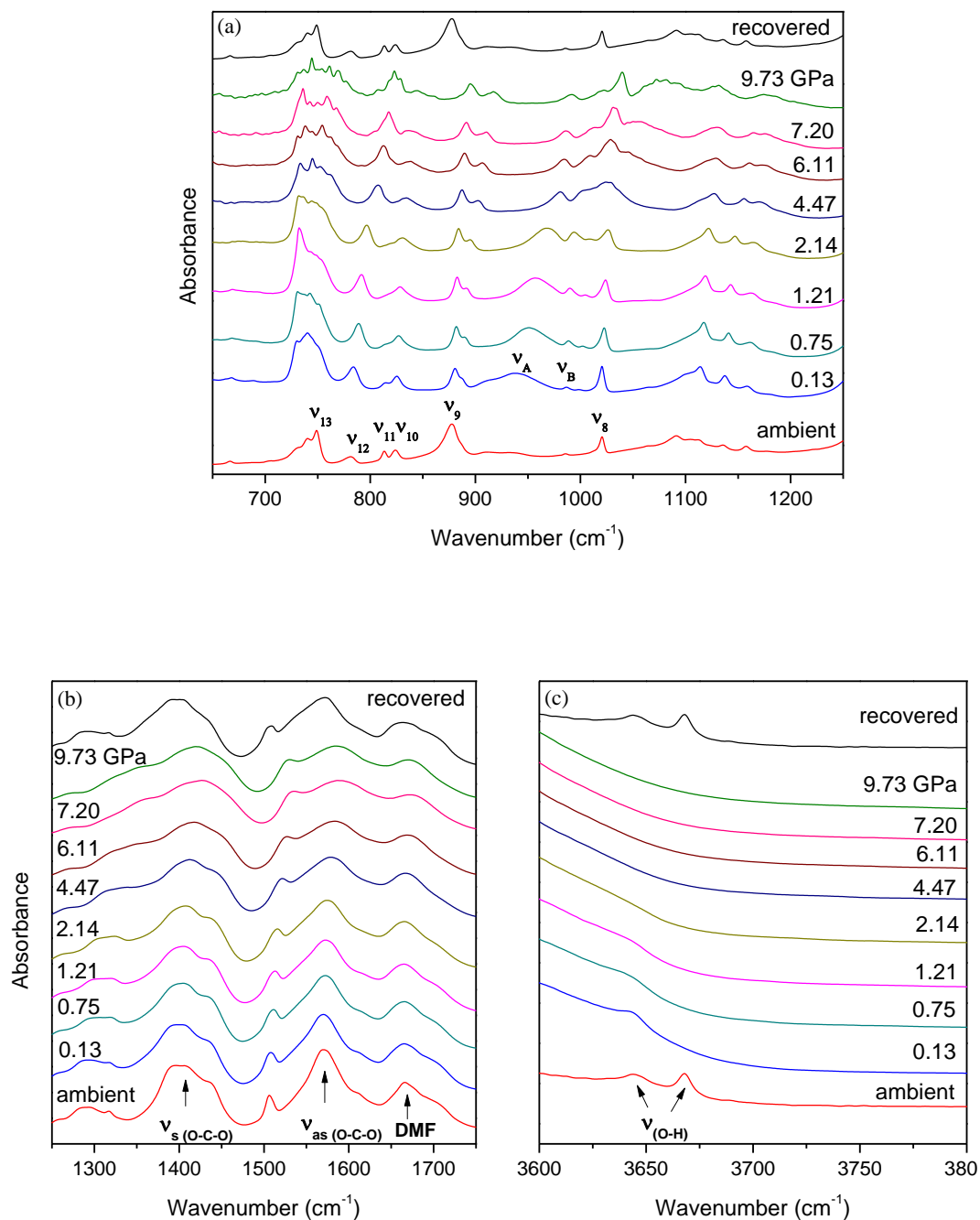


**Figure 4-3.** The IR spectra of as-made MIL-68(In) upon compression in the frequency region (a) 650-1250  $\text{cm}^{-1}$ ; (b) 1250-1750  $\text{cm}^{-1}$ ; (c) 3600-3800  $\text{cm}^{-1}$ .



Then the IR spectra of as-made MIL-68(In) were collected upon decompression all the way back to ambient pressure. Upon complete decompression, the recovered sample exhibits the same spectrum as the original sample. Especially the O-H stretch mode that experiences drastic changes are clearly recovered. The comparison suggests that the structural modifications of as-made MIL-68(In) are completely reversible in the pressure region 0-9 GPa in which the framework structure are highly preserved.

The frequency of selected IR bands of the as-made MIL-68(In) during compression is shown in Figure 4-4, along with the pressure dependencies listed in Table 4-2. In general, most of the IR modes exhibit regular pressure-induced blue shifts, consistent with that the bonds become stiffened upon compression. For example,  $\nu_2 - \nu_{12}$  mode show slight blue shifts (pressure dependence  $< 5 \text{ cm}^{-1} \cdot \text{GPa}^{-1}$ ) with increasing pressure. In strong contrast, the O-H modes merge upon initial compression to 0.13 GPa and completely disappear upon further compression above 1 GPa. The pressure-sensitive behavior of  $\nu_{\text{O-H}}$  is most likely due to the formation of hydrogen bonding between the C=O bond of DMF and O-H group of the framework when external pressure applies and subsequently the O-H modes are highly weakened.<sup>58</sup> Further compression to 9.7 GPa results in slight deformation of the framework because of the gentle changes of the frequencies with increasing pressure.

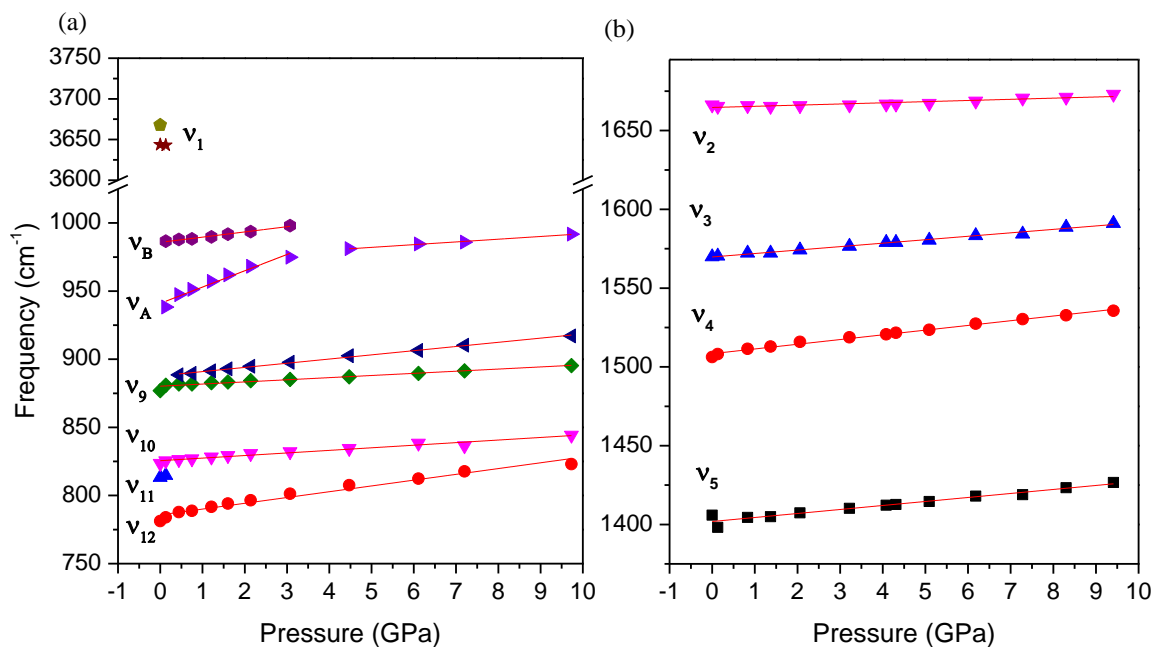


**Figure 4-4.** Frequency of IR modes of as-made MIL-68(In) as a function of pressure from 0 to 9 GPa in the spectral region of (a) 750-3750  $\text{cm}^{-1}$ ; (b) 1375-1695  $\text{cm}^{-1}$ .

**Table 4-2.** Pressure dependence ( $dv/dP$ ,  $\text{cm}^{-1} \text{GPa}^{-1}$ ) of IR modes of as-made MIL-68(In) from 0 to 9 GPa

IR Mode	Frequency ( $\text{cm}^{-1}$ )	$dv/dP$ ( $\text{cm}^{-1} \text{GPa}^{-1}$ )	
v <sub>2</sub>	1666	0.7	
v <sub>3</sub>	1570	2.2	
v <sub>4</sub>	1506	3.0	
v <sub>5</sub>	1400	2.5	
v <sub>B</sub>	986	3.8	
v <sub>A</sub>	938	12.0	2.0
		(0-3 GPa)	(4-9 GPa)
v <sub>9</sub>	888	3.1	
	877	1.6	
v <sub>10</sub>	823	1.9	
v <sub>12</sub>	781	4.2	

### 4.3.3 IR spectra of activated MIL-68(In) upon compression

The study above on as-made MIL-68(In) demonstrates the strong guest-host interactions within the framework in response to compression. We then focused on the intrinsic pressure behavior of activated MIL-68(In), and the selected IR spectra are shown in Figure 4-5. Upon initial compression to 0.12 GPa, the major change of the IR profile is the sudden broadening of  $\nu_{\text{O-H}}$  modes with a drop of intensity, similar to that of as-made framework. As discussed in the scenario of as-made framework, the drastic change of OH mode is associated with the strengthened hydrogen bonding. However, the activated framework contains very few guest species (i.e., DMF) in the pores. Thus the response of OH modes to pressure might be due to the formation of hydrogen bonding between OH units and the adjacent carboxylic group within the unit cell of the framework. Further compression leads to gradual broadening of the peaks, accompanied with band splitting ( $\nu_{13}$  mode). At the highest pressure of 9.3 GPa, the IR profile can be characterized as a largely broadened pattern, indicating the transformation to disordered or amorphous structure. Upon complete decompression, the spectrum of the recovered sample, especially the O-H stretch mode does not exhibit a similar profile to that of the original sample, suggesting that the framework has been partially modified. Hence the modification of activated framework is irreversible, in strong contrast to that of as-made sample. Nonetheless, the other major IR bands of the recovered sample are still characteristic of the organic linker, indicating that the entire activated framework has survived a compression pressure of 9.3 GPa without a permanent breakdown although the local structures have been modified.

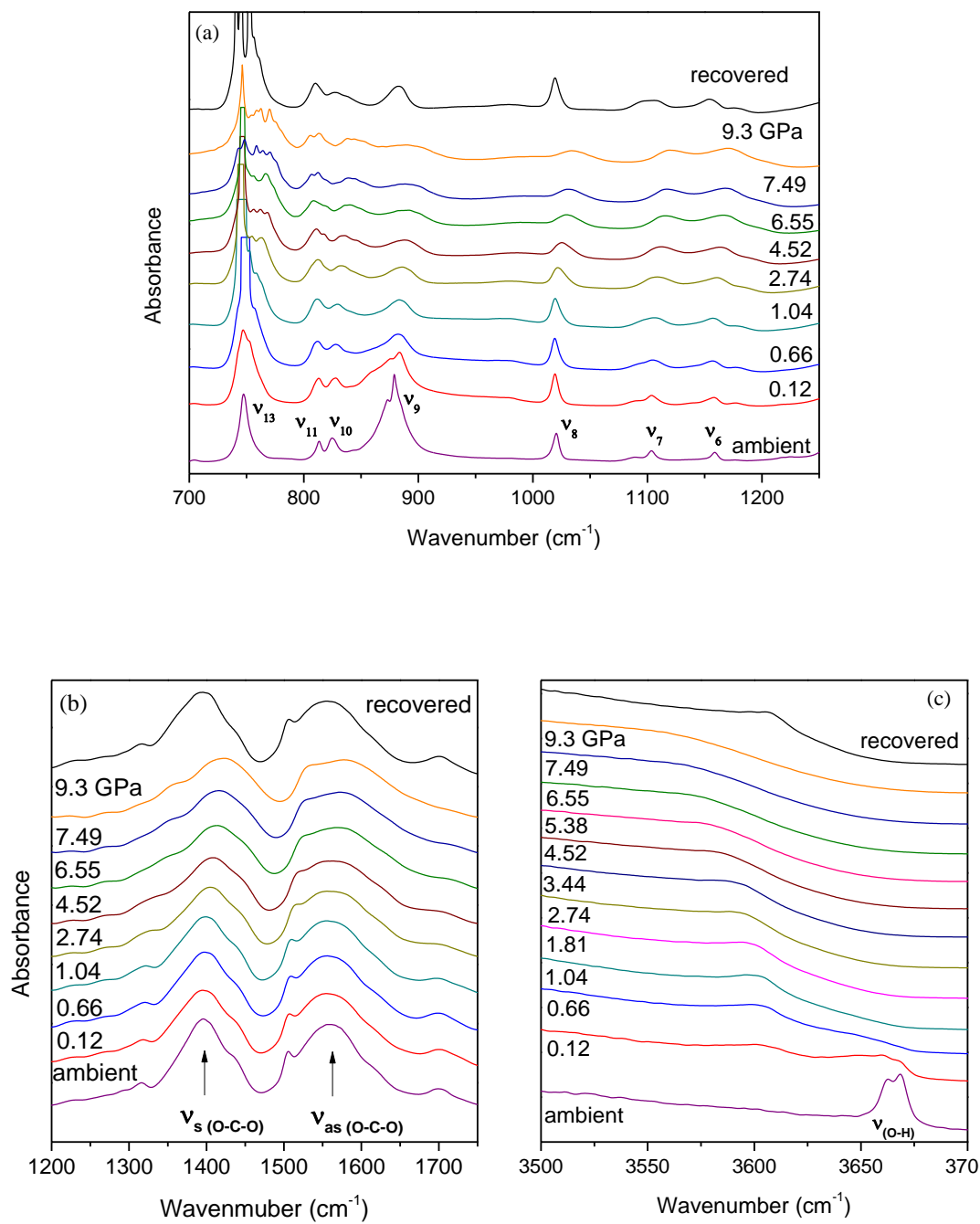


**Figure 4-5.** IR spectra of activated MIL-68(In) upon compression in the frequency region (a) 700-1250  $\text{cm}^{-1}$ ; (b) 1200-1750  $\text{cm}^{-1}$ ; (c) 3500-3700  $\text{cm}^{-1}$ .

In order to have a better understanding of pressure effects on the structure, the frequency of selected IR modes of activated MIL-68(In) as a function of pressure were illustrated in Figure 4-6, along with the pressure dependences listed in Table 4-3. For most of the bands in Figure 4-6a besides  $\nu_{\text{O-H}}$ , the pressure coefficients are small in magnitude (i.e.,  $< 5 \text{ cm}^{-1}\cdot\text{GPa}^{-1}$ ), indicating that the bond strength is not very sensitive to compression in a broad pressure region. Also these IR modes (except for  $\nu_{11}$  mode) exhibit regular pressure-induced blue shifts, in accord with that the bonds become stiffened upon compression. However, the O-H stretch modes exhibit an obvious red shifts, suggesting the weakening of O-H bonds. Upon slight compression to 0.12 GPa, the O-H modes (a doublet) merge into a single peak and its frequency drops with increasing pressure. Meanwhile, it can be seen from Figure 4-6b that although the carboxylate bands show small blue shifts overall, the frequency of both of the peaks ( $\nu_5$  and  $\nu_3$ ) decreases upon compression to 0.13 GPa. The initial weakening of both O-H and C-O modes suggest the strengthening of metal-linker (In-O) bonds that consist of In-O octahedron, in which all the six oxygens are either connected to carbon (denoted as  $\text{O}_1$ , Figure 4-7a) or hydrogen atoms (denoted as  $\text{O}_2$ ). As pressure increases, the O-H mode becomes further weakened (red shift) while the C-O modes are stiffened (blue shift). The opposite pressure behavior of these two modes may be due to the slight distortion of the In-O octahedron, since all the oxygens are connected to the In center. Previous high-pressure studies on  $\text{Mg}(\text{OH})_2$  and  $\text{Ca}(\text{OH})_2$  observed similar red shift of the O-H stretch mode upon compression and suggest that the negative pressure dependence of the mode is due to the influence of hydrogen bonding on the O-H vibration.<sup>59</sup> In our case, the distance from the hydrogen atom of a hydroxyl group to one of the adjacent oxygen of the octahedral units is  $\sim 3 \text{ \AA}$  with the O-H-O angle of  $\sim$

78 ° at ambient pressure (Figure 4-7a), which does not favor the condition of hydrogen bonding. However when the framework is compressed under high pressure, the OH units are highly stretched and subsequently the distance between hydroxyl hydrogen and the adjacent oxygen as well as the angle of O-H-O are significantly changed (Figure 4-7b), leading to the formation of hydrogen bonding within the framework. In addition, the slight distortion of In-O octahedral units facilitates the formation of hydrogen bonds. *In situ* X-ray diffraction measurements of the framework, especially the changes of In-O distances under high pressures would be helpful to further support the speculation. Nonetheless, the pores of the activated framework remain intact in the pressure range from ambient to 9.3 GPa.

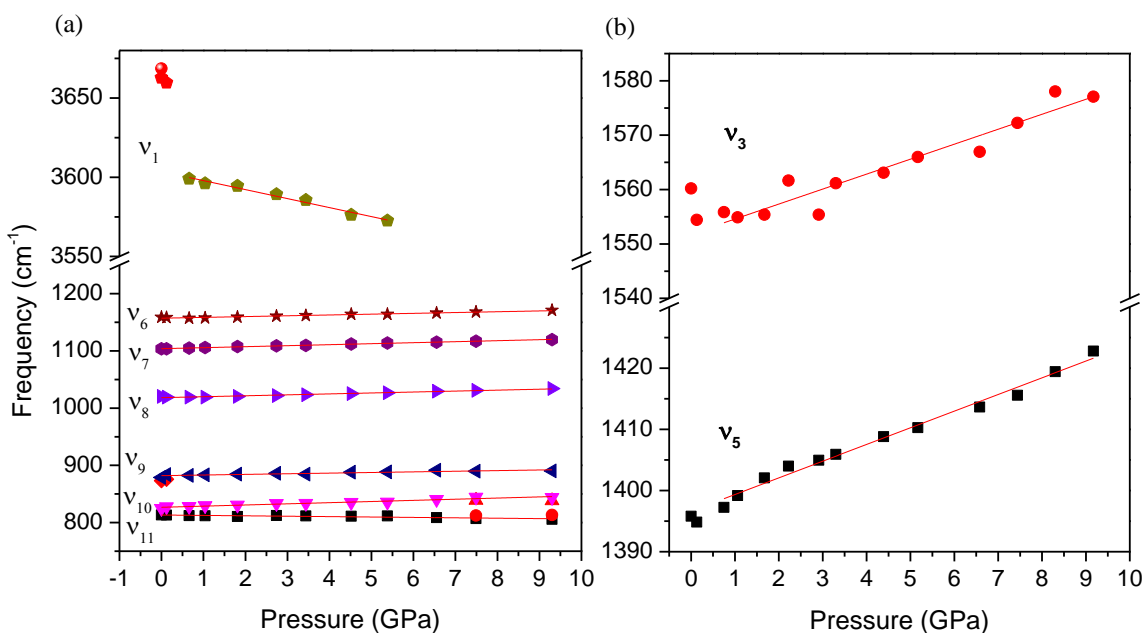


**Figure 4-6.** Frequency of IR modes of activated MIL-68(In) as a function of pressure from 0 to 9 GPa in the spectral region of (a) 750-3680  $\text{cm}^{-1}$ ; (b) 1390-1585  $\text{cm}^{-1}$ .

**Table 4-3.** Pressure dependence ( $dv/dP$ ,  $\text{cm}^{-1} \text{GPa}^{-1}$ ) of IR modes of activated MIL-68(In) from 0 to 9 GPa

<b>IR Mode</b>	<b>Frequency (<math>\text{cm}^{-1}</math>)</b>	<b><math>dv/dP</math> (<math>\text{cm}^{-1} \text{GPa}^{-1}</math>)</b>
v <sub>1</sub>	3643	-5.7
v <sub>3</sub>	1570	2.8
v <sub>5</sub>	1400	2.8
v <sub>6</sub>	1157	1.4
v <sub>7</sub>	1091	1.7
v <sub>8</sub>	1020	1.6
v <sub>9</sub>	877	1.1
v <sub>10</sub>	823	2.0
v <sub>11</sub>	813	-0.7



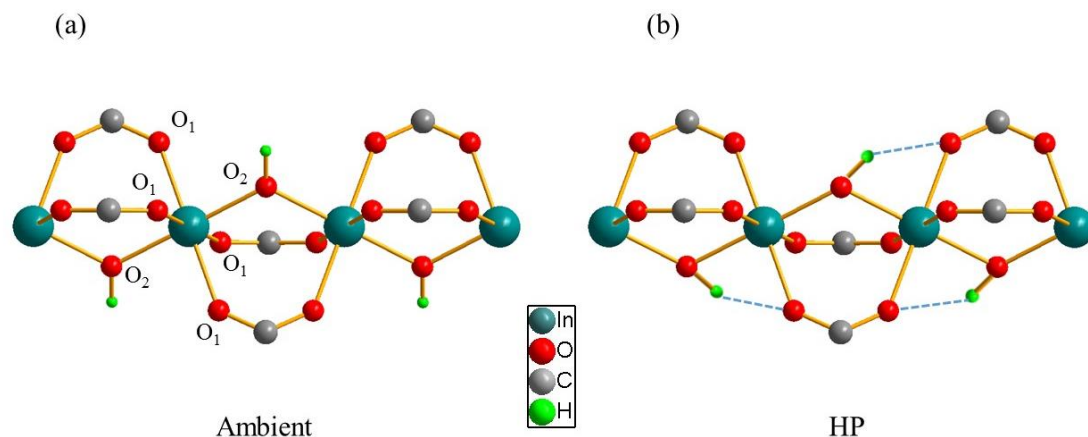


**Figure 4-7.** Illustration of local structure of MIL-68(In) at (a) ambient pressure; (b) high pressure (HP), showing hydrogen bonding between the OH units and carboxyl oxygens.

#### 4.3.4 IR spectra of activated MIL-68(In) with PTM upon compression

The above studies involve the pressure effects on as-made and activated MIL-68(In) under non-hydrostatic compression, in which the existence of solvent molecules inside the as-made framework is believed to be responsible for the different pressure behavior of the two samples. Besides the influence of solvent molecules on the pressure behavior of MOFs, the interaction between the framework and PTM, which distribute the pressure homogeneously in the sample chamber has also been shown to play an important role in the framework stability and phase transition. For example, Chapman *et al.*<sup>39</sup> reported different compressibility of Cu-btc framework, which depends on the size and penetrability of the guest molecules. Graham *et al.*<sup>41</sup> showed that application of pressure on Cu-btc causes solvent to be squeezed into the pores until a phase transition occurs, driven by the sudden compression and expansion of equatorial and axial Cu–O bonds. Lapidus *et al.*<sup>36</sup>

demonstrated that new phases of molecular framework  $\text{Zn}(\text{CN})_2$  can be formed under pressure by using different pressure transmitting fluids. Specifically, the transition is driven by an increase in overall atomic packing density by including fluid molecules in the pores of framework. Thus the study of influence of PTM on the framework under high pressure is of great interest.

The following results show the activated framework being compressed up to 18 GPa with the use of a PTM, which allows pressure to be applied evenly to the framework. Nujol, a mixture of alkanes of size ranging from  $\text{C}_{15}$  to  $\text{C}_{40}$  was used as the hydrostatic medium. Upon compression the O-H stretch modes ( $\nu_1$ ) merge into a single peak and then is gradually broadened, in contrast to the drastic changes of O-H bands under non-hydrostatic compression (Figure 4-8a). The gradual change of O-H mode indicates the O-H bond is not that sensitive to compression with the existence of PTM. The other major IR bands, i.e. the carboxylate stretch modes and the ring bending modes ( $\nu_3 - \nu_{13}$ ), also show continuous pressure-induced broadening during compression. At the highest pressure of 18.02 GPa, most of the bands were much broadened compared with those at ambient pressure, suggesting a transition to an amorphous structure. However, upon complete decompression, the recovered material exhibited a very similar profile to the original sample. These observations indicate that the structural modifications of MIL-68(In) are mostly reversible with the existence of hydrostatic fluids in a higher pressure region in which the framework structure are highly conserved.

The frequency of selected IR modes of MIL-68(In) with PTM are shown in Figure 4-8b. The pressure dependences listed in Table 4-4 are generally small in magnitude, which are consistent with those of IR modes under non-hydrostatic compression. The O-H stretch

mode still shows red shift as pressure increases, indicating the weakening of the O-H bond. However, the lower pressure dependence of the OH mode ( $-1.03 \text{ cm}^{-1}/\text{GPa}$ ) in the region 2-18 GPa, compared to that ( $-5.67 \text{ cm}^{-1}/\text{GPa}$ ) under non-hydrostatic compression indicates that the OH units are less pressure-sensitive with the existence of PTM in a much broader pressure range. The pressure dependences of all the other modes of MIL-68(In) are lower than those of activated framework as well, suggesting that the framework is less compressible in the company of PTM. The enhanced stability of the framework usually results from the pressure-induced inclusion of guest molecules in the pores of MOFs. For example, previous X-ray studies on ZIF-8 showed that the framework began to amorphize at 0.34 GPa without PTM, whereas stayed crystalline at 1.47 GPa with PTM due to its interaction with the framework.<sup>32,33</sup> For MIL-68 (In), the guest nujol molecules are small enough (5-7 Å) to be forced into the large hexagonal channels of the framework upon compression.<sup>60</sup> The space-filling mechanism makes the framework more resilient to compression and thus the OH units are much less pressure-sensitive.

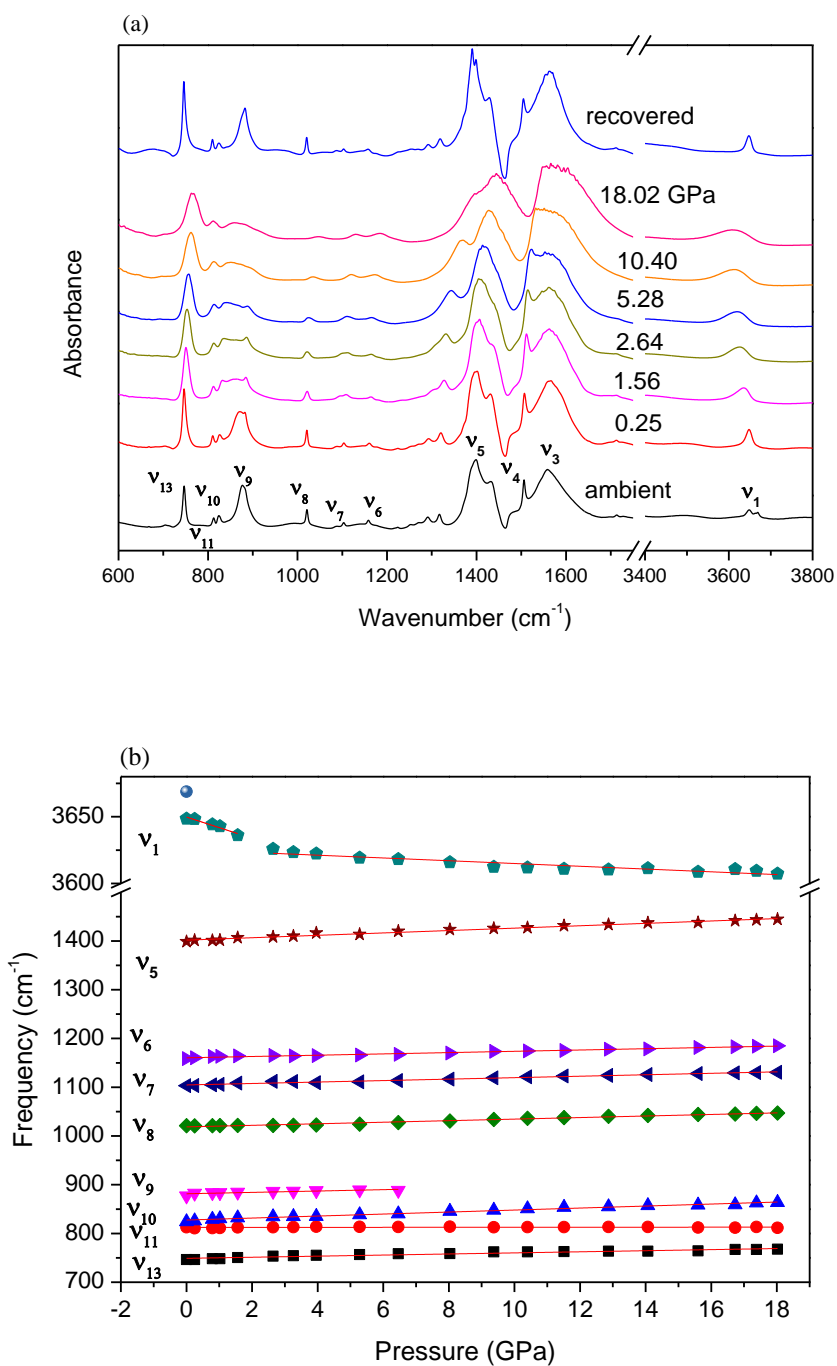


**Figure 4-8.** (a) IR spectra of activated MIL-68(In) with PTM upon compression. (b) Frequency of IR modes of activated MIL-68(In) with PTM as a function of pressure from 0 to 18 GPa.

**Table 4-4.** Pressure dependence ( $dv/dP$ ,  $\text{cm}^{-1} \text{GPa}^{-1}$ ) of IR modes of activated MIL-68(In) with PTM from 0 to 18 GPa.

IR Mode	Frequency ( $\text{cm}^{-1}$ )	$dv/dP$ ( $\text{cm}^{-1} \text{GPa}^{-1}$ )	
		(0-2 GPa)	(3-18 GPa)
$\nu_1$	3643	-7.9	-1.0
$\nu_5$	1400		2.5
$\nu_6$	1157		1.3
$\nu_7$	1091		1.5
$\nu_8$	1020		1.6
$\nu_9$	877		1.4
$\nu_{10}$	823		2.1
$\nu_{11}$	813		0.0
$\nu_{13}$	746		1.1

#### 4.3.5 IR spectra of activated MIL-68(In) loaded with CO<sub>2</sub> upon compression

MOFs are known for their application of green-house gases storage. The adsorption performance of MIL-68(Al), one of the MIL-68 family, has been well investigated by Yang and his co-workers,<sup>21</sup> who demonstrated that CO<sub>2</sub> molecules mainly occupy the hexagonal pores through the interaction with OH groups upon adsorption (up to 50 bar) while the triangular pores remain inaccessible for CO<sub>2</sub>. It would be interesting to see the performance of the framework for CO<sub>2</sub> adsorption when the pressure is elevated to gigapascal range. Figure 4-9 shows the IR spectrum of MIL-68(In) loaded with CO<sub>2</sub> compared with the spectrum of pure framework at a similar pressure (0.4 GPa), in which some major differences can be observed. Firstly, a few additional peaks can be seen in the top spectrum due to the existence of CO<sub>2</sub>: the bending mode of CO<sub>2</sub> ( $\nu_2$ ) at around 670 cm<sup>-1</sup> and the combination modes of  $\nu_3 + 2\nu_2$  and  $\nu_3 + \nu_1$  at ~ 3600 and 3700 cm<sup>-1</sup> respectively. The asymmetric stretching mode ( $\nu_3$ ) at 2325 cm<sup>-1</sup> is not shown in the figure because of its extremely high absorption intensity. Furthermore, the splitting of  $\nu_2$  and  $\nu_3 + \nu_1$  mode of CO<sub>2</sub> suggests that there are two types of CO<sub>2</sub> in the mixture. The one with higher frequency is consistent with the CO<sub>2</sub> outside the framework in the pressure medium in solid state and the one with lower frequency represents the CO<sub>2</sub> molecules trapped inside the framework, a similar scenario discussed in our previous work.<sup>42</sup> Therefore, the splitting of the CO<sub>2</sub> IR modes clearly suggests the CO<sub>2</sub> adsorption in the framework. Secondly, one of the  $\nu_{OH}$  modes, which is assigned to the OH groups in the triangular pores, is unaffected upon the insertion of CO<sub>2</sub> in the framework, in strong contrast to the pressure behavior of the OH groups in the activated framework upon compression. This observation suggests that the insertion of CO<sub>2</sub> enhanced the stability of the framework. According to Yang's study, the

OH groups of MIL-68(Al) would completely vanish upon the adsorption of gases including  $\text{CD}_3\text{CN}$ ,  $\text{CO}_2$  and  $\text{H}_2\text{S}$ , due to the strong interaction between the guest and host.<sup>21</sup> As a result, the fact that the OH band of the triangular pores stays relatively unaffected while the  $\text{CO}_2$  is inserted into the framework indicates that the triangular channels is not readily accessible to  $\text{CO}_2$  at 0.42 GPa. We thus concluded that  $\text{CO}_2$  molecules mainly occupy the hexagonal channels of the framework upon initial compression. Thirdly, both the symmetric OCO stretching ( $\nu_5$ ) and asymmetric OCO stretching ( $\nu_3$ ) in the spectrum of MIL-68(In) loaded with  $\text{CO}_2$  show an obvious blue shift with respect to the OCO modes of the activated framework, suggesting that the O-C-O bonds become stronger (Figure 4-9b). This indicates the interaction between  $\text{CO}_2$  and the framework makes the framework less compressible and more robust. Moreover, an additional peak at around  $1350\text{ cm}^{-1}$ , which can be assigned as a combination mode of CCH bending and C=C stretching, was observed in the IR profile of MIL-68(In) loaded with  $\text{CO}_2$ , as a result of the interaction between  $\text{CO}_2$  and the framework. The appearance of this mode, strongly suggests the host-guest interaction on the specific site of the organic linker. Our molecular mechanics simulations provide more detailed information which will be discussed next. Overall, our spectroscopic observations are not only consistent with the previous study but also demonstrate the enhanced interactions between  $\text{CO}_2$  and MIL-68 framework under high pressure.

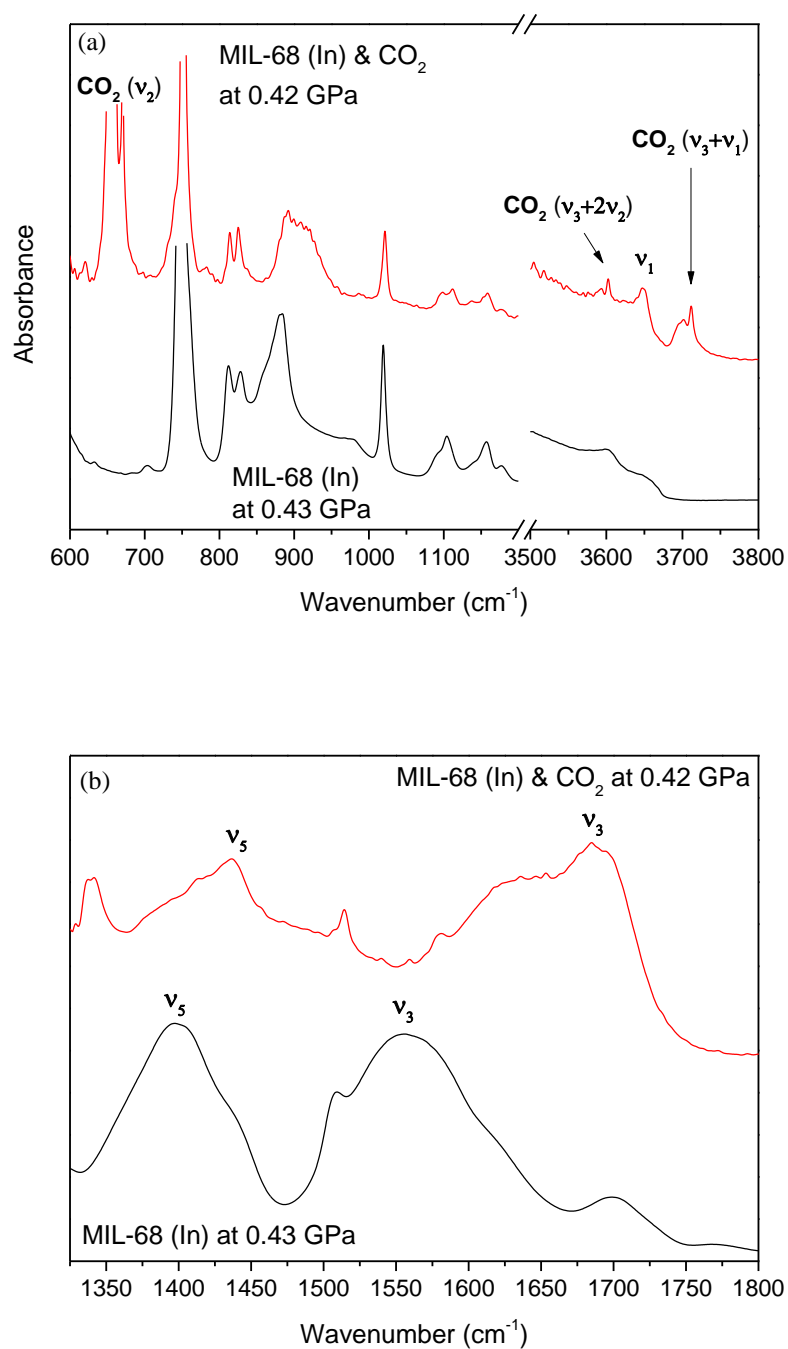


**Figure 4-9.** IR spectra of activated MIL-68(In) and MIL-68(In) loaded with CO<sub>2</sub> at around 0.4 GPa in the frequency region (a) 600-3800 cm<sup>-1</sup>; (b) 1325-1800 cm<sup>-1</sup>.



Upon compression of MIL-68(In) loaded with CO<sub>2</sub> to 0.96 GPa, as seen in Figure 4-10a, the OH stretching mode becomes gradually broadened, indicating the enhanced interaction between CO<sub>2</sub> and OH groups in the triangular channels of the framework. Besides, it is clear that the OH stretching mode experiences a red shift upon compression. (See the IR frequency of the O-H stretch mode as function of pressure in Figure 4-11 and the pressure dependence in Table 4-5.) It is further weakened as pressure increases and eventually disappears above 1.50 GPa. Highly likely, CO<sub>2</sub> forms strong hydrogen bonds between its oxygen atom and the hydrogen atom of OH groups in the pores. Upon decompression the pressure behavior of OH band is found to be reversible, as seen in Figure 4-10b, suggesting that CO<sub>2</sub> molecules substantially migrate out of the triangular pores of the framework (below 1.5 GPa). Therefore, the OH group is a key indicator of the insertion and extrusion of CO<sub>2</sub> into the triangular pores of MIL-68(In) in response of pressure. When the pressure is down to 0.34 GPa, the  $\nu_3 + \nu_1$  doublet of CO<sub>2</sub> can still be observed, showing that CO<sub>2</sub> remains in the bigger hexagonal pores of the framework. When the pressure is completely released, the CO<sub>2</sub> molecules escape from both the pores, as all the CO<sub>2</sub> characteristic peaks are no longer observable.

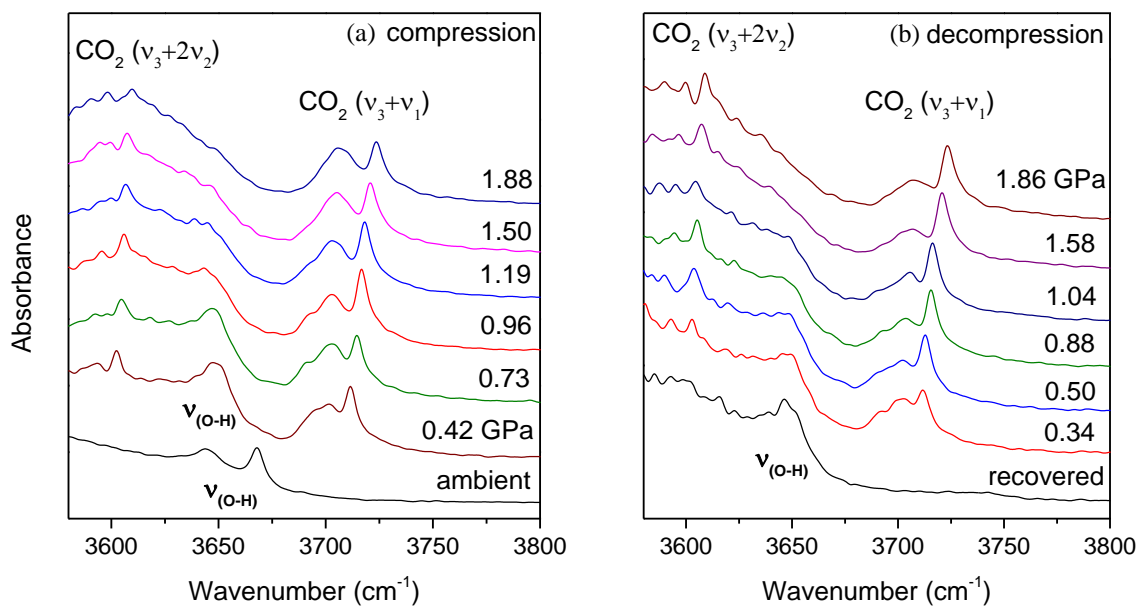


**Figure 4-10.** IR spectra of MIL-68(In) loaded with CO<sub>2</sub> upon (a) compression and (b) decompression in the frequency region 3580-3800 cm<sup>-1</sup>.

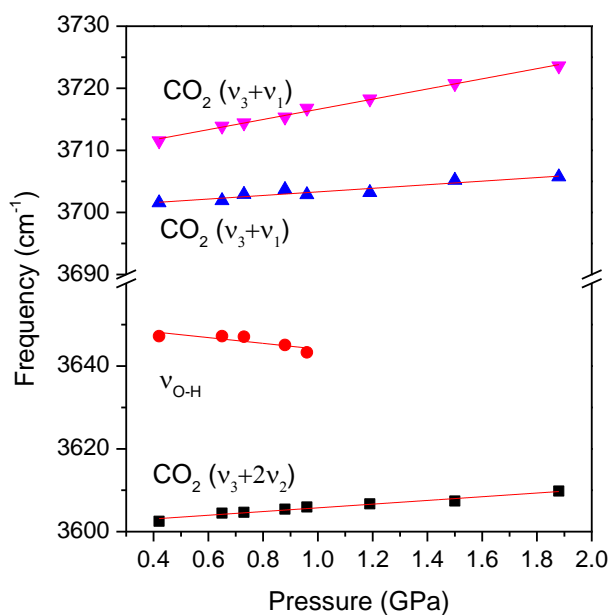


**Figure 4-11.** Frequency of the combination modes of CO<sub>2</sub> and the OH stretch mode of MIL-68(In) as a function of pressure from 0.42 to 1.88 GPa.

**Table 4-5.** Pressure dependence ( $dv/dP$ , cm<sup>-1</sup> GPa<sup>-1</sup>) of the combination modes of CO<sub>2</sub> and the OH stretch mode of MIL-68(In) from 0.42 to 1.88 GPa

IR Mode	Frequency (cm <sup>-1</sup> )	$dv/dP$ (cm <sup>-1</sup> GPa <sup>-1</sup> )
$\nu_3 + \nu_1$ (CO <sub>2</sub> )	3711	8.2
$\nu_3 + \nu_1$ (CO <sub>2</sub> )	3701	2.9
$\nu_{O-H}$	3647	-7.0
$\nu_3 + 2\nu_2$ (CO <sub>2</sub> )	3602	4.5

## 4.4 Discussion

The above results showed different pressure behavior among four different systems: the as-made MIL-68(In), the activated framework, the activated sample with PTM and the activated framework loaded with CO<sub>2</sub>. In the pressure range of 0-9 GPa, the activated framework undergoes an irreversible transformation upon recovery, whereas the as-made framework and especially the OH units experience a completely reversible deformation. The solvent molecules occluded in the channels of as-made framework are believed to play a key role in restoring the structure and crystallinity of the framework when the pressure was released. Prior studies of as-made ZSM-5 (Zeolite Socony Mobil-5)<sup>61</sup> under high pressure showed that the interaction between the template molecules and zeolite framework preserves the local structures associated with the original topology at high pressure. Upon releasing pressure, the template redirects the silicate species to partially reform the initial topology. For as-made framework of MIL-68(In), the solvent molecules DMF may play similar role to that of template molecules in ZSM-5. For the activated framework, the weakening and soft behavior of OH modes is associated with the formation of hydrogen bonding between the adjacent In-O octahedrons within the framework. The OH modes are not recovered upon complete decompression as the empty framework is partially modified during compression. The existence of solvent molecules is thus clearly pivotal to the reversibility of the framework.

The stability of activated MIL-68(In) is significantly enhanced when nujol is added as the hydrostatic medium with the sample, because of the pressure-induced insertion of nujol into the pores of the framework. Previous high-pressure studies of porous molecular frameworks have demonstrated the potential for fluid molecules to progressively fill the

pores with increasing pressure.<sup>36,39,40</sup> For MIL-68(In), the nujol molecules act as an inert space-filling agent which makes the framework more resistant to pressure. As a result, the OH units remain unaffected and are much less sensitive to pressure than that of the framework without hydrostatic medium.

As guest molecules to the MIL-68 framework, both nujol and CO<sub>2</sub> were found to enhance the stability of the framework. However, they have different impacts on the compression behavior of the MIL-68(In) framework, especially on the OH bridging units. Nujol appears to serve as the physical space-filling agent that makes the framework less compressible and thus the OH groups remain intact and only show red shift upon compression. In contrast, CO<sub>2</sub> not only serves as a pressure medium, but chemically interacts with the framework. Due to the strong interaction of hydrogen bonding between the OH units and CO<sub>2</sub>, the IR intensity of the OH band of the hexagonal pores substantially diminished upon initial CO<sub>2</sub> loading (even at 1 atm) while the OH band of the triangular pores without CO<sub>2</sub> occupying remains. At elevated pressure around 1.5 GPa, the OH band of the triangular pores finally vanishes as CO<sub>2</sub> are forced into the small channels. These unique signatures strongly suggest the chemical nature of the guest-host interaction in the CO<sub>2</sub> loaded activated framework.

The differential accessibility exhibited by the hexagonal pores (i.e., for CO<sub>2</sub> or other larger guest molecules (nujol) at low pressures, e.g., < 0.35 GPa) the triangular pores (i.e., for CO<sub>2</sub> at elevated pressure of > 1.5 GPa) is of great interest. Yang's computational study<sup>21</sup> demonstrated that CO<sub>2</sub> molecules are preferentially accommodated in the triangular pores due to a higher degree of confinement that creates the strongest energetic adsorption sites. However, the MIL-68(Al) framework in their work was not fully activated, thus leaving

the triangular pores inaccessible for small gas molecules under adsorption pressure (up to 50 bar). Our study is thus not inconsistent with the previous work at pressures that are lower than 1 GPa. When pressure was extended to 1.5 GPa, the CO<sub>2</sub> molecules can be squeezed into the triangular channels and the process is found to be reversible upon decompression. Thus pressure can play a regulating role in the insertion and extrusion of CO<sub>2</sub> molecules with respect to the triangular pores of MIL-68(In). The CO<sub>2</sub> adsorption in the triangular pores of MIL-68(In) is herein reported for the first time experimentally.

To understand the differential binding affinity of CO<sub>2</sub> inside the MIL-68 framework and the origin of the chemical nature of guest-host interactions at high pressures, we performed Grand Canonical Monte Carlo simulations on the adsorption behavior of CO<sub>2</sub> at different external compression pressures. Figure 4-11 shows the CO<sub>2</sub> probability density distributions in the MIL-68 framework at three representative pressures, i.e., ambient, 0.1 GPa and 10 GPa. These pressures were chosen to examine 1) the reproducibility of the simulation method on the adsorption behaviour of CO<sub>2</sub> studied before and 2) the trend and pressure-dependence of CO<sub>2</sub> adsorption at relatively lower and higher pressure aligned with the two experimentally identified pressure regions. At ambient pressure, the simulations show a CO<sub>2</sub> probability density of 90% at the triangular channel centre, suggesting that the triangular channel is the preferred binding sites. This result is consistent with that by Yang *et al.*<sup>21</sup> When compressed to about 1 kbar, the CO<sub>2</sub> distribution density is substantially shifted to the hexagonal channel. Although some density is found in the triangular channel at this pressure, the CO<sub>2</sub> probability density in the hexagonal channel is dominant over the triangular channels with a ratio of 90%:10%, highly consistent with our experimental observation that at below 0.35 GPa, the hexagonal channel is the preferential

binding channel of CO<sub>2</sub>. At the highest simulation pressure, i.e., 10 GPa, we found that both hexagonal and triangular channels are clearly occupied by CO<sub>2</sub>. The probability distribution values suggest that triangular pores are slightly more populated by CO<sub>2</sub> (i.e., 13%) than that at 0.1 GPa and the overall CO<sub>2</sub> adsorption capacity was found to be 10% higher than that at 0.1 GPa, in excellent accord with our experimental observations.

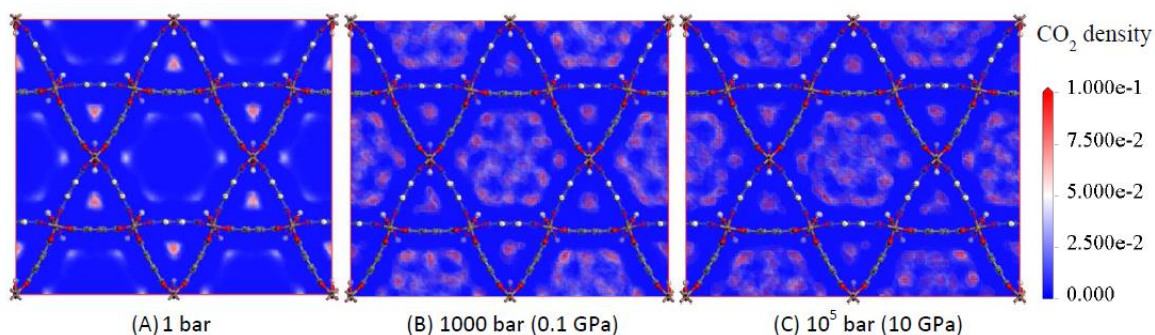


**Figure 4-12.** Simulated contour plots of the CO<sub>2</sub> probability density (in arbitrary unit) distributions along the hexagonal and triangular channels of MIL-68(In) framework at (A) 1 bar, (B) 1000 bar or 0.1 GPa and (C) 10<sup>5</sup> bar (or 10 GPa).

Finally, we examined the CO<sub>2</sub> storage capacity by MIL-68 based on the IR absorption intensity of the two components of the  $\nu_3 + \nu_1$  combination mode. We estimated that up to  $\sim 62\%$  of the loaded CO<sub>2</sub> was inserted in the framework (including the hexagonal and triangular pores) upon compression representing an enhanced CO<sub>2</sub> intake capacity compared to ZIF-8 framework (i.e.,  $\sim 33\%$ ) that we reported previously.<sup>42</sup> The different CO<sub>2</sub> storage capacities as well as different compression behaviors of CO<sub>2</sub> in the framework are believed to be associated with the structural difference and thus the different guest-host interaction mechanism between MIL-68 and ZIF-8. For instance, the CO<sub>2</sub> molecules absorbed in MIL-68(In) are more sensitive to pressure than CO<sub>2</sub> trapped in ZIF-

8. According to Figure 4-10a, the pressure dependences for  $\nu_3 + 2\nu_2$  and  $\nu_3 + \nu_1$  mode of  $\text{CO}_2$  inside the framework of MIL-68(In) are 4.47 and 2.88  $\text{cm}^{-1} \text{GPa}^{-1}$  respectively, which are higher than those of  $\text{CO}_2$  trapped in ZIF-8.<sup>42</sup> This is mainly due to the difference in the pore size and opening between the two frameworks. ZIF-8 has three-dimensional cavities with a small window size (3.4 Å), while MIL-68 (In) contains much larger one-dimensional open channels (16 Å for the hexagonal channel and 6 Å for the triangular channel). Once trapped,  $\text{CO}_2$  molecules in MIL-68(In) have a less confined environment than  $\text{CO}_2$  inside the cavities of ZIF-8 and thus are more pressure-sensitive. Moreover, the  $\text{CO}_2$  adsorption mechanism and the host-guest interactions vary in the two frameworks. For  $\text{CO}_2$  adsorption in ZIF-8, the framework flexibility and pressure-induced enlargement of pore opening play an important role in the facilitation of  $\text{CO}_2$  insertion, which mainly locate in the regions close to the organic imidazolate linkers through van der Waals' interaction.<sup>62</sup> On the other hand, the MIL-68(In) framework contains the OH units, which serve as the binding sites for  $\text{CO}_2$  adsorption through hydrogen bonding between each other. It has been established that in order to enhance the  $\text{CO}_2$  binding affinity in MOFs, three main approaches are most intensively investigated which includes amine grafting, introducing strongly polarizing functional groups and open metal cation sites.<sup>63</sup> In this case, the OH units of MIL-68(In) serve as functional groups that can offer enhancement of  $\text{CO}_2$ -MOF interactions. As a result,  $\text{CO}_2$  molecules preferentially reside at the corners of the hexagonal pores near OH units of the framework upon initial adsorption. Our molecular mechanics simulations clearly suggest that the regions near the OH units in the hexagonal channels are the preferential binding sites for  $\text{CO}_2$  with highest density distributions (Figure 4-11). Upon further compression to above 1.5 GPa,  $\text{CO}_2$  substantially occupy both the whole hexagonal



pores and the triangular pores with larger regions than at lower pressures. Therefore the existence of OH units as the CO<sub>2</sub> binding sites makes the guest-host interaction stronger for MIL-68(In), and the large pore sizes further contribute to the superior adsorption performance of MIL-68(In).

## 4.5 Conclusions

In summary, the behavior of as-made and activated MIL-68(In) and their reversibilities under high pressure were investigated by IR spectroscopy. Overall, the structures of both frameworks are highly stable upon compression to 9 GPa, but with some modifications on the local structure especially the bridging O-H units, which are very sensitive to pressure. Upon the release of external pressure, the structural modifications are found to be completely reversible for as-made MIL-68(In) while irreversible for the activated framework. The difference in the reversibility of framework is attributed to the solvent DMF molecules contained in the channels. In addition, the stability of the activated framework was studied under hydrostatic compression by using PTM. The pressure-induced inclusion of PTM makes the framework more resilient to pressure (18 GPa) and the structural modifications are completely reversible upon decompression. Furthermore, the performance of MIL-68(In) for CO<sub>2</sub> adsorption under high pressure was investigated. Our results show that the hexagonal pores are readily accessible for CO<sub>2</sub> at relative low pressures (e.g., < 0.35 GPa), while the triangular pores becomes accessible for CO<sub>2</sub> at elevated pressures (e.g., > 1.5 GPa). The pressure-regulated CO<sub>2</sub> occupation in different channels of the MIL-68 framework is found to be reversible between compression and decompression. The unique adsorption behavior of CO<sub>2</sub> in the framework is associated

with the OH units that contribute as the primary binding sites through hydrogen bonding with CO<sub>2</sub>. These observations are strongly supported by our simulation results. The high stability and enhanced CO<sub>2</sub> adsorption of MIL-68(In) under high pressure makes it a promising candidate for greenhouse gas storage.

## 4.6 Reference

- (1) Furukawa, H.; Cordova, K. E.; O’Keeffe, M.; Yaghi, O. M. *Science* **2013**, *341*, 1230444.
- (2) Sumida, K.; Rogow, D. L.; Mason, J. A.; McDonald, T. M.; Bloch, E. D.; Herm, Z. R.; Bae, T. H.; Long, J. R. *Chemical Reviews* **2012**, *112*, 724.
- (3) Furukawa, H.; Yaghi, O. M. *Journal of the American Chemical Society* **2009**, *131*, 8875.
- (4) Murray, L. J.; Dinca, M.; Long, J. R. *Chemical Society Reviews* **2009**, *38*, 1294.
- (5) Ma, S.; Zhou, H.-C. *Chemical Communications* **2010**, *46*, 44.
- (6) Sculley, J.; Yuan, D.; Zhou, H.-C. *Energy & Environmental Science* **2011**, *4*, 2721.
- (7) Li, J.-R.; Kuppler, R. J.; Zhou, H.-C. *Chemical Society Reviews* **2009**, *38*, 1477.
- (8) Chen, B.; Xiang, S.; Qian, G. *Accounts of Chemical Research* **2010**, *43*, 1115.
- (9) Li, J.-R.; Sculley, J.; Zhou, H.-C. *Chemical Reviews* **2011**, *112*, 869.
- (10) Farrusseng, D.; Aguado, S.; Pinel, C. *Angewandte Chemie International Edition* **2009**, *48*, 7502.
- (11) Lee, J.; Farha, O. K.; Roberts, J.; Scheidt, K. A.; Nguyen, S. T.; Hupp, J. T. *Chemical Society Reviews* **2009**, *38*, 1450.
- (12) Corma, A.; García, H.; Llabrés i Xamena, F. X. *Chemical Reviews* **2010**, *110*, 4606.
- (13) Zhao, M.; Ou, S.; Wu, C.-D. *Accounts of Chemical Research* **2014**, *47*, 1199.
- (14) Horcajada, P.; Serre, C.; Vallet-Regí M.; Sebban, M.; Taulelle, F.; Férey, G. *Angewandte Chemie International Edition* **2006**, *118*, 6120.
- (15) Huxford, R. C.; Della Rocca, J.; Lin, W. *Current Opinion in Chemical Biology* **2010**, *14*, 262.
- (16) McKinlay, A. C.; Morris, R. E.; Horcajada, P.; Férey, G.; Gref, R.; Couvreur, P.; Serre, C. *Angewandte Chemie International Edition* **2010**, *49*, 6260.

- (17) Della Rocca, J.; Liu, D.; Lin, W. *Accounts of Chemical Research* **2011**, *44*, 957.
- (18) Barthelet, K.; Marrot, J.; Ferey, G.; Riou, D. *Chemical Communications* **2004**, *5*, 520.
- (19) Volkringer, C.; Meddouri, M.; Loiseau, T.; Guillou, N.; Marrot, J. r. m.; Férey, G. r.; Haouas, M.; Taulelle, F.; Audebrand, N.; Latroche, M. *Inorganic Chemistry* **2008**, *47*, 11892.
- (20) Fateeva, A.; Horcajada, P.; Devic, T.; Serre, C.; Marrot, J.; Grenèche, J.-M.; Morcrette, M.; Tarascon, J.-M.; Maurin, G.; Férey, G. *European Journal of Inorganic Chemistry* **2010**, *2010*, 3789.
- (21) Yang, Q.; Vaesen, S.; Vishnuvarthan, M.; Ragon, F.; Serre, C.; Vimont, A.; Daturi, M.; De Weireld, G.; Maurin, G. *Journal of Materials Chemistry* **2012**, *22*, 10210.
- (22) Wu, L.; Xue, M.; Qiu, S.-L.; Chaplais, G.; Simon-Masseron, A.; Patarin, J. *Microporous and Mesoporous Materials* **2012**, *157*, 75.
- (23) Bennett, T. D.; Tan, J. C.; Moggach, S. A.; Galvelis, R.; Mellot-Draznieks, C.; Reisner, B. A.; Thirumurugan, A.; Allan, D. R.; Cheetham, A. K. *Chemistry-A European Journal* **2010**, *16*, 10684.
- (24) Li, W.; Probert, M. R.; Kosa, M.; Bennett, T. D.; Thirumurugan, A.; Burwood, R. P.; Parinello, M.; Howard, J. A. K.; Cheetham, A. K. *Journal of the American Chemical Society* **2012**, *134*, 11940.
- (25) Ogborn, J. M.; Collings, I. E.; Moggach, S. A.; Thompson, A. L.; Goodwin, A. L. *Chemical Science* **2012**, *3*, 3011.
- (26) Ortiz, A. U.; Boutin, A.; Fuchs, A. H.; Coudert, F.-X. *Physical Review Letters* **2012**, *109*, 195502.
- (27) Ortiz, A. U.; Boutin, A.; Fuchs, A. H.; Coudert, F.-X. *The Journal of Physical Chemistry Letters* **2013**, *4*, 1861.
- (28) Cai, W.; Katrusiak, A. *Nature Communications* **2014**, *5*, 4337.
- (29) Bennett, T. D.; Sotelo, J.; Tan, J.-C.; Moggach, S. A. *CrystEngComm* **2015**, *17*, 286.
- (30) Serra-Crespo, P.; Dikhtiarenko, A.; Stavitski, E.; Juan-Alcaniz, J.; Kapteijn, F.; Coudert, F.-X.; Gascon, J. *CrystEngComm* **2015**, *17*, 276.
- (31) Su, Z.; Miao, Y.-R.; Mao, S.-M.; Zhang, G.-H.; Dillon, S.; Miller, J. T.; Suslick, K. S. *Journal of the American Chemical Society* **2015**, *137*, 1750.
- (32) Chapman, K. W.; Halder, G. J.; Chupas, P. J. *Journal of the American Chemical Society* **2009**, *131*, 17546.
- (33) Moggach, S. A.; Bennett, T. D.; Cheetham, A. K. *Angewandte Chemie International Edition* **2009**, *48*, 7087.

- (34) Hu, Y.; Kazemian, H.; Rohani, S.; Huang, Y.; Song, Y. *Chemical Communications* **2011**, 47, 12694.
- (35) Gagnon, K. J.; Beavers, C. M.; Clearfield, A. *Journal of the American Chemical Society* **2013**, 135, 1252.
- (36) Lapidus, S. H.; Halder, G. J.; Chupas, P. J.; Chapman, K. W. *Journal of the American Chemical Society* **2013**, 135, 7621.
- (37) Ortiz, A. U.; Boutin, A.; Gagnon, K. J.; Clearfield, A.; Coudert, F.-X. *Journal of the American Chemical Society* **2014**, 136, 11540.
- (38) Spencer, E. C.; Kiran, M. S. R. N.; Li, W.; Ramamurty, U.; Ross, N. L.; Cheetham, A. K. *Angewandte Chemie International Edition* **2014**, 53, 5583.
- (39) Chapman, K. W.; Halder, G. J.; Chupas, P. J. *Journal of the American Chemical Society* **2008**, 130, 10524.
- (40) Graham, A. J.; Allan, D. R.; Muszkiewicz, A.; Morrison, C. A.; Moggach, S. A. *Angewandte Chemie International Edition* **2011**, 50, 11138.
- (41) Graham, A. J.; Tan, J.-C.; Allan, D. R.; Moggach, S. A. *Chemical Communications* **2012**, 48, 1535.
- (42) Hu, Y.; Liu, Z.; Xu, J.; Huang, Y.; Song, Y. *Journal of the American Chemical Society* **2013**, 135, 9287.
- (43) Graham, A. J.; Banu, A.-M.; Duren, T.; Greenaway, A.; McKellar, S. C.; Mowat, J. P. S.; Ward, K.; Wright, P. A.; Moggach, S. A. *Journal of the American Chemical Society* **2014**, 136, 8606.
- (44) Li, Q.; Li, S.; Wang, K.; Liu, J.; Yang, K.; Liu, B.; Zou, G.; Zou, B. *The Journal of Physical Chemistry C* **2014**, 118, 5848.
- (45) Haines, J.; Cambon, O.; Levelut, C.; Santoro, M.; Gorelli, F.; Garbarino, G. *Journal of the American Chemical Society* **2010**, 132, 8860.
- (46) Lee, Y.; Liu, D.; Seoung, D.; Liu, Z. X.; Kao, C. C.; Vogt, T. *Journal of the American Chemical Society* **2011**, 133, 1674.
- (47) Santoro, M.; Gorelli, F.; Haines, J.; Cambon, O.; Levelut, C.; Garbarino, G. *Proceedings of the National Academy of Sciences* **2011**, 108, 7689.
- (48) Dong, Z. H.; Song, Y. *Journal of Chemical Physics C* **2010**, 114, 1782.
- (49) Delley, B. *The Journal of Chemical Physics* **2000**, 113, 7756.
- (50) Delley, B. *The Journal of Chemical Physics* **1990**, 92, 508.
- (51) Wang, Y.; Perdew, J. P. *Physical Review B* **1991**, 44, 13298.
- (52) Duren, T.; Bae, Y.-S.; Snurr, R. Q. *Chemical Society Reviews* **2009**, 38, 1237.

- (53) Mayo, S. L.; Olafson, B. D.; Goddard, W. A. *Journal of Physical Chemistry* **1990**, *94*, 8897.
- (54) Martin, M. G.; Siepmann, J. I. *Journal of Physical Chemistry B* **1998**, *102*, 2569.
- (55) Tález S, C. A.; Hollauer, E.; Mondragon, M. A.; Castaño, V. M. *Spectrochimica Acta Part A: Molecular and Biomolecular Spectroscopy* **2001**, *57*, 993.
- (56) Jacobs, P. A.; Mortier, W. J. *Zeolites* **1982**, *2*, 226.
- (57) Shearer, G.; Forselv, S.; Chavan, S.; Bordiga, S.; Mathisen, K.; Bjørgen, M.; Svelle, S.; Lillerud, K. *Topics in Catalysis* **2013**, *56*, 770.
- (58) Chen, B.; Wang, L.; Zapata, F.; Qian, G.; Lobkovsky, E. B. *Journal of the American Chemical Society* **2008**, *130*, 6718.
- (59) Kruger, M. B.; Williams, Q.; Jeanloz, R. *The Journal of Chemical Physics* **1989**, *91*, 5910.
- (60) Grice, K.; Mesmay, R. d.; Glucina, A.; Wang, S. *Organic Geochemistry* **2008**, *39*, 284.
- (61) Fu, Y. Q.; Song, Y.; Huang, Y. I. *Journal of Physical Chemistry C* **2012**, *116*, 2080.
- (62) Perez-Pellitero, J.; Amrouche, H.; Siperstein, F. R.; Pirngruber, G.; Nieto-Draghi, C.; Chaplais, G.; Simon-Masseron, A.; Bazer-Bachi, D.; Peralta, D.; Bats, N. *Chemistry-A European Journal* **2010**, *16*, 1560.
- (63) Zhang, Z.; Zhao, Y.; Gong, Q.; Li, Z.; Li, J. *Chemical Communications* **2013**, *49*, 653.

## Chapter 5

### 5 High Pressure Study of CO<sub>2</sub> Adsorption in MOF $\alpha$ -Mg<sub>3</sub>(HCOO)<sub>6</sub> by Vibrational Spectroscopy

#### 5.1 Introduction

Metal-organic frameworks (MOFs) are an emerging class of porous crystalline materials that are constructed from metal ion clusters and organic linkers.<sup>1,2</sup> The potential applications of MOFs such as gas storage and separation,<sup>3-7</sup> catalysis,<sup>8-12</sup> drug delivery<sup>13-15</sup> and sensors<sup>16-18</sup> have been studied extensively over the last decade. Within the large varieties of MOFs currently known, frameworks that have Mg<sup>2+</sup> ion as metal centers have received a considerable amount of attention, due to their low cost, nontoxicity and low atomic weight.<sup>19-22</sup> Out of this specific group of MOFs,  $\alpha$ -Mg<sub>3</sub>(HCOO)<sub>6</sub> further demonstrated its capability of being a gas storage material with its permanent porosity and good stability in various solvents within a wide temperature range.<sup>22</sup> The framework structure of  $\alpha$ -Mg<sub>3</sub>(HCOO)<sub>6</sub> which crystallizes in monoclinic space group P2<sub>1</sub>/n, along with the local structures of the Mg-O clusters are shown in Figure 1. The framework contains interconnecting one-dimensional chains of edge-shared octahedra of Mg1 and Mg3 with vertex-shared MgO<sub>6</sub> octahedra of Mg2 and Mg4 via Mg1, forming narrow one dimensional zig-zag channels along the b axis with the pore size 4.5 Å × 5.5 Å (Figure 5-1a). All of the formate anions adopt similar binding modes, with one oxygen connecting to a single metal center ( $\mu^1$ -O) and the second oxygen bridging between two other metals ( $\mu^2$ -O). There are three different coordination environments for the metal centers. Mg1 bonds to six  $\mu^2$ -O, Mg2 and Mg4 each bond to four  $\mu^1$ -O and two  $\mu^2$ -O, whereas Mg3 bonds to two  $\mu^1$ -O and four  $\mu^2$ -O (Figure 5-1b).

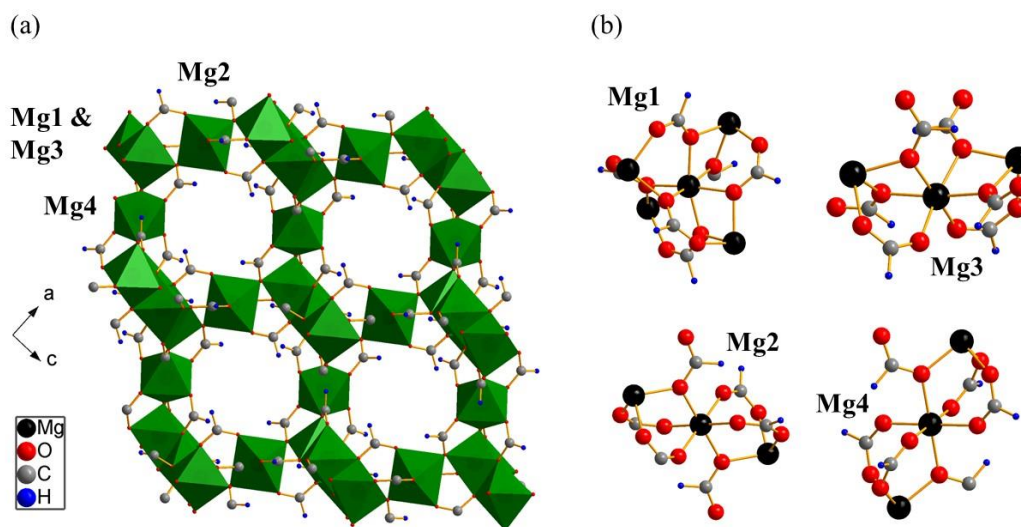


**Figure 5-1.** The structure of activated  $\alpha$ - $\text{Mg}_3(\text{HCOO})_6$  at ambient conditions. (a) The framework structure along  $b$  axis, showing the one-dimensional zigzag channels with a dimension of  $4.5 \text{ \AA} \times 5.5 \text{ \AA}$ . The green polyhedrons represent Mg-O clusters. (b) Four Different Mg coordination environments.

Our recent work on  $\alpha$ - $\text{Mg}_3(\text{HCOO})_6$  demonstrated its high stability against external high pressure up to 13 GPa, with an irreversible crystal-to-crystal transition above 2 GPa.<sup>23</sup> In addition,  $\alpha$ - $\text{Mg}_3(\text{HCOO})_6$  framework composed of exclusively carbonyl linkers that can be considered as substantial  $\text{CO}_2$  moiety in the framework suggests strong affinity between  $\text{CO}_2$  and  $\text{Mg}^{2+}$ , making additional intake of  $\text{CO}_2$  into the framework thermodynamically favorable. Thus the intrinsic rigidity of the framework as well as all the other properties listed makes the investigation of enhanced uptake of  $\text{CO}_2$  at much higher pressures than ambient an interesting possibility. In this work, we explored the effects of high external pressure on the  $\text{CO}_2$  adsorption in  $\alpha$ - $\text{Mg}_3(\text{HCOO})_6$  using Infrared (IR) and Raman

Spectroscopy, which demonstrated pressure-enhanced CO<sub>2</sub> interactions with the framework on compression.

## 5.2 Experimental section

The  $\alpha$ -Mg<sub>3</sub>(HCOO)<sub>6</sub> sample was synthesized according to the literature.<sup>22</sup> Specifically, a mixture of 10 mL DMF, 0.23 mL of formic acid (6 mmol) and 0.77 g of Mg(NO<sub>3</sub>)<sub>2</sub> · 6H<sub>2</sub>O (3 mmol) was placed in a 20 mL scintillation vial. The vial was capped and immersed in a silicon oil bath that was kept at a constant temperature of 110 °C for 40 h. During this period, high quality crystals of the as-made sample were deposited (0.34 g, 81.7%). The crystals could then be filtered in air until dry. Activated  $\alpha$ -Mg<sub>3</sub>(HCOO)<sub>6</sub> was obtained by heating the as-made sample to 130 °C for 36 h in vacuum condition. Its crystallinity was checked by XRD. A diamond anvil cell (DAC) equipped with type II diamonds with culet sizes of 600  $\mu$ m was used to generate high pressures. The pure desolvated  $\alpha$ -Mg<sub>3</sub>(HCOO)<sub>6</sub> powder samples were loaded into the DAC together with solid CO<sub>2</sub> in a cryogenic bath of liquid nitrogen at a temperature below the melting point of dry ice (i.e., < -78 °C). Then the cell was carefully sealed in the liquid nitrogen bath before warming up to room temperature. A few ruby chips were preloaded in the DAC as the pressure calibrant and the pressure was determined by the well-established ruby fluorescent method.<sup>24</sup> A customized IR and Raman micro-spectroscopic system with details described in *Chapter 1* were used for all mid-IR absorption and Raman measurements.<sup>23</sup> Far-infrared measurements were performed at the U2A beamline at the National Synchrotron Light Source (NSLS), Brookhaven National Laboratory (BNL). All measurements were performed under room temperature and multiple runs were carried out for reproducibility.

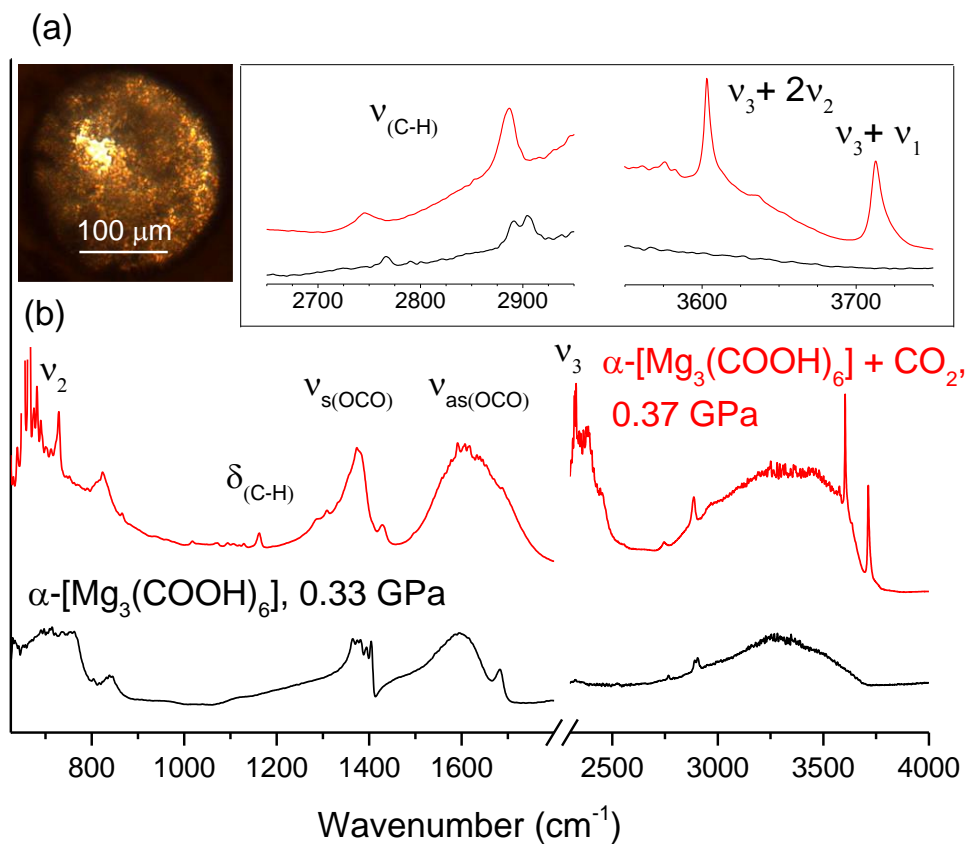


## 5.3 Results

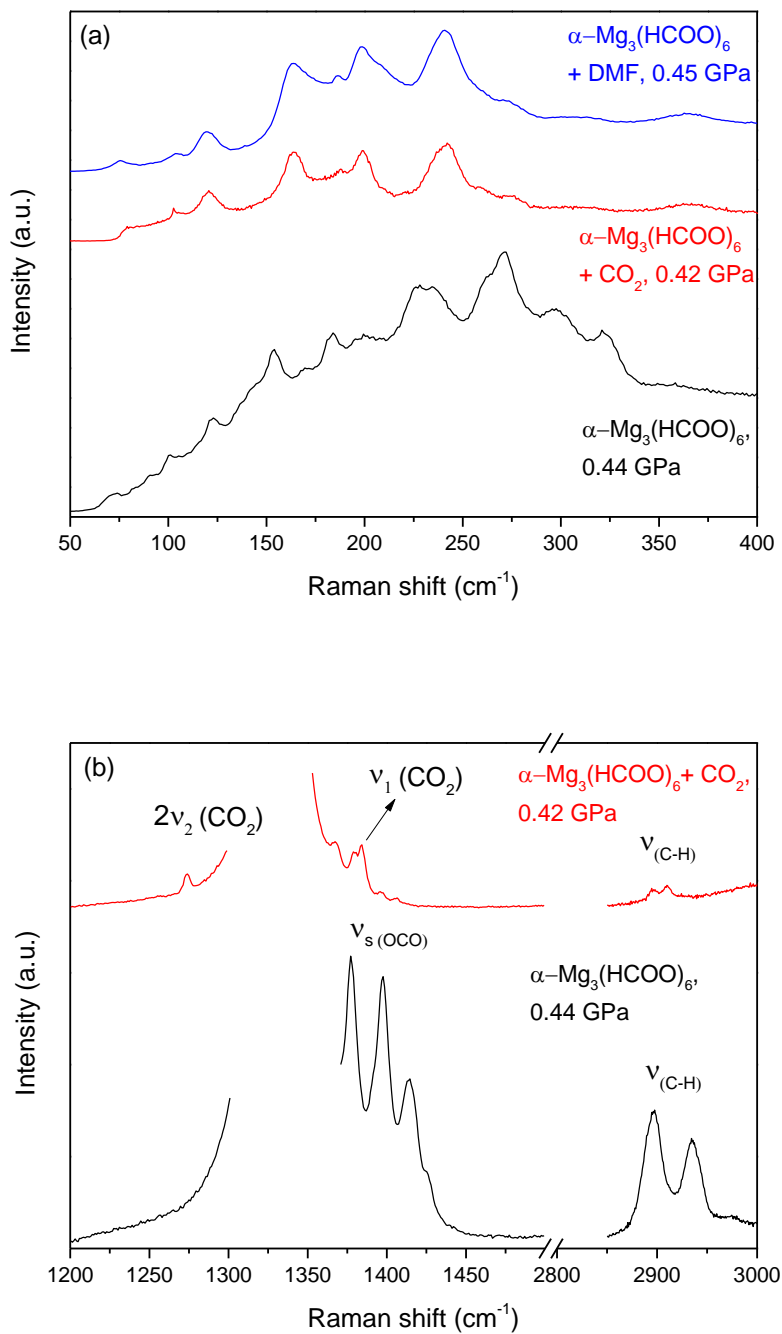
### 5.3.1 IR and Raman spectra of $\alpha$ -Mg<sub>3</sub>(HCOO)<sub>6</sub> loaded with CO<sub>2</sub>

Figure 5-2a shows the optical image of the sample chamber that consists of  $\alpha$ -Mg<sub>3</sub>(HCOO)<sub>6</sub> sample (the opaque parts) with CO<sub>2</sub> (the transparent areas). The representative IR absorption spectra of  $\alpha$ -Mg<sub>3</sub>(HCOO)<sub>6</sub> loaded with CO<sub>2</sub> and pure  $\alpha$ -Mg<sub>3</sub>(HCOO)<sub>6</sub> at similar pressure (i.e. 0.3-0.4 GPa) are shown in Figure 5-2b, with the inset that displays the zoomed spectral region of 2650 - 2950 cm<sup>-1</sup> and 3550 - 3750 cm<sup>-1</sup> of the two samples. The IR spectrum of pure  $\alpha$ -Mg<sub>3</sub>(HCOO)<sub>6</sub> at 0.33 GPa is almost identical with that of activated  $\alpha$ -Mg<sub>3</sub>(HCOO)<sub>6</sub> at ambient reported previously.<sup>23</sup> The comparison of the two spectra suggests the successful loading of CO<sub>2</sub> as evidenced by the additional peaks of the top spectrum observed. The two strong absorption bands at 670 and 2350 cm<sup>-1</sup> in the top spectrum are attributed to the bending mode ( $\nu_2$ ) and asymmetric stretching mode ( $\nu_3$ ) of CO<sub>2</sub>, respectively. Moreover, two high-frequency bands were observed at around 3600 and 3710 cm<sup>-1</sup>, which are well understood as the CO<sub>2</sub> combination modes of  $\nu_3 + 2\nu_2$  and  $\nu_3 + \nu_1$ , respectively due to the strong Fermi resonance effect.<sup>25</sup> The IR spectrum of  $\alpha$ -Mg<sub>3</sub>(HCOO)<sub>6</sub> loaded with CO<sub>2</sub> not only indicates the effective CO<sub>2</sub> loading but also provides strong evidence for guest–host interactions between the framework and CO<sub>2</sub>. Firstly, the modifications in the number and shape of  $\nu_s(\text{OCO})$  at ~1400 cm<sup>-1</sup> and  $\nu_{as}(\text{OCO})$  peaks at ~1600 cm<sup>-1</sup> strongly indicate that one of the preferential CO<sub>2</sub> adsorption sites of  $\alpha$ -Mg<sub>3</sub>(HCOO)<sub>6</sub> are located in particular regions close to the formate linkers. Secondly, a new band at around 1160 cm<sup>-1</sup> that can be assigned as the C-H in-plane bending mode ( $\delta_{(\text{C-H})}$ ) appears upon CO<sub>2</sub> loading with the framework, providing consisting information on the

interaction between CO<sub>2</sub> and the organic linker, which can be further evidenced by the enhancement of the intensity and merging of  $\nu_{(\text{C-H})}$  mode of the CO<sub>2</sub> loaded framework.



**Figure 5-2.** (a) Optical image of the sample chamber consisting of activated  $\alpha\text{-Mg}_3(\text{HCOO})_6$  loaded with CO<sub>2</sub> at 0.37 GPa and room temperature. (b) Selected mid-IR spectrum of  $\alpha\text{-Mg}_3(\text{HCOO})_6$  loaded with CO<sub>2</sub> at 0.37 GPa compared with that of the activated  $\alpha\text{-Mg}_3(\text{HCOO})_6$  at 0.33 GPa. The inset shows the enlarged parts of the two spectra in the region of 2650 – 2950 cm<sup>-1</sup> and 3550 – 3750 cm<sup>-1</sup>, respectively.



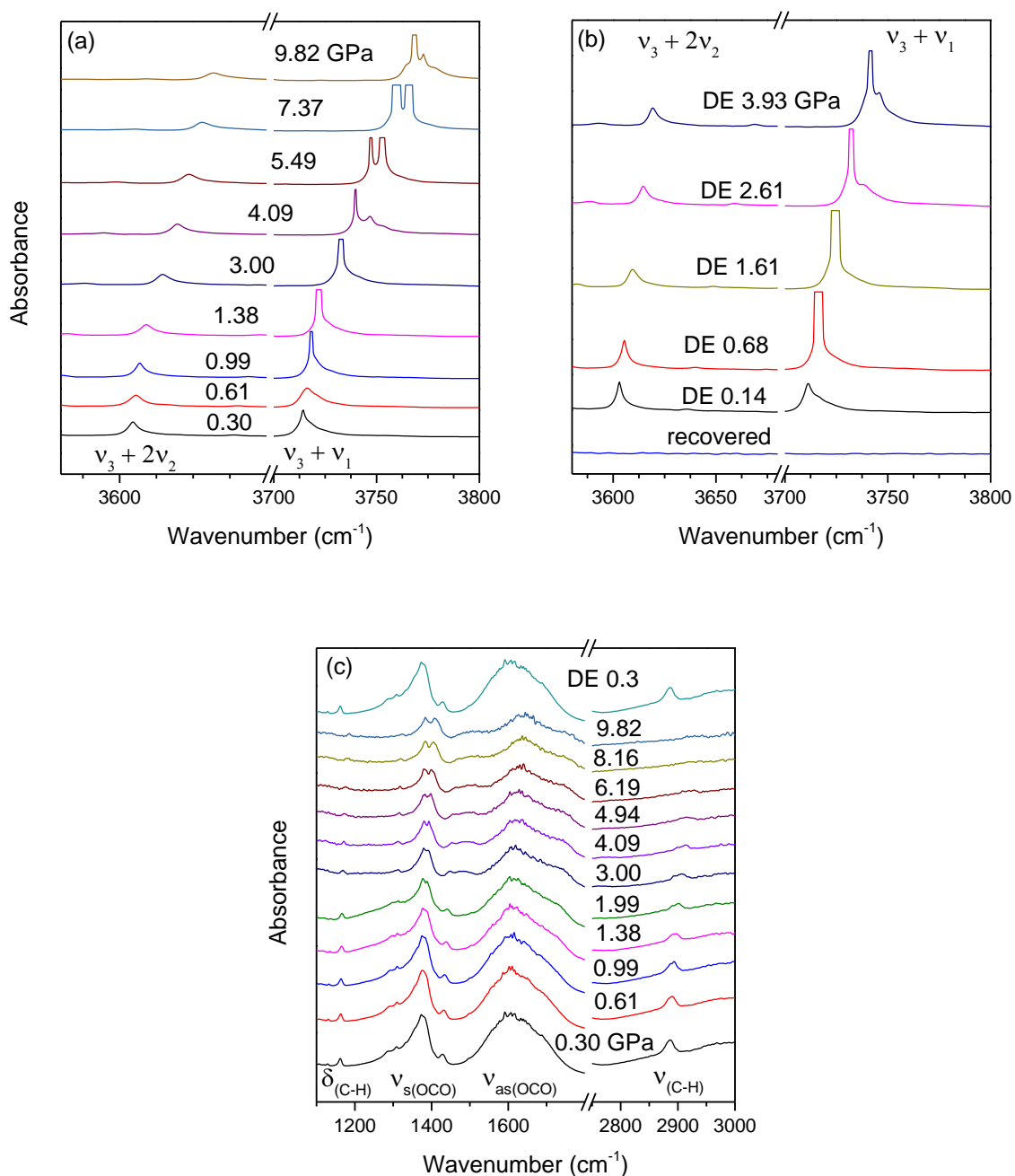
**Figure 5-3.** Selected Raman spectrum of  $\alpha\text{-Mg}_3(\text{HCOO})_6$  loaded with  $\text{CO}_2$  at 0.42 GPa compared with the empty  $\alpha\text{-Mg}_3(\text{HCOO})_6$  at 0.44 GPa and  $\alpha\text{-Mg}_3(\text{HCOO})_6$  loaded with DMF at 0.45 GPa in the spectral region 50 – 400  $\text{cm}^{-1}$  (a); Empty  $\alpha\text{-Mg}_3(\text{HCOO})_6$  at 0.44 GPa in the spectral region 1200 – 3000  $\text{cm}^{-1}$  (b).

Figure 5-3 shows the Raman spectrum of  $\alpha$ -Mg<sub>3</sub>(HCOO)<sub>6</sub> loaded with CO<sub>2</sub> compared with that of empty framework at similar pressure (i.e. 0.4 GPa). The additional peaks of the CO<sub>2</sub> loaded framework at 1273 cm<sup>-1</sup> ( $2\nu_2$  of CO<sub>2</sub>) and 1384 cm<sup>-1</sup> ( $\nu_1$  of CO<sub>2</sub>) confirmed the successful loading of CO<sub>2</sub>. From the lattice region (Figure 5-3a), it can be seen that the lattice modes of the CO<sub>2</sub> loaded samples are significantly different from the ones of pure  $\alpha$ -Mg<sub>3</sub>(HCOO)<sub>6</sub>, yet consistent with those of the DMF loaded framework.<sup>23</sup> This observation suggests that guest loading in  $\alpha$ -Mg<sub>3</sub>(HCOO)<sub>6</sub> could lead to the change of crystal structure of the framework, independent of the guest. Moreover, the significant changes in the  $\nu_s(\text{OCO})$  and  $\nu(\text{C-H})$  modes (Figure 5-3b) were also observed upon CO<sub>2</sub> loading, in accord with our observations in the IR spectra, indicating that CO<sub>2</sub> interacts with the framework in particular regions near the formate ligands.

### 5.3.2 Mid-IR spectra of $\alpha$ -Mg<sub>3</sub>(HCOO)<sub>6</sub> loaded with CO<sub>2</sub> at high pressures

In order to study the pressure effects on the performance of  $\alpha$ -Mg<sub>3</sub>(HCOO)<sub>6</sub> for CO<sub>2</sub> storage, the IR spectra of the framework loaded with CO<sub>2</sub> were measured upon compression and decompression. As mentioned in our previous work,<sup>26</sup> the CO<sub>2</sub> overtone/combination bands ( $\nu_3 + 2\nu_2$  and  $\nu_3 + \nu_1$ ) can be used to monitor the insertion of CO<sub>2</sub> into the pores of framework. It can be seen from Figure 5-4a that the  $\nu_3 + \nu_1$  mode of CO<sub>2</sub> at above 3710 cm<sup>-1</sup> becomes broadened and asymmetrical upon compression from initial loading at 0.3 GPa. At the pressure higher than 3 GPa, the  $\nu_3 + \nu_1$  mode clearly splits into a doublet, indicating two types of CO<sub>2</sub> exist in the system, with the high-frequency component representing the CO<sub>2</sub> residing outside the framework as the excessive pressure

medium, while the low-frequency component characterizing the CO<sub>2</sub> molecules inside the framework of  $\alpha$ -Mg<sub>3</sub>(HCOO)<sub>6</sub>.<sup>27</sup> Typically it is difficult to monitor the behavior of  $\nu_2$  and  $\nu_3$  modes of CO<sub>2</sub> due to their extremely intense IR absorptions. But in this case, even the combination mode  $\nu_3 + \nu_1$  of CO<sub>2</sub> is saturated, indicating that a significant amount of CO<sub>2</sub> has been trapped in the sample chamber and a large portion of CO<sub>2</sub> are inserted into the pores of  $\alpha$ -Mg<sub>3</sub>(HCOO)<sub>6</sub>. The splitting of the  $\nu_3 + \nu_1$  mode of CO<sub>2</sub> upon compression strongly suggest a pressure-enhanced CO<sub>2</sub> interaction with the framework. Continuously compressing to higher pressures (up to 9.82 GPa) resulted in the blue shift of all modes. Upon decompression, the  $\nu_3 + \nu_1$  doublet starts to merge back into a singlet below 2.61 GPa. When the pressure is completely released, the CO<sub>2</sub> has escaped from the DAC completely (Figure 5-4b). The compression–decompression cycles can be repeated several times reversibly with very little hysteresis, and the splitting of  $\nu_3 + \nu_1$  mode always occurs at 2.6–3.0 GPa. Thus the pressure behavior of CO<sub>2</sub> combination modes suggests a reversible pressure-enhanced CO<sub>2</sub> interaction with the  $\alpha$ -Mg<sub>3</sub>(HCOO)<sub>6</sub> framework.



**Figure 5-4.** Selected mid-IR spectra of  $\alpha\text{-Mg}_3(\text{HCOO})_6$  loaded with  $\text{CO}_2$  in the spectra region of 3580–3800  $\text{cm}^{-1}$  upon compression from 0.30 to 9.82 GPa (a); upon decompression to ambient (b); in the spectra region of 1100–3000  $\text{cm}^{-1}$  upon compression and as recovered to 0.37 GPa (c).

The pressure-enhanced interplay between  $\alpha\text{-Mg}_3(\text{HCOO})_6$  and  $\text{CO}_2$  are also accompanied by some structural modifications on the framework. Figure 5-4c shows the selected IR bands of the  $\alpha\text{-Mg}_3(\text{HCOO})_6$  framework loaded with  $\text{CO}_2$  upon compression together with the spectrum of the recovered sample upon decompression. All the selected IR bands, i.e. the new C-H in-plane bending mode, the OCO symmetric and asymmetric stretching modes and the C-H stretching mode experienced gradual broadening and a decrease of intensity upon compression. In particular, the  $\nu_{\text{s(OCO)}}$  mode starts to split at 4.09 GPa, implying the pressure-induced distortion of formate ligands bound to the metal and enhanced  $\text{CO}_2$  interaction with the formate ligands of the framework as pressure increases. Moreover, it is noteworthy that the change of the C-H stretching mode of the empty  $\alpha\text{-Mg}_3(\text{HCOO})_6$  framework was drastic upon initial compression and eventually disappeared below 1 GPa. In strong contrast to the sensitive pressure behavior of the empty framework, the intensity of the C-H stretching mode of the  $\text{CO}_2$  loaded framework exhibits continuous reduction with increasing pressure from 0.37 GPa to 3.00 GPa and sustains until 4.94 GPa. This observation indicates that the  $\text{CO}_2$  inclusion makes the framework more resilient to pressure, consistent with our prior study on the guest loaded  $\alpha\text{-Mg}_3(\text{HCOO})_6$  that was much more stable to external pressure than that of the activated phase. The spectrum of the recovered sample (top spectrum) resembles that of the initial sample at 0.37 GPa, suggesting that the structural modifications of the framework are reversible.

### 5.3.3 Raman and far-IR spectra of $\alpha\text{-Mg}_3(\text{HCOO})_6$ loaded with $\text{CO}_2$ at high pressures

Supplementary to the mid-IR spectra that are sensitive to the local structural changes of the organic linker upon compression, the Raman and far-IR spectra of the  $\text{CO}_2$

loaded  $\alpha$ -Mg<sub>3</sub>(HCOO)<sub>6</sub> provide additional information on the changes in the lattice region of the framework and the metal-ligand bonding at high pressures. Figure 5-5 shows the Raman and far-IR spectra of  $\alpha$ -Mg<sub>3</sub>(HCOO)<sub>6</sub> loaded with CO<sub>2</sub> upon compression and decompression. The Raman peaks in the region 100-400 cm<sup>-1</sup> are associated with the lattice modes of the  $\alpha$ -Mg<sub>3</sub>(HCOO)<sub>6</sub> framework, whereas the peak of the lowest frequency (80 cm<sup>-1</sup> at 0.69 GPa) is attributed to the external mode (E<sub>g</sub>) of crystalline CO<sub>2</sub> outside the framework (Figure 5-5a).<sup>28</sup> Upon compression from 0.69 GPa to 4.46 GPa, the E<sub>g</sub> mode of CO<sub>2</sub> increases intensively, while the lattice modes of the framework become much broadened. The changes indicate the sample consists of highly crystalline solid CO<sub>2</sub> outside the framework and a reduced crystallinity of the  $\alpha$ -Mg<sub>3</sub>(HCOO)<sub>6</sub> framework in such a pressure region. Upon further compression from 6.4 GPa to 11.41 GPa, the Raman profile in the lattice region are dominated by three external modes of crystalline CO<sub>2</sub> (phase I), which are the E<sub>g</sub>, F<sub>g-</sub> and F<sub>g+</sub> mode (at 115, 145, 216 cm<sup>-1</sup> respectively, shown in Figure 5-5a).<sup>28</sup> The disappearance of the lattice modes of the framework indicates the transition from a crystalline to an amorphous phase for  $\alpha$ -Mg<sub>3</sub>(HCOO)<sub>6</sub> above 4.46 GPa. Upon decompression, the changes of the Raman peaks are found to be reversible. When the pressure is completely released, the spectrum of the recovered sample resembles that of the CO<sub>2</sub> loaded framework at 0.69 GPa except for the disappearance of the CO<sub>2</sub> external mode. Thus the amorphization of the  $\alpha$ -Mg<sub>3</sub>(HCOO)<sub>6</sub> framework loaded with CO<sub>2</sub> above 4.5 GPa is reversible.

The changes of the far-IR spectra (Figure 5-5b) are consistent with those of Raman spectra of the  $\alpha$ -Mg<sub>3</sub>(HCOO)<sub>6</sub> framework loaded with CO<sub>2</sub> upon compression. The IR band at around 413 cm<sup>-1</sup> at 0.69 GPa is due to Mg-O stretching and the bands below 400 cm<sup>-1</sup>



are attributed to the lattice modes of the  $\alpha$ -Mg<sub>3</sub>(HCOO)<sub>6</sub> framework. No IR bands associated with solid CO<sub>2</sub> are observed in the far-IR region, due to the weak IR absorption of solid CO<sub>2</sub>.<sup>29</sup> The disappearance of the Mg-O stretching mode and the external modes of the framework above 4.46 GPa suggests the amorphization for the CO<sub>2</sub> loaded framework. The spectrum of the recovered sample (top spectrum), when the CO<sub>2</sub> completely escape the sample chamber, is almost identical with that of CO<sub>2</sub> loaded framework at 0.69 GPa except for the frequency shifts. This observation strongly suggests that CO<sub>2</sub> does not interact with the metal center of the  $\alpha$ -Mg<sub>3</sub>(HCOO)<sub>6</sub> framework.

The combined Raman and far-IR data suggest that the CO<sub>2</sub> loaded  $\alpha$ -Mg<sub>3</sub>(HCOO)<sub>6</sub> framework undergoes a reversible crystalline-to-amorphous phase transition at around 4.5 GPa. Thus the connectivity of the pores remains intact in the amorphous phase at high pressures. The pressure behavior of the framework loaded with CO<sub>2</sub> is similar to those of benzene or DMF loaded framework which has no phase transition within 4 GPa, consistent with the fact that the framework containing guest molecules is more stable to external pressure than that of the empty framework.

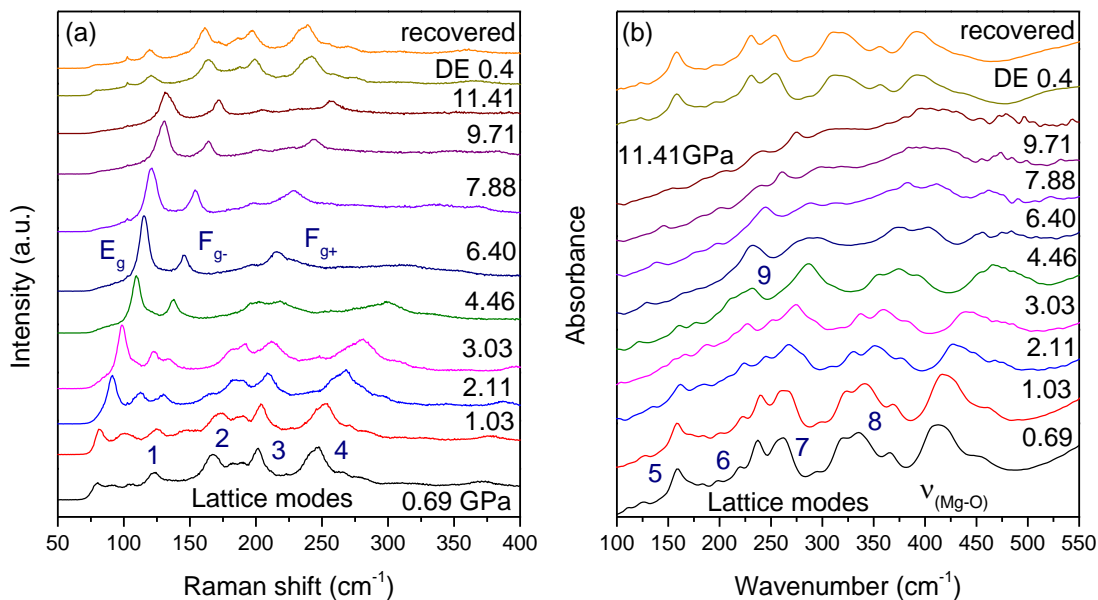


**Figure 5-5.** (a) Selected Raman spectra of  $\alpha\text{-Mg}_3(\text{HCOO})_6$  loaded with  $\text{CO}_2$  in the spectra region of 50 – 400  $\text{cm}^{-1}$  upon compression from 0.69 to 11.41 GPa and as recovered to 0.40 GPa and ambient pressure. (b) Selected far-IR spectra of  $\alpha\text{-Mg}_3(\text{HCOO})_6$  loaded with  $\text{CO}_2$  in the spectra region of 100 – 550  $\text{cm}^{-1}$  upon compression from 0.69 to 11.41 GPa and as recovered to 0.40 GPa and ambient pressure.

## 5.4 Discussion

In order to examine the stability and phase transformation of the CO<sub>2</sub> loaded  $\alpha$ -Mg<sub>3</sub>(HCOO)<sub>6</sub> on compression in great details, we monitored the IR frequencies and Raman shifts as a function of pressure as shown in Figures 5-6. The pressure coefficients ( $dv/dP$  ( $\text{cm}^{-1}\cdot\text{GPa}^{-1}$ )) of the IR and Raman modes were calculated by linear regression of the experimental data and listed in Tables 5-1 and 5-2, respectively. Generally all the IR and Raman modes exhibit regular pressure-induced blue shifts, consistent with that the bonds become stiffened upon compression. For mid-IR measurements of the framework loaded with CO<sub>2</sub>, both the  $\delta_{(\text{C-H})}$  and  $\nu_{(\text{C-H})}$  mode vanish above 4.09 GPa (Figure 5-6a). Moreover, the disappearance of the lattice modes of  $\alpha$ -Mg<sub>3</sub>(HCOO)<sub>6</sub> (denoted as 1-8 in Figures 5-6b and 5-6c) beyond 4.46 GPa provides clear evidence for the amorphization of the framework. The approximate phase transition boundary for the CO<sub>2</sub> loaded  $\alpha$ -Mg<sub>3</sub>(HCOO)<sub>6</sub> is thus around 4.50 GPa, as indicated in Figures 5-6.

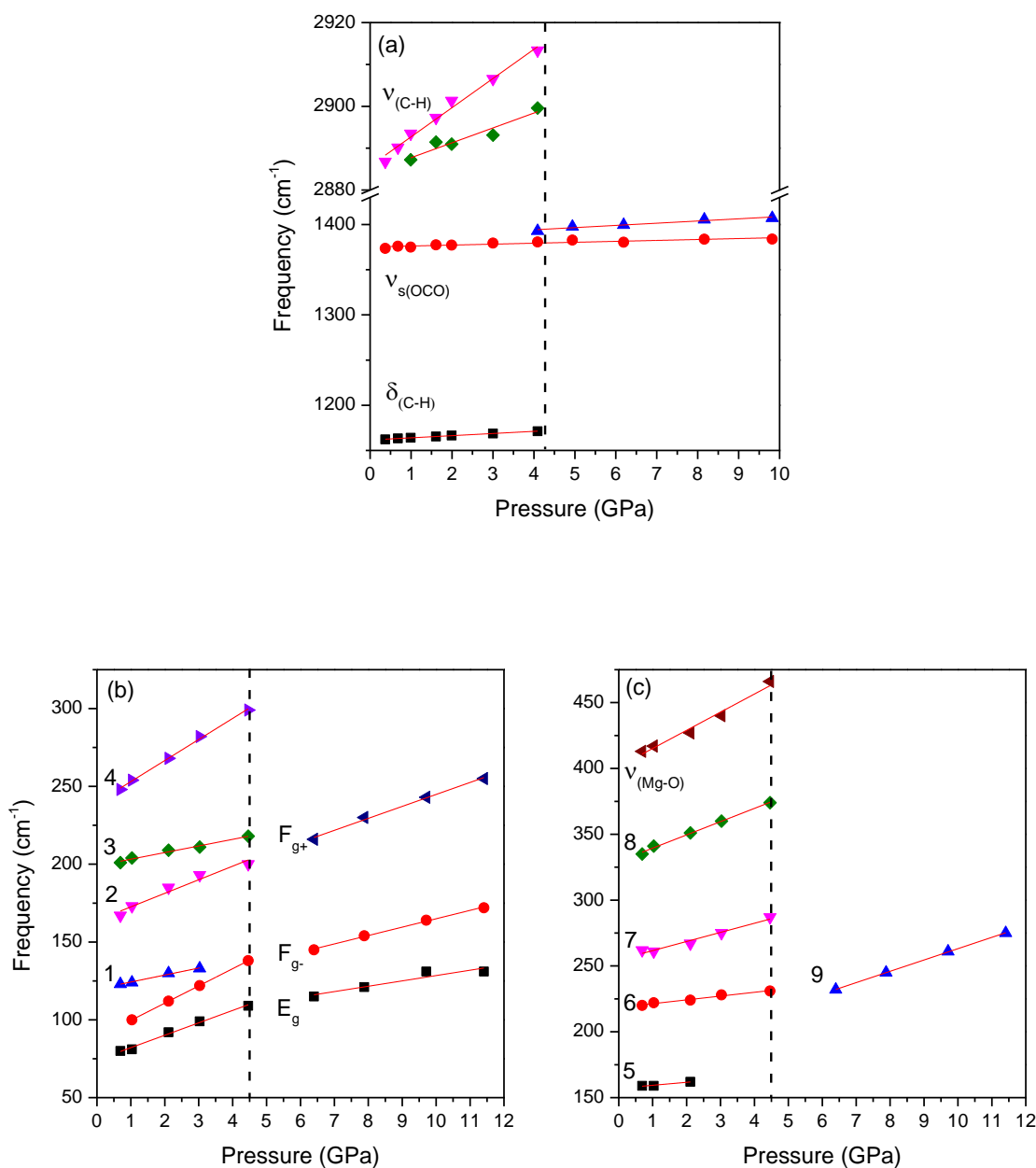


**Figure 5-6.** (a) IR frequencies of  $\nu_{(C-H)}$ ,  $\nu_{s(OCO)}$  and  $\delta_{(C-H)}$  mode of CO<sub>2</sub> loaded  $\alpha$ -Mg<sub>3</sub>(HCOO)<sub>6</sub> as a function of pressure; (b) Raman shifts of the lattice modes (denoted as 1- 4) of CO<sub>2</sub> loaded  $\alpha$ -Mg<sub>3</sub>(HCOO)<sub>6</sub> and the lattice modes (F<sub>g+</sub>, F<sub>g-</sub> and E<sub>g</sub>) of solid CO<sub>2</sub> as a function of pressure; (c) IR frequencies of  $\nu_{(Mg-O)}$  and the lattice modes (denoted as 5- 9) of CO<sub>2</sub> loaded  $\alpha$ -Mg<sub>3</sub>(HCOO)<sub>6</sub> as a function of pressure.

**Table 5-1.** Pressure dependences [ $dv/dP$  ( $\text{cm}^{-1}\cdot\text{GPa}^{-1}$ )] of the selected IR bands of  $\alpha$ - $\text{Mg}_3(\text{HCOO})_6$  loaded with  $\text{CO}_2$  on compression

IR mode	Frequency ( $\text{cm}^{-1}$ )	$dv/dP$ ( $\text{cm}^{-1}\cdot\text{GPa}^{-1}$ )	
		0-4.5 GPa	4.5-11 GPa
$\nu_{(\text{CH})}$	2886	7.0	
	2887	3.6	
$\nu_{\text{s}(\text{OCO})}$	1388		2.4
	1374	1.0	
$\delta_{(\text{CH})}$	1162	2.4	
$\nu_{(\text{Mg-O})}$	413	13.8	
8	335	10.0	
7	262	6.9	
6	220	2.9	
9	232		8.6
5	159	2.3	

**Table 5-2.** Pressure dependences [ $dv/dP$  ( $\text{cm}^{-1}\cdot\text{GPa}^{-1}$ )] of the selected Raman bands of  $\alpha$ - $\text{Mg}_3(\text{HCOO})_6$  loaded with  $\text{CO}_2$  on compression

Raman mode	Frequency ( $\text{cm}^{-1}$ )	$dv/dP$ ( $\text{cm}^{-1}\cdot\text{GPa}^{-1}$ )	
		0-4.5 GPa	4.5-11 GPa
4	248	13.5	
3	201	4.2	
2	167	8.7	
1	123	4.5	
$F_{g+}$	216		7.7
$F_{g-}$	100	11.0	5.4
$E_g$	80	8.0	3.4

Our results demonstrate an enhanced stability of  $\alpha$ -Mg<sub>3</sub>(HCOO)<sub>6</sub> framework to external high pressure due to the space-filling of the guest CO<sub>2</sub>. Below 4 GPa, the CO<sub>2</sub> loaded framework experiences no phase change whereas the empty framework undergoes an irreversible phase transformation at 2 GPa. Similar pressure behavior were observed for the DMF/benzene loaded framework, which further demonstrates the general trend that guest molecules can significantly enhance framework resistance to external stress, independent of the guest molecules loaded. In addition, the higher stability of the CO<sub>2</sub> loaded framework is further evidenced by the pressure behavior of the internal mode  $\nu_{s(\text{OCO})}$  from mid-IR spectra. The pressure dependence of the  $\nu_{s(\text{OCO})}$  mode of the CO<sub>2</sub> loaded framework (i.e. 1.0 cm<sup>-1</sup>·GPa<sup>-1</sup>) is much lower compared with its counterparts of the empty framework (i.e. 13.1 cm<sup>-1</sup>·GPa<sup>-1</sup>),<sup>23</sup> indicating that the formate ligands that bound to the metal are much less distorted with the existence of CO<sub>2</sub> inside the framework. Thus the rigidity of the entire framework is substantially enhanced upon CO<sub>2</sub> loading.

The compression-decompression cycles on CO<sub>2</sub> loaded  $\alpha$ -Mg<sub>3</sub>(HCOO)<sub>6</sub> reveal an reversible pressure-enhanced interactions between CO<sub>2</sub> and the framework. As a promising candidate for CO<sub>2</sub> storage material, the performance of MOFs for CO<sub>2</sub> adsorption has been widely studied. However, the study of the enhanced guest-host interactions between the surrounding CO<sub>2</sub> and the MOF framework or other nano-porous materials (e.g. zeolites) are sparse.<sup>26,27,30</sup> Previous studies have shown that the nature of the interactions between CO<sub>2</sub> and the framework as well as the migration mechanism are mainly dependent on the porosity, the flexibility and the existence of the preferential adsorption sites of the host framework. The above factors that influence the performance of  $\alpha$ -Mg<sub>3</sub>(HCOO)<sub>6</sub> for CO<sub>2</sub> storage will be discussed in details as follows.

Firstly, the porosity of the host framework especially the pore size has a significant impact on the threshold conditions of CO<sub>2</sub> inclusion into the framework. For example, Lee *et al.*<sup>30</sup> demonstrated that only under pressure (1.5 GPa) and elevated temperatures (110 °C) CO<sub>2</sub> can be inserted into the natrolite in which the pore size is just slightly bigger than the kinetic diameter of gaseous CO<sub>2</sub> (3.3 Å). The  $\alpha$ -Mg<sub>3</sub>(HCOO)<sub>6</sub> has a pore diameter around 5 Å, which provides enough space for guest molecules CO<sub>2</sub> to fit inside the channels. Thus CO<sub>2</sub> can be adsorbed into the  $\alpha$ -Mg<sub>3</sub>(HCOO)<sub>6</sub> framework upon initial loading at low pressures (i.e., < 0.6 GPa when CO<sub>2</sub> is in fluid phase) under room temperature.

Secondly, the flexibility of the organic ligand plays an important role in the mechanism and performance of CO<sub>2</sub> adsorption in MOFs. Earlier work on ZIF-8 revealed a so-called “gate opening” effect, under which the imidazolate ligands can be reoriented in response to adsorption as well as external pressure to increase the accessible pore volume, facilitating the CO<sub>2</sub> diffusion and adsorption in the framework.<sup>26,31,32</sup> Therefore, ZIF-8 exhibits excellent performance for CO<sub>2</sub> adsorption, with the maximum CO<sub>2</sub> uptake of 4.3 wt% at 298K and ambient pressure, despite its small pore size (3.4 Å).<sup>33</sup> In contrast, the CO<sub>2</sub> adsorption capacity of  $\alpha$ -Mg<sub>3</sub>(HCOO)<sub>6</sub> at ambient pressure (1.32 wt%)<sup>34</sup> is substantially lower than that of ZIF-8, not only owing to the lesser porosity, but also because of the rigidity of organic ligands of the framework. Our previous work showed that the response of  $\alpha$ -Mg<sub>3</sub>(HCOO)<sub>6</sub> framework to compression was initiated by the small distortion of the individual Mg<sub>2</sub>-O and Mg<sub>4</sub>-O clusters, in contrast to the twist of the organic linker of ZIF-8. This argument is further evidenced by the pressure behavior of the Mg-O bond monitored by far-IR measurements in this work. Our results show that the



pressure dependence of Mg-O stretch mode ( $13.8 \text{ cm}^{-1}/\text{GPa}$ ) is substantially higher than those of the other modes from the formate ligand (such as  $\nu_{\text{s(OCO)}}$  and  $\nu_{\text{(CH)}}$ ), indicating that the compression on the framework is mainly mediated through the Mg-O bonds. Thus the rigidity of the organic ligands make  $\alpha\text{-Mg}_3(\text{HCOO})_6$  less favorable for  $\text{CO}_2$  adsorption compared with ZIF-8.

Lastly, the existence of preferential adsorption site of MOFs can substantially affect their performance for  $\text{CO}_2$  adsorption. A typical example is Mg-MOF-74<sup>21</sup>, an efficient  $\text{CO}_2$  capture media due to the strong affinity between its open metal sites and  $\text{CO}_2$ . Our prior studies of MIL-68 (In) showed an outstanding performance for  $\text{CO}_2$  adsorption not only because of the large pore size of the framework, but also due to the presence of the preferential adsorption site OH units, which interact strongly with  $\text{CO}_2$  through hydrogen bonding. In this work, unlike Mg-MOF-74, the Mg metal center of  $\alpha\text{-Mg}_3(\text{HCOO})_6$  has no interaction with  $\text{CO}_2$  as it is stably coordinated with six oxygens from the organic ligands. The almost identical IR profiles of the  $\text{CO}_2$  loaded framework and the empty one from the far-IR measurements suggested that the Mg-O bonds are not affected upon  $\text{CO}_2$  adsorption. Nonetheless, strong interactions between  $\text{CO}_2$  and the formate ligand of  $\alpha\text{-Mg}_3(\text{HCOO})_6$  were observed from the pressure behavior of  $\nu_3 + \nu_1$  mode of  $\text{CO}_2$ . The splitting of the  $\nu_3 + \nu_1$  mode of  $\text{CO}_2$  loaded  $\alpha\text{-Mg}_3(\text{HCOO})_6$ , which suggests two types of  $\text{CO}_2$  present in the system, is distinctively different from what we observed in ZIF-8 or MIL-68 (In). The  $\text{CO}_2$  adsorbed in ZIF-8 or MIL-68 (In), which exhibited a broad  $\nu_3 + \nu_1$  IR band with a lower frequency, is characteristic of fluid-like  $\text{CO}_2$ , in strong contrast to the solid  $\text{CO}_2$  outside the framework which displayed a sharp peak with a higher frequency. However in this case, the  $\text{CO}_2$  included in  $\alpha\text{-Mg}_3(\text{HCOO})_6$  framework under high pressures showed a solid-like

feature (sharp peak), which indicates a more localized CO<sub>2</sub> inside the pores. The localization or reduced mobility of CO<sub>2</sub> in the  $\alpha$ -Mg<sub>3</sub>(HCOO)<sub>6</sub> framework is highly likely due to the strong dipole-dipole interaction between the oxygen of CO<sub>2</sub> and the carbon of the formate ligand, as illustrated in Figure 5-7. Previous studies demonstrated similar yet weaker van der Waals interactions between CO<sub>2</sub> and the framework at gas adsorption pressures.<sup>35</sup> Under much high pressures, the mobility of CO<sub>2</sub> in the pores of  $\alpha$ -Mg<sub>3</sub>(HCOO)<sub>6</sub> is highly restricted, resulting from a stronger guest-host interaction induced by external pressure. Based on the sharp feature of the  $\nu_3 + \nu_1$  mode, CO<sub>2</sub> molecules were believed to be aligned and in high order within the pores of  $\alpha$ -Mg<sub>3</sub>(HCOO)<sub>6</sub>.

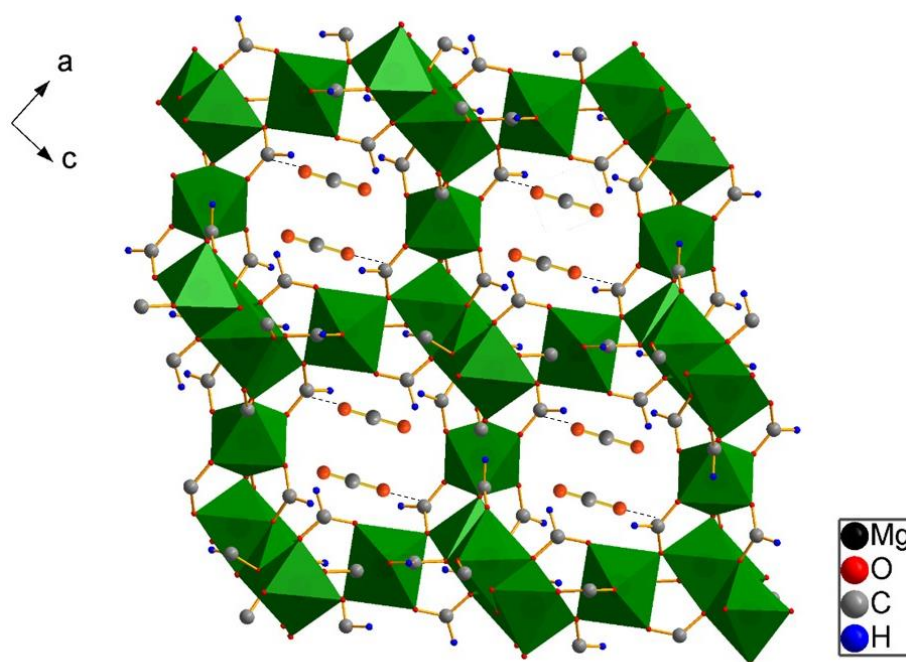


**Figure 5-7.** Illustration of CO<sub>2</sub> adsorption in  $\alpha$ -Mg<sub>3</sub>(HCOO)<sub>6</sub>. The grey & red ball-stick models represent the CO<sub>2</sub> molecules adsorbed inside the pores of the framework. The dash lines symbolise the dipole-dipole interaction between CO<sub>2</sub> and the formate ligands.

## 5.5 Conclusions

In summary, *in situ* IR and Raman spectroscopic measurements of  $\alpha$ -Mg<sub>3</sub>(HCOO)<sub>6</sub> loaded with CO<sub>2</sub> were investigated under external high pressure up to 11 GPa. We demonstrate a strong guest-host interplay between CO<sub>2</sub> and the formate ligand via dipole-dipole interaction, while the Mg metal center has no interactions with CO<sub>2</sub>. The CO<sub>2</sub> molecules are highly confined inside the pores due to the strong interaction with the framework at high pressures. Moreover, the CO<sub>2</sub> loaded  $\alpha$ -Mg<sub>3</sub>(HCOO)<sub>6</sub> framework undergoes a reversible crystalline-to-amorphous phase transformation at around 4.5 GPa, in contrast to the pressure behavior of the empty framework that experience an irreversible crystal-to-crystal phase transition at 2 GPa. The chemical connectivity was intact in the amorphous phase that maintained the porosity for CO<sub>2</sub> storage at high pressures. Our observations further demonstrate that guest molecules can significantly enhance the stability of the host framework to external pressure. Overall, the chemical and mechanical robustness of the framework with the presence of preferential CO<sub>2</sub> adsorption site makes  $\alpha$ -Mg<sub>3</sub>(HCOO)<sub>6</sub> an interesting and promising candidate for CO<sub>2</sub> storage at high pressure conditions.

## 5.6 Reference

- (1) Rowsell, J. L. C.; Yaghi, O. M. *Microporous and Mesoporous Materials* **2004**, *73*, 3.
- (2) Furukawa, H.; Cordova, K. E.; O’Keeffe, M.; Yaghi, O. M. *Science* **2013**, *341*, 1230444.
- (3) Li, B.; Wen, H.-M.; Zhou, W.; Chen, B. *The Journal of Physical Chemistry Letters* **2014**, *5*, 3468.
- (4) Van de Voorde, B.; Bueken, B.; Denayer, J.; De Vos, D. *Chemical Society Reviews* **2014**, *43*, 5766.

- (5) He, Y.; Zhou, W.; Qian, G.; Chen, B. *Chemical Society Reviews* **2014**, *43*, 5657.
- (6) Barea, E.; Montoro, C.; Navarro, J. A. R. *Chemical Society Reviews* **2014**, *43*, 5419.
- (7) Sumida, K.; Rogow, D. L.; Mason, J. A.; McDonald, T. M.; Bloch, E. D.; Herm, Z. R.; Bae, T. H.; Long, J. R. *Chemical Reviews* **2012**, *112*, 724.
- (8) Dhakshinamoorthy, A.; Garcia, H. *Chemical Society Reviews* **2014**, *43*, 5750.
- (9) Zhang, T.; Lin, W. *Chemical Society Reviews* **2014**, *43*, 5982.
- (10) Liu, J.; Chen, L.; Cui, H.; Zhang, J.; Zhang, L.; Su, C.-Y. *Chemical Society Reviews* **2014**, *43*, 6011.
- (11) Gascon, J.; Corma, A.; Kapteijn, F.; Llabrés i Xamena, F. X. *ACS Catalysis* **2014**, *4*, 361.
- (12) Ranocchiari, M.; Bokhoven, J. A. v. *Physical Chemistry Chemical Physics* **2011**, *13*, 6388.
- (13) Della Rocca, J.; Liu, D.; Lin, W. *Accounts of Chemical Research* **2011**, *44*, 957.
- (14) McKinlay, A. C.; Morris, R. E.; Horcajada, P.; Férey, G.; Gref, R.; Couvreur, P.; Serre, C. *Angewandte Chemie International Edition* **2010**, *49*, 6260.
- (15) Rodrigues, M. O.; de Paula, M. V.; Wanderley, K. A.; Vasconcelos, I. B.; Alves, S.; Soares, T. A. *International Journal of Quantum Chemistry* **2012**, *112*, 3346.
- (16) Kreno, L. E.; Leong, K.; Farha, O. K.; Allendorf, M.; Van Duyne, R. P.; Hupp, J. T. *Chemical Reviews* **2012**, *112*, 1105.
- (17) Hu, Z.; Deibert, B. J.; Li, J. *Chemical Society Reviews* **2014**, *43*, 5815.
- (18) Ramaswamy, P.; Wong, N. E.; Shimizu, G. K. H. *Chemical Society Reviews* **2014**, *43*, 5913.
- (19) Xu, J.; Terskikh, V. V.; Huang, Y. *Chemistry – A European Journal* **2013**, *19*, 4432.
- (20) Mallick, A.; Saha, S.; Pachfule, P.; Roy, S.; Banerjee, R. *Inorganic Chemistry* **2011**, *50*, 1392.
- (21) Britt, D.; Furukawa, H.; Wang, B.; Glover, T. G.; Yaghi, O. M. *Proceedings of the National Academy of Sciences* **2009**, *106*, 20637.
- (22) Rood, J. A.; Noll, B. C.; Henderson, K. W. *Inorganic Chemistry* **2006**, *45*, 5521.
- (23) Mao, H.; Xu, J.; Hu, Y.; Huang, Y.; Song, Y. *Journal of Materials Chemistry A* **2015**, *3*, 11976.
- (24) Mao, H. K.; Xu, J.; Bell, P. M. *Journal of Geophysical Research: Solid Earth* **1986**, *91*, 4673.
- (25) Hanson, R. C.; Jones, L. H. *The Journal of Chemical Physics* **1981**, *75*, 1102.

- (26) Hu, Y.; Liu, Z.; Xu, J.; Huang, Y.; Song, Y. *Journal of the American Chemical Society* **2013**, *135*, 9287.
- (27) Santoro, M.; Gorelli, F.; Haines, J.; Cambon, O.; Levelut, C.; Garbarino, G. *Proceedings of the National Academy of Sciences* **2011**, *108*, 7689.
- (28) Olijnyk, H.; Däüfer, H.; Jodl, H. J.; Hochheimer, H. D. *The Journal of Chemical Physics* **1988**, *88*, 4204.
- (29) Aoki, K.; Yamawaki, H.; Sakashita, M. *Phys Rev B* **1993**, *48*, 9231.
- (30) Lee, Y.; Liu, D.; Seoung, D.; Liu, Z. X.; Kao, C. C.; Vogt, T. *Journal of the American Chemical Society* **2011**, *133*, 1674.
- (31) Fairen-Jimenez, D.; Moggach, S. A.; Wharmby, M. T.; Wright, P. A.; Parsons, S.; Duren, T. *Journal of the American Chemical Society* **2011**, *133*, 8900.
- (32) Moggach, S. A.; Bennett, T. D.; Cheetham, A. K. *Angewandte Chemie International Edition* **2009**, *48*, 7087.
- (33) Low, J. J.; Benin, A. I.; Jakubczak, P.; Abrahamian, J. F.; Faheem, S. A.; Willis, R. R. *Journal of the American Chemical Society* **2009**, *131*, 15834.
- (34) Rossin, A.; Ienco, A.; Costantino, F.; Montini, T.; Di Credico, B.; Caporali, M.; Gonsalvi, L.; Fornasiero, P.; Peruzzini, M. *Crystal Growth & Design* **2008**, *8*, 3302.
- (35) Fischer, M.; Hoffmann, F.; Fröba, M. *ChemPhysChem* **2010**, *11*, 2220.

## Chapter 6

# 6 Exploring the Remarkable Affinity of MOF CaSDB towards CO<sub>2</sub> at Extreme Pressure

## 6.1 Introduction

Porous crystalline metal–organic frameworks (MOFs) have attracted intensive research attention in recent years because of their intriguing structures, exceptional porosities and a wide range of potential applications, including gas storage & separation, catalysis, biomedical drug delivery and so on.<sup>1-3</sup> Among these applications, the investigation of using MOFs as storage media to efficiently trap greenhouse gas such as carbon dioxide for clean energy uses is one of the mostly studied fields.<sup>4-6</sup> Plentiful MOFs with various structures have been examined for their performances of CO<sub>2</sub> capture and storage.<sup>7-10</sup> Within the large varieties of the MOFs capable of gas sorption, the alkaline earth MOFs especially the calcium MOFs have been less studied compared with transition or lanthanide metal-based MOFs. Considering the natural abundance, non-toxicity, low-cost as well as the role of calcium in natural CO<sub>2</sub> separation and storage,<sup>11</sup> the synthesis of calcium based MOFs is of particular interest.

Recently, a highly robust microporous calcium based MOF named CaSDB (SDB = 4,4'-sulfonyldibenzoate) was successfully synthesized and showed high CO<sub>2</sub>/N<sub>2</sub> selectivity.<sup>12,13</sup> The CaSDB framework is a three-dimensional network, composed of corner-sharing calcium polyhedral chains along the crystallographic [010] direction. The calcium ion is octahedrally coordinated to five-carboxylate groups and one sulfonyl oxygen atom. One of the sulfonyl oxygen atoms of the linker is uncoordinated (Figure 6-1a). Each of the calcium polyhedral chains is connected with six other such chains in the [100] and

[001] directions through vertex sharing. Such a connectivity leads to the formation of diamond-shaped channels along the [010] direction with an average size  $5.9 \text{ \AA} \times 5.8 \text{ \AA}$  (Figure 6-1b). Disordered water molecules are present within the channel, which can be readily removed upon activation by heating to 563 K in vacuum. Remarkably, the activated CaSDB framework does not reabsorb water when exposed to air.

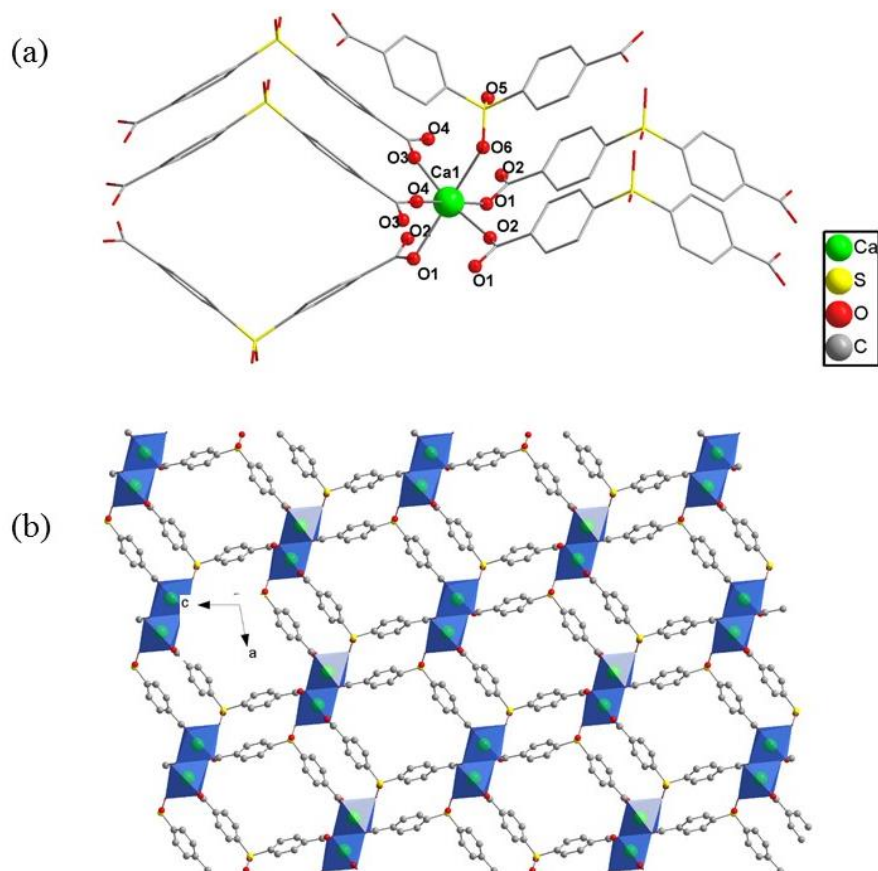


**Figure 6-1.** (a) Local structure and Calcium coordination environment of CaSDB; (b) View of the structure of activated CaSDB along *b* axis, showing the diamond-shaped channels with the size of  $\sim 5.5 \text{ \AA}$  in diameter.

For the performance of CO<sub>2</sub> storage, CaSDB shows a reversible uptake of CO<sub>2</sub> of 4.37 wt% at 298 K, 1 bar; with a high CO<sub>2</sub>/N<sub>2</sub> selectivity. The specific CO<sub>2</sub> adsorption sites at the framework has been explored by Plonka *et al.*, who observed that CO<sub>2</sub> molecules adopt two positions approximately in the middle of the channel through the interaction between the delocalized  $\pi$  aromatic system of both phenyl rings of the organic linker and the molecular quadrupole of CO<sub>2</sub> via single crystal data.<sup>14</sup> The CO<sub>2</sub> – phenyl ring interactions at low pressures ( $\leq 1$  bar) in an alkaline-metal-containing MOFs is novel and encouraging in the search for alternative mechanisms for CO<sub>2</sub> adsorption under higher pressures, as the application of MOFs as a gas storage media sometimes requires extreme loading pressures that is far beyond ambient pressure. So far no study has addressed the CO<sub>2</sub> storage in CaSDB and guest-host interactions at high pressures in the gigapascal scale, despite the adsorption studies at low pressures mentioned above. Application of high external pressure on the framework may significantly change the framework topology,<sup>15-25</sup> the pore size opening and thus the adsorption properties.<sup>26-33</sup> Thus the stability of the framework is pivotal to its gas storage performance. Besides, the storage capacity can be substantially enhanced as more CO<sub>2</sub> could be inserted into the framework at high pressures.

In this study, the stability of CaSDB framework and the enhanced CO<sub>2</sub> adsorptive performance under high pressures were examined by IR and Raman spectroscopy, which allows the understanding of local structures, chemical bonding, and thus the nature of host–guest interactions between the adsorbed molecules and the framework. We demonstrated a high stability of activated CaSDB on compression and a remarkable affinity of the framework towards CO<sub>2</sub> at high pressures. In addition to the single CO<sub>2</sub> adsorption



site observed at ambient pressure, new CO<sub>2</sub> interaction sites were found at elevated pressure, suggesting a pressure-enhanced CO<sub>2</sub> storage in CaSDB.

## 6.2 Experimental section

The CaSDB sample was synthesized according to the literature.<sup>12</sup> The detailed procedure is as follows: a mixture of 4,4'-sulfonyldibenzoate acid (H<sub>2</sub>SDB, 0.1224 g, 0.4 mmol), Ca(NO<sub>3</sub>)<sub>2</sub> · 4H<sub>2</sub>O (0.1890 g, 0.8 mmol), ethanol (9.0 ml) and H<sub>2</sub>O (1.0 ml) was stirred for 10 min in air. Then the mixture was placed in a 100 ml Teflon autoclave and heated at 150 °C for 20 minutes. The autoclave was cooled to room temperature, washed with fresh ethanol and colorless crystals were collected (0.1077 g, 74.3% yield based on the H<sub>2</sub>SDB reagent). The as-synthesized sample was then activated in a vacuum gas manifold at 563 K to remove the solvent molecules inside the channels of the framework. The crystallinity of the activated sample was checked by XRD.

To achieve high pressure, diamond anvil cells (DAC) equipped with type II and I diamonds with culet size of 600 μm were used for IR and Raman measurements, respectively. Stainless steel gaskets were predrilled with a hole of 200 μm as the sample chamber. The samples with 30 μm in thickness were loaded into the gasket along with a few ruby chips as the pressure calibrant. To study CO<sub>2</sub> storage in CaSDB under high pressures, the activated CaSDB powder samples were firstly loaded into the DAC which was cooled in a cryogenic bath of liquid nitrogen. Gaseous CO<sub>2</sub> was then introduced into the sample chamber when the temperature was below the melting point of dry ice (i.e., < -78 °C) before the DAC was sealed with minimal possible pressure (~ 0.5 GPa). After the

DAC was brought to room temperature, the internal pressure was measured by analyzing the shift in the R1 emission line of the included ruby chips.<sup>34</sup> Customized IR and Raman micro-spectroscopic system with details described in *Chapter 1* were used for all mid-IR absorption and Raman measurements.<sup>35,36</sup> Far-infrared measurements were performed at the U2A beamline at the National Synchrotron Light Source (NSLS), Brookhaven National Laboratory (BNL). All measurements were performed under room temperature and multiple runs were carried out for reproducibility.

## 6.3 Results

### 6.3.1 IR and Raman spectra of activated CaSDB at ambient pressure

The IR and Raman spectra of activated CaSDB at ambient conditions are depicted in Figure 6-2 from 100 to 3400  $\text{cm}^{-1}$  and with the spectral assignments listed. Our mid-IR and Raman measurements of CaSDB are in good agreement with those of previously studied;<sup>14</sup> while the far-IR spectrum, which is unique to the bonding between the metal center and organic ligands, is reported for the first time. In the IR spectrum (bottom spectrum of Figure 6-2), the IR bands from 100 to 300  $\text{cm}^{-1}$  are assigned to the lattice modes of the CaSDB framework and bands at around 303 and 430  $\text{cm}^{-1}$  are attributed to the Ca-O stretching vibrations ( $\nu_{(\text{Ca-O})}$ ). The peaks in the spectral region of 500 – 900  $\text{cm}^{-1}$  and 1000 – 1200  $\text{cm}^{-1}$  can be assigned as the ring out-of-plane bending and ring in-plane bending modes of the benzene rings of SDB, respectively. The band at 1294  $\text{cm}^{-1}$  is due to the sulfonyl stretching vibrations ( $\nu_{(\text{OSO})}$ ) of the organic linker. The symmetric carbonyl stretching mode ( $\nu_{\text{s}(\text{OCO})}$ ) can be observed at  $\sim 1408 \text{ cm}^{-1}$  and the peaks at  $\sim 1613 \text{ cm}^{-1}$  are ascribed to the asymmetric carbonyl stretching vibrations ( $\nu_{\text{as}(\text{OCO})}$ ).<sup>14</sup> Those well resolved

multiple peaks (enlarged in the inset) that are due to the aromatic C-H stretching ( $\nu_{\text{C-H}}$ ) can be observed at 3044, 3062, 3104 and 3217  $\text{cm}^{-1}$ .

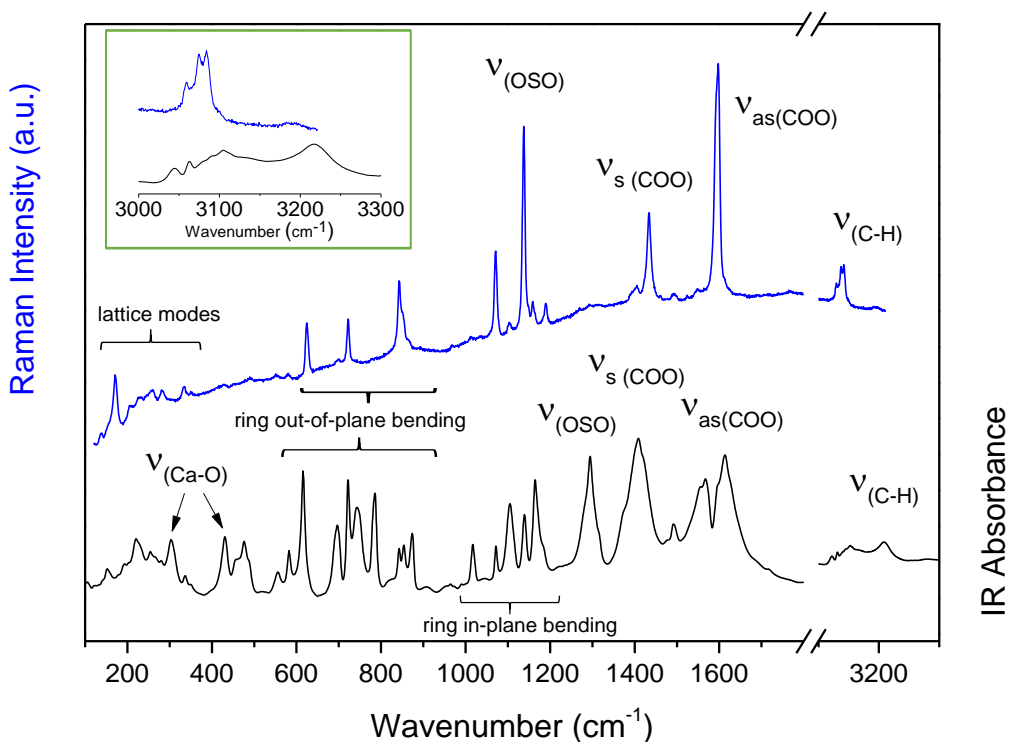


**Figure 6-2.** IR (bottom) and Raman (top) spectra of activated CaSDB at ambient pressure in the frequency region of 100- 3400  $\text{cm}^{-1}$ , with the inset showing the C-H stretching modes in the enlarged spectral region of 3000-3300  $\text{cm}^{-1}$ .

Supplementary to the IR measurements, the Raman spectrum of activated CaSDB at ambient pressure is shown in on the top of Figure 6-2. The Raman peaks in the spectral region of 100–400  $\text{cm}^{-1}$  are assigned to the lattice modes of CaSDB framework, whereas the peaks from 600 to 800  $\text{cm}^{-1}$  are associated with out-of-plane bending vibrations of the benzene rings. The sulfonyl stretching mode ( $\nu_{\text{OSO}}$ ) can be found at 1137  $\text{cm}^{-1}$  and the

symmetric ( $\nu_{s(\text{OCO})}$ ) and asymmetric ( $\nu_{as(\text{OCO})}$ ) carbonyl stretching mode can be observed at 1434 and 1597  $\text{cm}^{-1}$ , respectively. In addition, three sharp peaks at 3059, 3074 and 3084  $\text{cm}^{-1}$  originate from the C-H stretching ( $\nu_{(\text{C-H})}$ ) of the benzene rings. The ambient IR and Raman spectra combined provide the full picture of the crystallinity, the metal-ligand bonding and the local structure of the organic linker of the activated CaSDB framework.

### 6.3.2 IR and Raman spectra of activated CaSDB at high pressures

The far-IR spectra (in the region of 100–550  $\text{cm}^{-1}$ ) of activated CaSDB were collected from ambient to 10.93 GPa and then decompression to ambient pressure, as shown in Figure 6-3 (a). Upon compression from ambient to 3.2 GPa, the Ca-O stretching modes became gradually broadened along with the disappearance and merging of the lattice modes, indicating a decrease of crystallinity of the framework under high pressure. Further compression resulted in continuous broadening of the IR bands accompanied by mode splitting and eventually an almost flattened pattern of the IR profile at 10.93 GPa, suggesting the transformation to an amorphous structure for the framework. Upon complete decompression, the IR spectrum of the recovered sample resembles the initial spectrum at ambient pressure, which strongly indicates that the amorphization of the framework is reversible in the pressure range from ambient to 10.93 GPa.

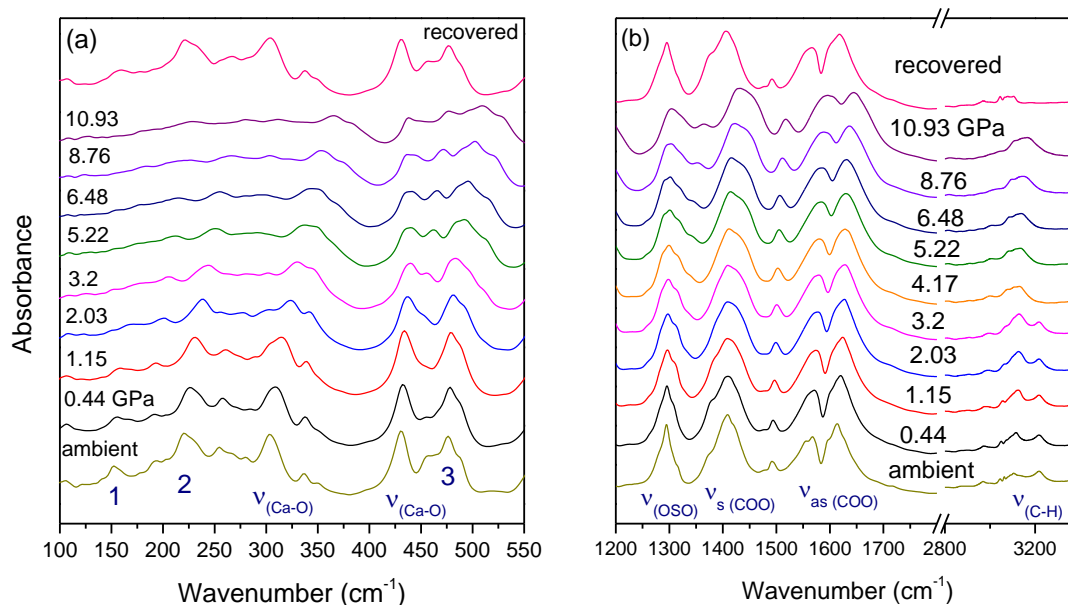


**Figure 6-3.** IR spectra of CaSDB upon compression from ambient to 10.93 GPa and upon recovery in the frequency region (a) 100-550 cm<sup>-1</sup> and (b) 1200-3400 cm<sup>-1</sup>.

While the far-IR data reveal the changes of Ca-O bonding upon compression, the mid-IR spectra provide information of the evolution of local structures of the organic linkers under high pressures. The selected Mid-IR spectra (1200–3400 cm<sup>-1</sup>) of activated CaSDB upon compression and recovery are shown in Figure 6-3 (b). The most significant changes of the IR modes on increasing pressure are the aromatic C-H stretching modes. Upon compression to 3.28 GPa, the intensity of the C-H mode at 3104 cm<sup>-1</sup> was greatly enhanced, along with the merging of the modes at 3044 and 3062 cm<sup>-1</sup> at 0.43 GPa. Upon further compression to 10.92 GPa, the C-H mode at 3217 cm<sup>-1</sup> merged with other C-H modes and became gradually broadened. The sensitive pressure behavior of the C-H modes indicate the enhanced intermolecular interactions, in this case, the ring–ring

interaction of the CaSDB framework. However, the other modes in the mid-IR region, such as the sulfonyl and carbonyl stretching modes, were not very sensitive to pressure, as they did not exhibit obvious changes upon compression. The pressure responses of the sulfonyl and carbonyl modes suggest the robustness of the SDB organic linker. Upon complete decompression, all the modes were clearly recovered, except for the C-H modes, indicating the local structures of the framework has experienced minor modifications. The combination of far-IR and mid-IR data at high pressures shows the high stability of the CaSDB framework which underwent a reversible amorphization upon compression to 10.93 GPa.

The changes of the Raman spectra are consistent with those of IR spectra of activated CaSDB upon compression and recovery, as shown in Figure 6-4. The lattice modes (denoted as 4) at  $171\text{ cm}^{-1}$  (Figure 6-4a) became gradually broadened as pressure increases from ambient to 3.2 GPa, suggesting a decrease of the crystallinity of the framework structure. The C-H stretching modes began to merge upon initial compression to 0.34 GPa and evolved into a single peak at 1.11 GPa. Further compression led to the constant broadening of the modes, in accord to the pressure behavior of the C-H IR modes. In addition, the sulfonyl and carbonyl Raman modes exhibited blue shifts on compression, similar to their counterpart IR modes. At the highest pressure of 10.73 GPa, the Raman modes in the lattice region were much flattened, suggesting the amorphization of the framework. Upon release of pressure, the spectrum of the recovered sample is almost identical to that of ambient CaSDB except for the C-H modes, especially the lattice region, indicating the amorphization of the framework is reversible.

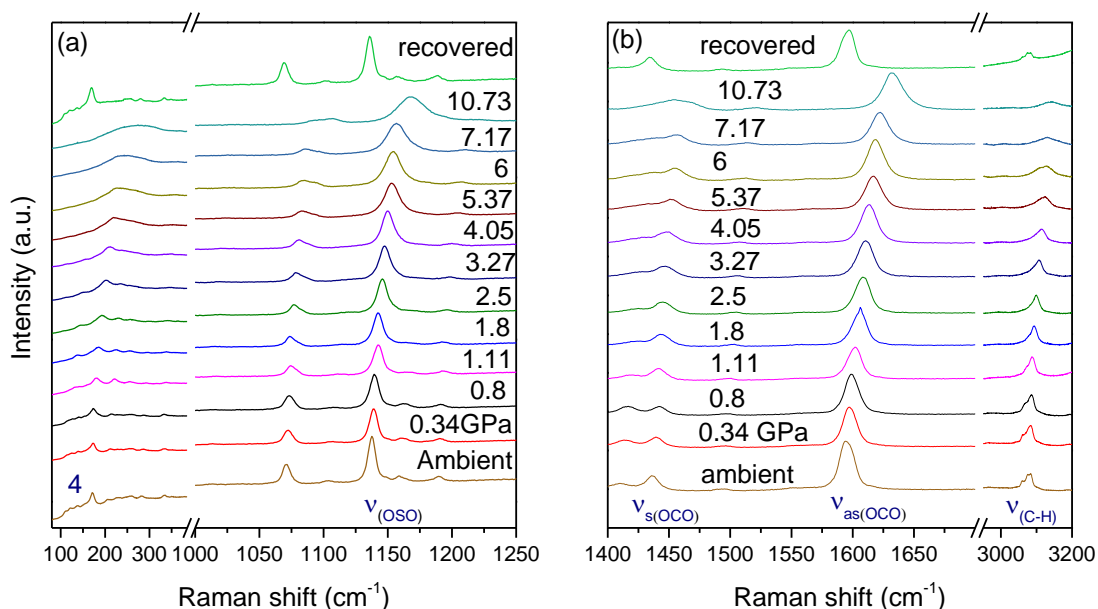


**Figure 6-4.** Raman spectra of CaSDB upon compression from ambient to 10.73 GPa and recovery in the frequency region (a) 100-1250  $\text{cm}^{-1}$  and (b) 1400-3200  $\text{cm}^{-1}$ .

In order to further examine the stability of the CaSDB framework on compression, we monitored selected IR frequencies and Raman shifts as a function of pressure (Figure 6-5). The pressure coefficients ( $dv/dP$  ( $\text{cm}^{-1}\cdot\text{GPa}^{-1}$ )) of the IR and Raman modes were calculated by linear regression of the experimental data and listed in Tables 6-1 and 6-2. In general, all the IR and Raman modes exhibit regular pressure-induced blue shifts, consistent with that the bonds become stiffened upon compression. Most of the pressure coefficients are small in magnitude (i.e.,  $< 5 \text{ cm}^{-1}\cdot\text{GPa}^{-1}$ ), except for the C-H stretch mode, indicating that the bond strength is not very sensitive to compression in the pressure region of 0-11 GPa. Thus the analysis of the pressure dependences of IR and Raman modes further demonstrate the high stability of the activated CaSDB framework.

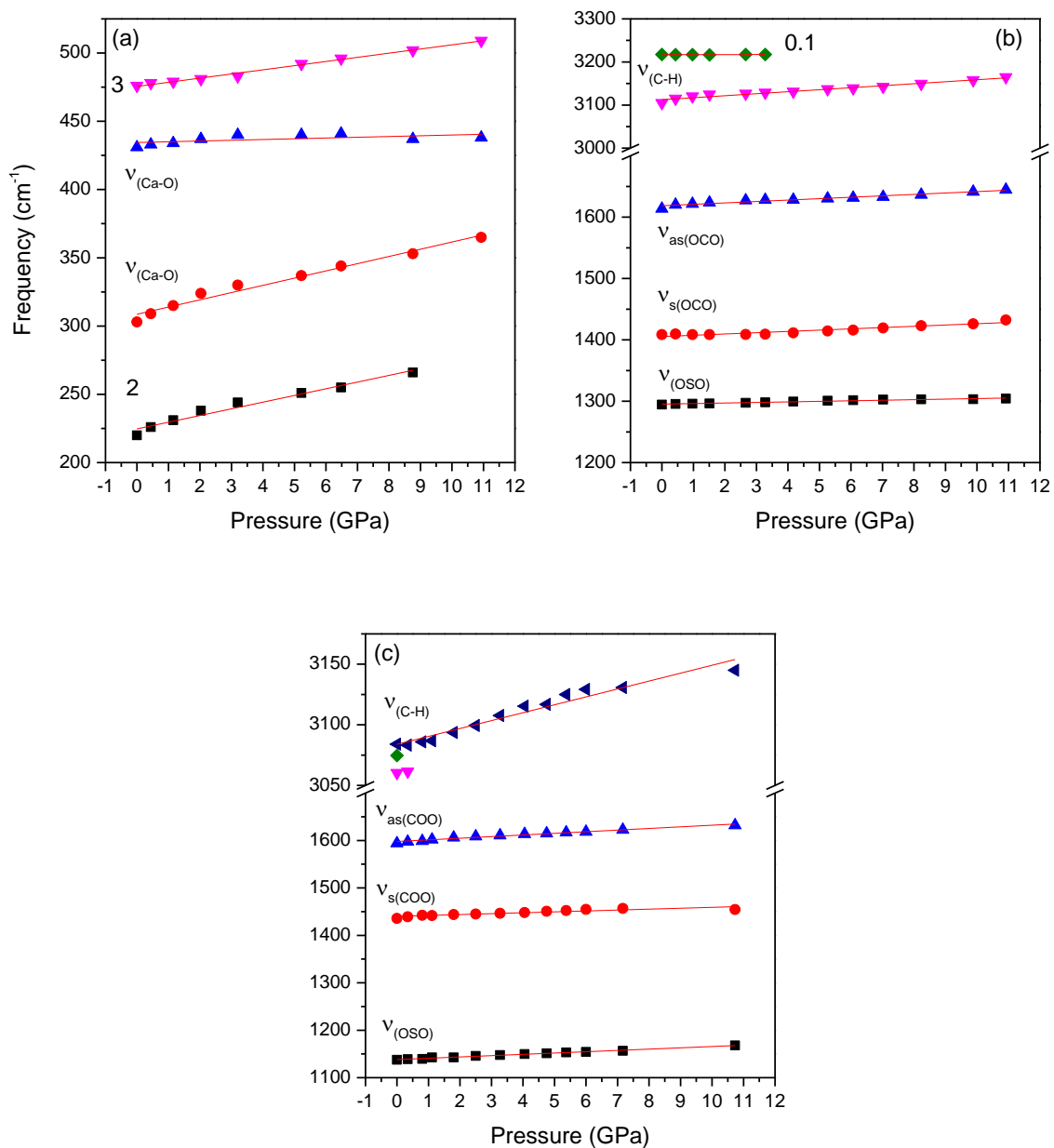


**Figure 6-5.** Frequency of selected (a) far-IR; (b) mid-IR; and (c) Raman modes of CaSDB as a function of pressure from ambient to 11 GPa.



**Table 6-1.** Pressure dependence ( $dv/dP$ ,  $\text{cm}^{-1} \text{GPa}^{-1}$ ) of selected IR modes of CaSDB from ambient to 11 GPa.

<b>IR Mode</b>	<b>Frequency (<math>\text{cm}^{-1}</math>)</b>	<b><math>dv/dP</math> (<math>\text{cm}^{-1} \text{GPa}^{-1}</math>)</b>
V(C-H)	3217	0.1
	3104	4.6
V <sub>as</sub> (OCO)	1613	2.3
V <sub>s</sub> (OCO)	1408	2.1
V(OSO)	1294	0.9
3	476	3.0
V(Ca-O)	431	0.5
	303	5.3
2	220	4.9

**Table 6-2.** Pressure dependence ( $dv/dP$ ,  $\text{cm}^{-1} \text{GPa}^{-1}$ ) of selected Raman modes of CaSDB from ambient to 11 GPa

<b>Raman Mode</b>	<b>Frequency (<math>\text{cm}^{-1}</math>)</b>	<b><math>dv/dP</math> (<math>\text{cm}^{-1} \text{GPa}^{-1}</math>)</b>
V(C-H)	3084	6.5
V <sub>as</sub> (OCO)	1594	3.4
V <sub>s</sub> (OCO)	1435	1.9
V(OSO)	1137	2.8

### 6.3.3 IR spectra of CaSDB loaded with CO<sub>2</sub> at 0.39 GPa

The above results showed the high stability of the activated CaSDB framework upon compression, which is crucial to its application for gas storage. In order to study the performance of CaSDB for CO<sub>2</sub> storage under high pressures and explore the possible adsorption mechanism, the IR and Raman spectra of CaSDB loaded with CO<sub>2</sub> were collected and compared with those of empty framework at similar pressures, as depicted in Figure 6-6. The optical image of the sample chamber that consists of CaSDB (the opaque parts) and solid CO<sub>2</sub> (the transparent area) shown in Figure 6-6a demonstrates the successful loading of CO<sub>2</sub>, which can be further evidenced by the characteristic IR absorption band of CO<sub>2</sub> at 2334 cm<sup>-1</sup> ( $\nu_3$ ) that is due to the asymmetric stretching vibration of O=C=O (Figure 6-6b). Moreover, two sets of high-frequency IR bands can be observed at around 3600 and 3710 cm<sup>-1</sup>, that are assigned as the CO<sub>2</sub> combination modes of  $\nu_3 + 2\nu_2$  and  $\nu_3 + \nu_1$ , respectively.<sup>26</sup> The splitting of  $\nu_3 + \nu_1$  mode of CO<sub>2</sub> (Figure 6-6b inset) indicates the insertion of CO<sub>2</sub> into the pores of CaSDB framework at 0.39 GPa as two different types of CO<sub>2</sub> are present in the system. The one with the lower frequency (3690 cm<sup>-1</sup>) is due to the CO<sub>2</sub> inside the CaSDB channels and the other with higher frequency (3712 cm<sup>-1</sup>) can be assigned as the CO<sub>2</sub> outside the framework as the pressure medium.<sup>28</sup>

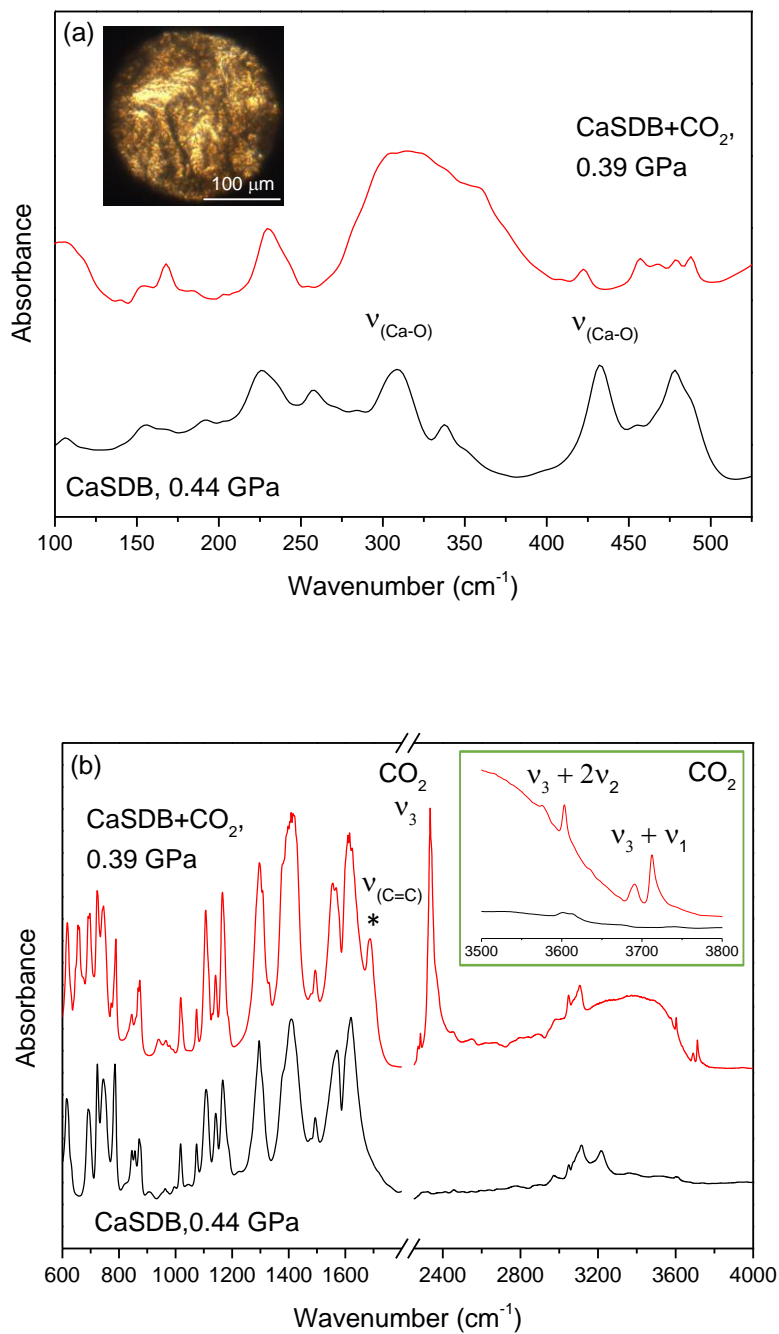


**Figure 6-6.** IR spectra of CaSDB and CO<sub>2</sub> loaded CaSDB at around 0.4 GPa in the spectral region of (a) 100-525  $\text{cm}^{-1}$ ; (b) 600-4000  $\text{cm}^{-1}$ . The inset shows (a) the optical image of the sample chamber of CaSDB loaded with CO<sub>2</sub>; (b) the CO<sub>2</sub> combination modes in the enlarged spectral region of 3550-3800  $\text{cm}^{-1}$ .

The comparison between these two spectra also indicates the strong interactions between CO<sub>2</sub> and the CaSDB framework. Firstly, the intensity and width of one of the  $\nu_{(\text{Ca}-\text{O})}$  mode at 308 cm<sup>-1</sup> was greatly enhanced upon CO<sub>2</sub> loading, whereas the intensity of the other mode at 432 cm<sup>-1</sup> was much weakened. Typically, the band width of an IR mode indicates the ordering of the environment surrounding the mode. Thus the drastic change of the Ca-O band width is caused by the change of the local surroundings of Ca<sup>2+</sup> due to the strong interaction between the oxygen of CO<sub>2</sub> and the calcium metal center. Secondly, a new peak at 1687 cm<sup>-1</sup> appeared in the spectrum of CO<sub>2</sub> loaded CaSDB, which can be assigned to the C=C stretching mode of the benzene ring. The enhancement of the C=C mode, which is otherwise lacking in the IR spectrum of pure CaSDB, strongly suggests the guest-host interaction on the specific site of the benzene ring. All these significant changes of the IR modes of CaSDB upon CO<sub>2</sub> loading demonstrate direct evidence of interactions between CO<sub>2</sub> and the framework and the specific adsorption sites of the framework.

#### 6.3.4 IR and Raman spectra of CaSDB loaded with CO<sub>2</sub> at high pressures

To study the pressure effects on the performance of CaSDB framework for CO<sub>2</sub> storage, the IR and Raman spectra of the framework loaded with CO<sub>2</sub> upon compression and decompression were measured, as shown in Figures 6-7 and 6-9. CO<sub>2</sub> was found to be inserted into the channels of the framework in the entire pressure region from 0.24 GPa to 13.69 GPa, as two sets of  $\nu_3 + \nu_1$  mode of CO<sub>2</sub> were observed (Figure 6-7c), which experienced gradual pressure-induced blue shift and broadening on increasing pressure. In the far-IR region (Figure 6-7a), one of the most striking changes of the IR mode in response

to pressure was the Ca-O stretch mode at  $\sim 300 \text{ cm}^{-1}$ , which experienced an obvious decrease of band width upon compression from 0.24 GPa to 1.03 GPa, indicating a gradual formation of Ca-O bond between the metal center and  $\text{CO}_2$ . Upon further compression, the broad Ca-O stretch mode slowly evolved into two single peaks with a drop of intensity. The drastic change of the Ca-O modes suggests a pressure-enhanced interaction between the oxygen of  $\text{CO}_2$  and the  $\text{Ca}^{2+}$  of the CaSDB framework as more  $\text{CO}_2$  were forced into the framework. Other changes in the far-IR region include the enhancement of the intensity of the lattice mode at  $165 \text{ cm}^{-1}$  and broadening of the lattice mode at  $228 \text{ cm}^{-1}$  upon compression. A new IR peak (denoted as A) at  $214 \text{ cm}^{-1}$  appeared at 5.39 GPa and its intensity increased on compression. The appearance of new peaks usually suggest a phase transition in the framework. Thus the  $\text{CO}_2$  loaded CaSDB might experience a phase transformation at around 5.39 GPa. The pure CaSDB framework was found to be very stable to compression, thus the phase transition is highly likely induced by strong  $\text{CO}_2$  interactions with the framework. At the highest pressure of 13.6 GPa, the IR profile in the far-IR region can be characterized by an extremely broadened pattern, indicating the amorphization of  $\text{CO}_2$  loaded CaSDB framework. In the mid-IR range (Figure 6-7b), most of the IR modes were gradually broadened upon compression. It is worth noting that the C=C stretching mode showed an obvious red shift as pressure increases and disappeared above 4.74 GPa. The weakening of C=C mode is a result of the interaction between the molecular quadrupole of adsorbed  $\text{CO}_2$  molecules and the phenyl rings of the linker, consistent with Plonka *et al.*'s study.<sup>14</sup> Upon decompression and complete recovery, all the modifications of the IR modes were found to be reversible, except for the  $\text{CO}_2$  modes such as  $\nu_3 + 2\nu_2$  and  $\nu_3 + \nu_1$  mode as all the  $\text{CO}_2$  molecules escape from the sample chamber.

The Raman peaks (denoted as 4-7) in the region 100-400  $\text{cm}^{-1}$  are associated with the lattice modes of the CaSDB framework (Figure 6-9a). Upon compression to 1.44 GPa, three new peaks appeared at 85 and 105  $\text{cm}^{-1}$  that can be assigned as the  $E_g$ ,  $F_{g-}$  and  $F_{g+}$  mode of solid  $\text{CO}_2$ , respectively, indicating that the sample in the DAC consists of CaSDB and highly crystalline solid  $\text{CO}_2$  (phase I) outside the framework.<sup>37</sup> Furthermore, additional Raman peak (denoted as B) appeared at 160  $\text{cm}^{-1}$  at 1.44 GPa due to the enhanced  $\text{CO}_2$ -framework interaction. Upon further compression to 4.08 GPa, the intensity of the  $E_g$ ,  $F_{g-}$  and  $F_{g+}$  modes of crystalline  $\text{CO}_2$  along with the lattice modes B and 4 were much enhanced. From 5.39 GPa to 11.97 GPa (Figure 6-9b), the lattice mode 5 and 6 disappeared and the other lattice modes of CaSDB became broadened, indicating a decrease of crystallinity of the framework. At the highest pressure of 13.6 GPa, the entire Raman pattern was almost flattened, suggesting a transformation to an amorphous structure. Upon decompression, the changes of the Raman peaks are found to be reversible. When the pressure was released to 0.24 GPa, the spectrum resembles the initial one at the same pressure. Thus the  $\text{CO}_2$  loaded CaSDB framework maintained the original structure and crystallinity upon compression from 13.6 GPa.

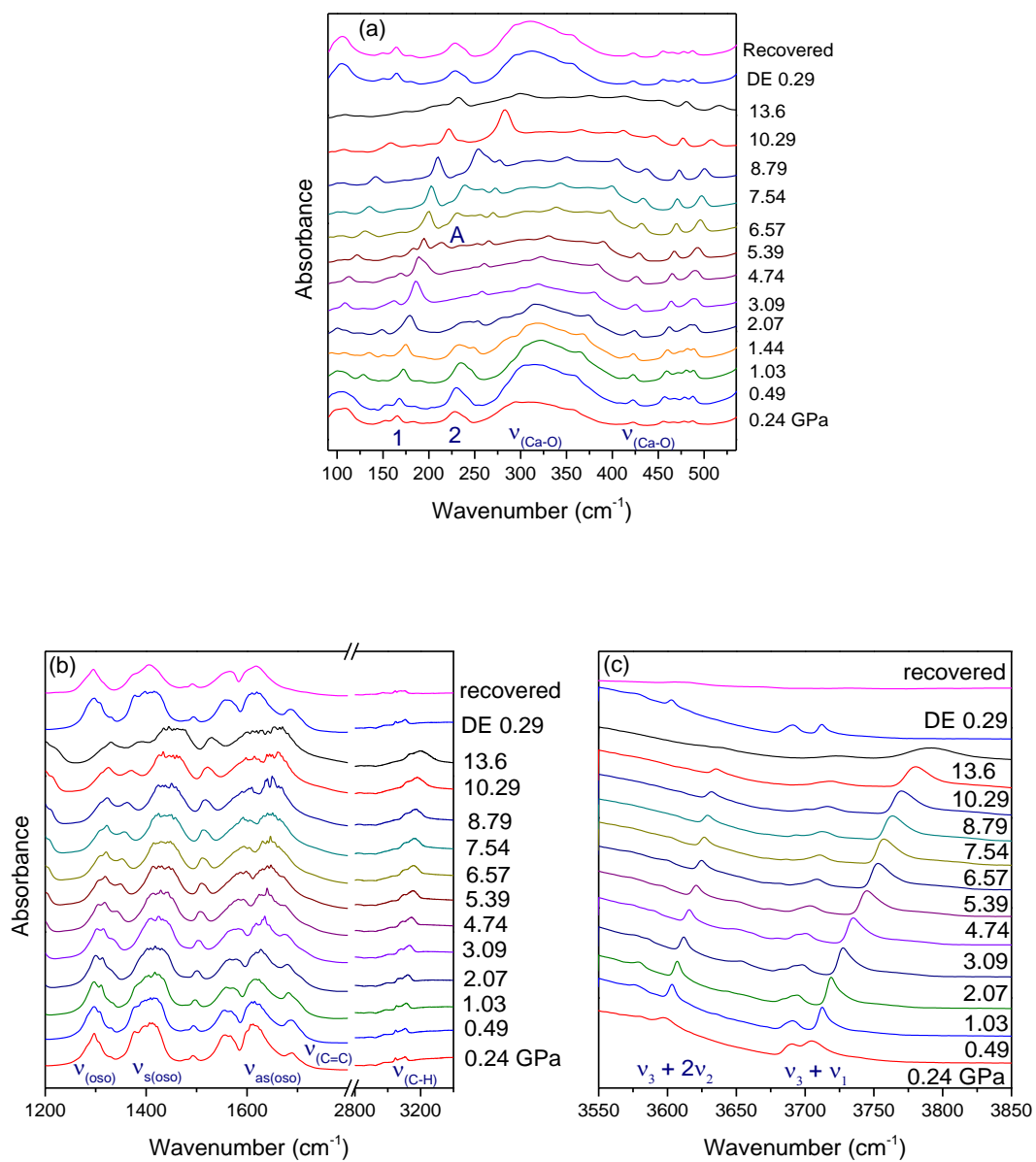


**Figure 6-7.** IR spectra of CaSDB loaded with CO<sub>2</sub> upon compression from 0.24 to 13.6 GPa and recovery in the frequency region (a) 90-535 cm<sup>-1</sup>; (b) 1200-3300 cm<sup>-1</sup> and (c) 3550-3850 cm<sup>-1</sup>.

To further examine the boundary of the phase transition for the CO<sub>2</sub> loaded CaSDB framework, the frequency of selected IR and Raman modes as a function of pressure from 0.24 to 13.6 GPa were analyzed in Figures 6-8 (IR) and 6-9c (Raman); along with the pressure dependences listed in Tables 6-3 (IR) and 6-4 (Raman). In general, the change in the slope of pressure-dependence, disappearance of the initial peaks, and appearance of new peaks provide evidence for the start and finish of phase transitions of the structure. Thus, the approximate phase boundary for the CO<sub>2</sub> loaded CaSDB framework is around 5 GPa, as evidenced by the slope change for all the selected modes (Figures 6-8 and 6-9c) and the appearance of a new IR mode  $\nu_A$  at such pressure (Figure 6-7a). Since the empty CaSDB framework shows high stability (no phase transition) under high pressure, hence the phase transition of the CO<sub>2</sub> loaded framework results from the strong interactions with CO<sub>2</sub>.



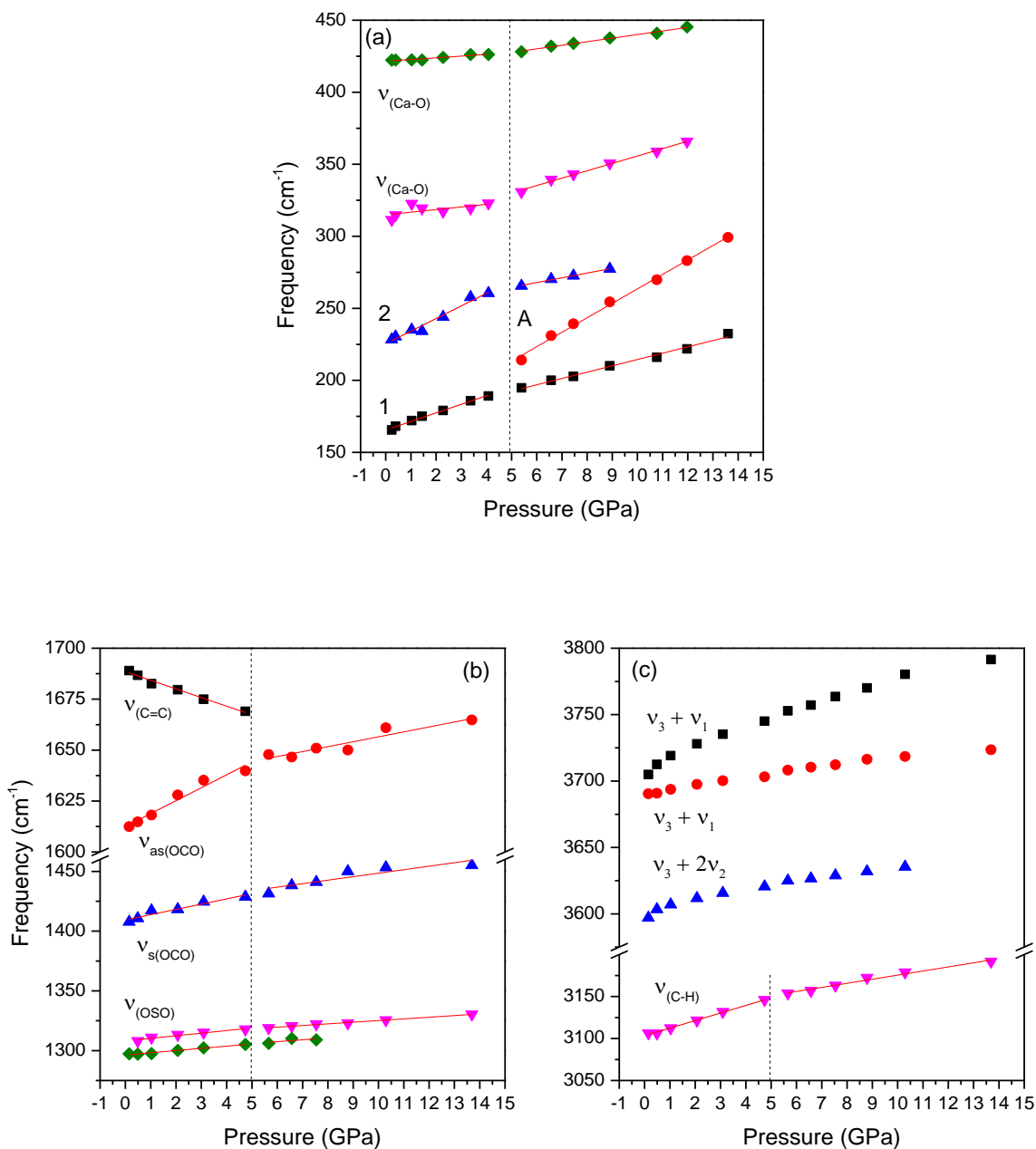


**Figure 6-8.** Frequency of selected IR modes of CaSDB loaded with  $\text{CO}_2$  GPa in the frequency region of (a) 150-450  $\text{cm}^{-1}$ ; (b) 1275-1700  $\text{cm}^{-1}$  and (c) 3050-3800  $\text{cm}^{-1}$  as a function of pressure from 0.24 to 13.6 GPa.

**Table 6-3.** Pressure dependence ( $dv/dP$ ,  $\text{cm}^{-1} \text{GPa}^{-1}$ ) of selected IR modes of CaSDB loaded with  $\text{CO}_2$  from 0.24 to 13.6 GPa.

IR mode	Frequency ( $\text{cm}^{-1}$ )	$dv/dP$ ( $\text{cm}^{-1} \cdot \text{GPa}^{-1}$ )	
		0.24 - 5 GPa	5 - 13.6 GPa
$\nu_{\text{(C-H)}}$	3106	9.0	4.9
$\nu_{\text{(C=C)}}$	1689	-4.2	
$\nu_{\text{as(OCO)}}$	1612	6.3	2.4
$\nu_{\text{s(OCO)}}$	1407	4.4	2.9
$\nu_{\text{(OSO)}}$	1308	2.2	1.4
	1297	1.9	1.5
$\nu_{\text{(Ca-O)}}$	422	1.2	2.5
	311	1.8	5.1
2	228	8.8	3.3
A	214		10.0
1	165	6.0	4.4

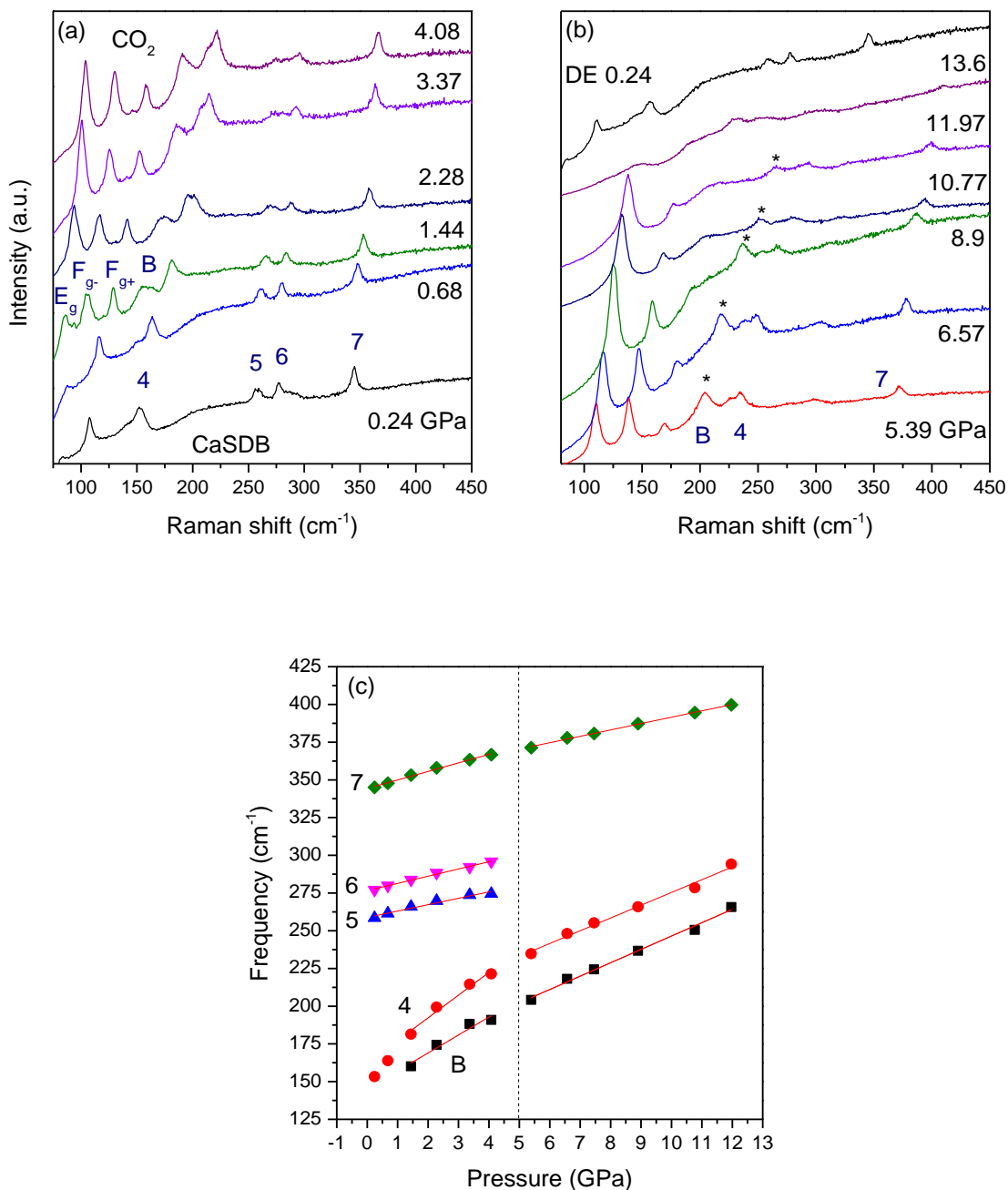


**Figure 6-9.** Raman spectra of CaSDB upon compression from (a) 0.24-4.08 GPa; (b) 5.39-13.6 GPa and recovery in the frequency region of 75-450 cm<sup>-1</sup> and (c) Frequency of selected Raman modes of CaSDB loaded with CO<sub>2</sub> as a function of pressure from 0.24 to 13.6 GPa.

**Table 6-4.** Pressure dependence ( $dv/dP$ ,  $\text{cm}^{-1} \cdot \text{GPa}^{-1}$ ) of selected Raman modes of CaSDB loaded with  $\text{CO}_2$  from 0.24 to 13.6 GPa.

Raman mode	Frequency ( $\text{cm}^{-1}$ )	$dv/dP$ ( $\text{cm}^{-1} \cdot \text{GPa}^{-1}$ )	
		0.24 - 5 GPa	5 - 13.6 GPa
7	345	5.7	4.2
6	277	4.8	
5	258	4.2	
4	181	15.0	8.5
B	160	11.9	8.9

## 6.4 Discussion

The above results showed the high stability of activated CaSDB framework under high pressure and an enhanced CO<sub>2</sub> storage in CaSDB induced by pressure. Thus, in-depth understanding of the contributing factors to the framework stability as well as the guest-host interaction mechanisms are of fundamental interest. Firstly, the Far-IR and Raman measurements suggest that the activated CaSDB framework exhibit high crystallinity upon compression to 3.2 GPa evidenced by the well-resolved lattice modes. The crystalline stability is close to that of  $\alpha$ -Mg<sub>3</sub>(HCOO)<sub>6</sub> and significantly higher than those of other MOFs investigated under high pressure such as ZIF-8. According to Mao's work, the activated  $\alpha$ -Mg<sub>3</sub>(HCOO)<sub>6</sub> framework stays crystalline up to 4 GPa with an irreversible crystalline-to-crystalline phase transition at 2 GPa.<sup>36</sup> In contrast, Chapman *et al.*<sup>21</sup> demonstrated that the ZIF-8 framework undergoes irreversible amorphization upon slight compression to 0.34 GPa. Based on previous studies, the crystalline stability of a MOF framework mainly depends on the porosity of the framework and the connectivity between the metal center and organic ligands. The BET surface area and pore volume of CaSDB are 224 m<sup>2</sup>/g and 0.65 cm<sup>3</sup>/g, respectively<sup>12</sup>, which are slightly higher than those of  $\alpha$ -Mg<sub>3</sub>(HCOO)<sub>6</sub>;<sup>38</sup> yet much smaller than those of ZIF-8.<sup>39</sup> Thus the relatively low porosity of CaSDB makes the framework crystalline stable. Moreover, the metal center of CaSDB not only connects with carboxylic oxygens, but also bonds to one of the sulfonyl oxygens from the ligands due to the special geometry of the SDB ligand. Usually, the metal center of a MOF framework only bounds to one kind of functional group of the organic linker. The unique connection of the metal center to bi-functional groups of the organic linker further helps the stabilization of framework crystallinity to compression. Further

compression to higher pressures (>3.2 GPa) resulted in a gradual disordering of the framework, but the channels remains intact up to 11 GPa.

The structural stability of MOFs is crucial to their sorption applications. The high stability of the framework probed by IR and Raman spectra suggests that CaSDB is a promising candidate for CO<sub>2</sub> storage under high pressure loading conditions. Previous studies of CO<sub>2</sub> adsorption in CaSDB only limited the pressure range to ambient pressure. Thus it is imperative to comprehend the CO<sub>2</sub> adsorption mechanisms by CaSDB at elevated pressures. Based on the mid-IR results, the splitting of the CO<sub>2</sub> combination mode  $\nu_3 + \nu_1$  occurred at very low pressure (i.e. 0.24 GPa) and room temperature, under which CO<sub>2</sub> was in liquid phase.<sup>37</sup> Thus the fact that two distinctly different CO<sub>2</sub> molecules present in the system under above conditions indicates the CO<sub>2</sub> included in the pores had strong bonding with the framework and limited mobility, in strong contrast to the liquid CO<sub>2</sub> outside the framework. This observation is comparable with that of MIL-68(In) which contains big-size pores (11.6 Å) and preferential binding sites (OH units) for CO<sub>2</sub>. Thus the splitting of the CO<sub>2</sub> combination mode  $\nu_3 + \nu_1$  suggests that the CaSDB framework has a high affinity towards CO<sub>2</sub> under mild pressure conditions as low as 0.24 GPa. Furthermore, our IR data of CO<sub>2</sub> loaded CaSDB showed that the benzene ring of the organic linker is one of the major interaction sites for CO<sub>2</sub>, in accord to previous study at ambient pressure that described the nature of the interaction as the interplay between the delocalized  $\pi$  aromatic system of the phenyl rings and the molecular quadrupole of CO<sub>2</sub>.<sup>14</sup> The unique geometry of the SDB ligand results in a pocket where the adsorbed CO<sub>2</sub> molecule is placed between two centroids of the aromatic rings, as illustrated in Figure 10a. More importantly, the drastic change of the Ca-O stretch mode (especially the increase of the band width) of

CaSDB upon initial CO<sub>2</sub> loading (0.24 GPa) suggests a strong interaction between CO<sub>2</sub> and the calcium metal center, as shown in Figure 10b. The observation of the metal-CO<sub>2</sub> interaction in CaSDB is novel under high pressure, in addition to the phenyl-CO<sub>2</sub> interaction at ambient pressure. Thus our results demonstrate much stronger CO<sub>2</sub>-framework interactions induced by high pressure. In addition, based on the absorption intensity of the two components of the  $\nu_3 + \nu_1$  mode, we estimated that up to ~33.6 % of the loaded CO<sub>2</sub> was inserted in the framework, close to the CO<sub>2</sub> uptake in ZIF-8 at high pressures.<sup>26</sup>

Being guest molecules, CO<sub>2</sub> substantially in turn, influences the structural stability of CaSDB under high pressure. The CO<sub>2</sub> loaded framework was found to undergo a crystalline-to-crystalline phase transition at around 5 GPa, whereas the empty framework maintained the same structure up to 11 GPa. The phase transition for the CO<sub>2</sub> loaded CaSDB was probably induced by a reorientation of the benzene rings to increase the pore opening, allowing more CO<sub>2</sub> to accommodate in the channels as pressure increases, as depicted in Figure 6-10b. As mentioned, the phenyl rings 1 & 2 or 3 & 4 of the SDB ligand are in such an optimized geometry that CO<sub>2</sub> molecules can be contained in the middle of the “pocket” upon adsorption at ambient pressure. However, the two phenyl rings 1 & 4 or 2 & 3 are in a twisted configuration and thus cannot provide an adsorption site for CO<sub>2</sub> to interact with both rings (Figure 6-10a). Upon compression, the phenyl ring 3 (or 4) can be reoriented to form an additional “ $\pi$  pocket” with phenyl 2 (or 1), generating another CO<sub>2</sub> adsorption site (Figure 6-10b). The flexibility of the benzene ring was reported before. Prior study of biphenyl showed a phase transition from a twisted to a planar conformation at 0.18 GPa due to the pressure-induced twist of the rings.<sup>40</sup> Thus it is possible that the

strong CO<sub>2</sub>-framework interaction forced the reorientation of the benzene rings of SDB ligand, which can be described as two phenyl rings connected by sulfonyl group, despite the fact that the SDB ligand itself is quite resilient to compression. Besides, the guest adsorption-driven phase transition of other MOFs were investigated many times before, including the study on the specific CO<sub>2</sub> adsorption-induced phase transformations of MOFs.<sup>41-46</sup> For example, MIL-53 (Cr) experienced so-called “breathing” transitions between large pore and narrow pore phases during CO<sub>2</sub> adsorption.<sup>47</sup> *In situ* X-ray diffraction measurements on the CO<sub>2</sub> loaded CaSDB at high pressures would be helpful to elucidate the exact interaction mechanism between CO<sub>2</sub> and the framework, including the phase transition and specific adsorption sites.



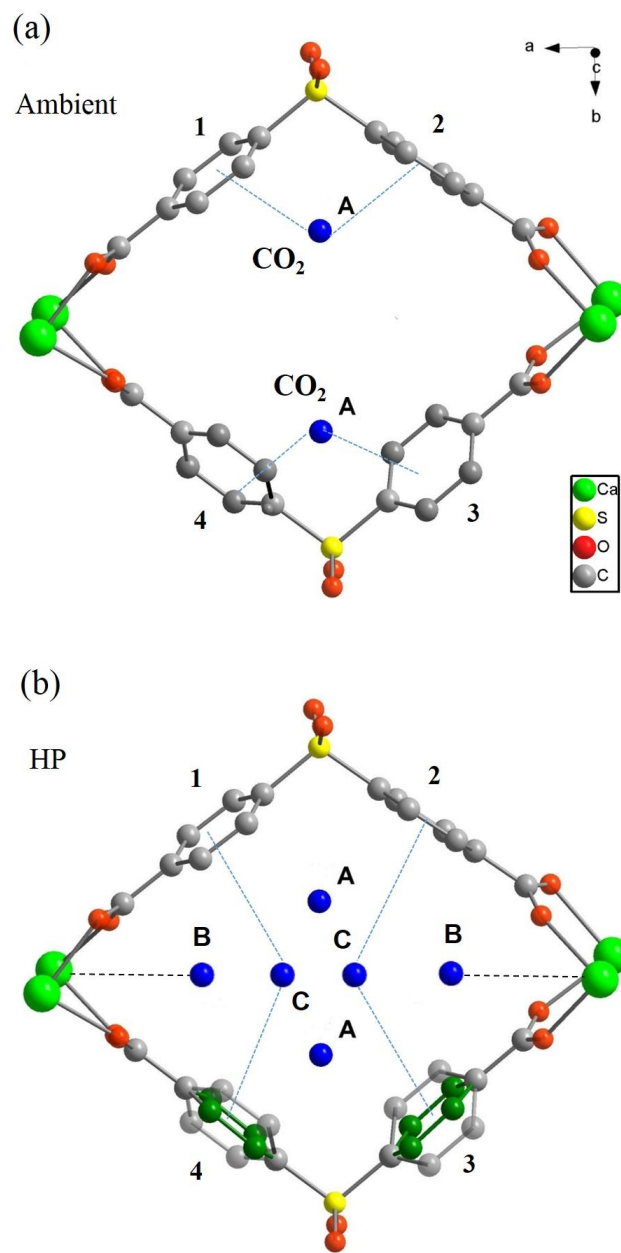


**Figure 6-10.** CO<sub>2</sub> adsorption in CaSDB at (a) ambient pressure; (b) high pressures (HP). The blue balls represent CO<sub>2</sub> molecules inside the pores of CaSDB, with the oxygen atoms omitted. The dash lines symbolize the interactions between CO<sub>2</sub> and the specific adsorption sites of the framework.

## 6.5 Conclusions

In summary, the stability of activated CaSDB framework and its performance for CO<sub>2</sub> storage under high pressures were investigated by *in situ* IR and Raman spectroscopic measurements. The activated CaSDB framework which underwent a reversible amorphization at 11 GPa exhibited high stability upon compression. We also demonstrated a remarkable affinity between CO<sub>2</sub> and the framework evidenced by the splitting of the  $\nu_3 + \nu_1$  mode of CO<sub>2</sub> at very low pressure (0.24 GPa). Strong guest-host interactions are apparent from the IR features of the framework in the Ca-O, C=C stretching region, providing key information about the possible CO<sub>2</sub> adsorption sites of CaSDB. In particular, the CO<sub>2</sub>-metal interaction is novel and intriguing. As guest molecules, CO<sub>2</sub> substantially influenced the structure of CaSDB and triggered a reversible phase transition of the framework at 5 GPa, involving the reorientation of the phenyl rings to allow accommodation for more CO<sub>2</sub> storage. Our results provide a fundamental understanding of CO<sub>2</sub> adsorption mechanism in CaSDB, which is promising for the application of greenhouse storage.

## 6.6 Reference

- (1) Zhou, H. C. K., S. *Chemical Society Reviews* **2014**, *43*, 5415.
- (2) Zhou, H.-C.; Long, J. R.; Yaghi, O. M. *Chemical Reviews* **2012**, *112*, 673.
- (3) Furukawa, H.; Cordova, K. E.; O’Keeffe, M.; Yaghi, O. M. *Science* **2013**, *341*, 1230444.
- (4) He, Y.; Zhou, W.; Qian, G.; Chen, B. *Chemical Society Reviews* **2014**, *43*, 5657.
- (5) Sumida, K.; Rogow, D. L.; Mason, J. A.; McDonald, T. M.; Bloch, E. D.; Herm, Z. R.; Bae, T. H.; Long, J. R. *Chemical Reviews* **2012**, *112*, 724.
- (6) Ma, S.; Zhou, H.-C. *Chemical Communications* **2010**, *46*, 44.

- (7) Poloni, R.; Lee, K.; Berger, R. F.; Smit, B.; Neaton, J. B. *The Journal of Physical Chemistry Letters* **2014**, *5*, 861.
- (8) Liu, Y.; Wang, Z. U.; Zhou, H.-C. *Greenhouse Gases: Science and Technology* **2012**, *2*, 239.
- (9) Li, J.-R.; Ma, Y.; McCarthy, M. C.; Sculley, J.; Yu, J.; Jeong, H.-K.; Balbuena, P. B.; Zhou, H.-C. *Coordination Chemistry Reviews* **2011**, *255*, 1791.
- (10) Liu, J.; Thallapally, P. K.; McGrail, B. P.; Brown, D. R.; Liu, J. *Chemical Society Reviews* **2012**, *41*, 2308.
- (11) Lee, J. D. *Concise Inorganic Chemistry*; Chapman & Hall: New York, **1991**, 4th ed.
- (12) Yeh, C.-T.; Lin, W.-C.; Lo, S.-H.; Kao, C.-C.; Lin, C.-H.; Yang, C.-C. *CrystEngComm* **2012**, *14*, 1219.
- (13) Banerjee, D.; Zhang, Z.; Plonka, A. M.; Li, J.; Parise, J. B. *Crystal Growth & Design* **2012**, *12*, 2162.
- (14) Plonka, A. M.; Banerjee, D.; Woerner, W. R.; Zhang, Z.; Nijem, N.; Chabal, Y. J.; Li, J.; Parise, J. B. *Angewandte Chemie International Edition* **2013**, *52*, 1692.
- (15) Spencer, E. C.; Kiran, M. S. R. N.; Li, W.; Ramamurty, U.; Ross, N. L.; Cheetham, A. K. *Angewandte Chemie International Edition* **2014**, *53*, 5583.
- (16) Ortiz, A. U.; Boutin, A.; Gagnon, K. J.; Clearfield, A.; Coudert, F.-X. *Journal of the American Chemical Society* **2014**, *136*, 11540.
- (17) Gagnon, K. J.; Beavers, C. M.; Clearfield, A. *Journal of the American Chemical Society* **2013**, *135*, 1252.
- (18) Hu, Y.; Kazemian, H.; Rohani, S.; Huang, Y.; Song, Y. *Chemical Communications* **2011**, *47*, 12694.
- (19) Su, Z.; Miao, Y.-R.; Mao, S.-M.; Zhang, G.-H.; Dillon, S.; Miller, J. T.; Suslick, K. S. *Journal of the American Chemical Society* **2015**, *137*, 1750.
- (20) Serra-Crespo, P.; Dikhtiarenko, A.; Stavitski, E.; Juan-Alcaniz, J.; Kapteijn, F.; Coudert, F.-X.; Gascon, J. *CrystEngComm* **2015**, *17*, 276.
- (21) Chapman, K. W.; Halder, G. J.; Chupas, P. J. *Journal of the American Chemical Society* **2009**, *131*, 17546.
- (22) Serra-Crespo, P.; Stavitski, E.; Kapteijn, F.; Gascon, J. *RSC Advances* **2012**, *2*, 5051.
- (23) Zhou, M.; Wang, K.; Men, Z.; Sun, C.; Li, Z.; Liu, B.; Zou, G.; Zou, B. *CrystEngComm* **2014**, *16*, 4084.
- (24) Ortiz, A. U.; Boutin, A.; Coudert, F.-X. *Chemical Communications* **2014**, *50*, 5867.

- (25) Yot, P. G.; Ma, Q.; Haines, J.; Yang, Q.; Ghoufi, A.; Devic, T.; Serre, C.; Dmitriev, V.; Ferey, G.; Zhong, C.; Maurin, G. *Chemical Science* **2012**, *3*, 1100.
- (26) Hu, Y.; Liu, Z.; Xu, J.; Huang, Y.; Song, Y. *Journal of the American Chemical Society* **2013**, *135*, 9287.
- (27) Graham, A. J.; Tan, J.-C.; Allan, D. R.; Moggach, S. A. *Chemical Communications* **2012**, *48*, 1535.
- (28) Santoro, M.; Gorelli, F.; Haines, J.; Cambon, O.; Levelut, C.; Garbarino, G. *Proceedings of the National Academy of Sciences* **2011**, *108*, 7689.
- (29) Lee, Y.; Liu, D.; Seoung, D.; Liu, Z. X.; Kao, C. C.; Vogt, T. *Journal of the American Chemical Society* **2011**, *133*, 1674.
- (30) Graham, A. J.; Allan, D. R.; Muszkiewicz, A.; Morrison, C. A.; Moggach, S. A. *Angewandte Chemie International Edition* **2011**, *50*, 11138.
- (31) Chapman, K. W.; Sava, D. F.; Halder, G. J.; Chupas, P. J.; Nenoff, T. M. *Journal of the American Chemical Society* **2011**, *133*, 18583.
- (32) Moggach, S. A.; Bennett, T. D.; Cheetham, A. K. *Angewandte Chemie International Edition* **2009**, *48*, 7087.
- (33) Bennett, T. D.; Sotelo, J.; Tan, J.-C.; Moggach, S. A. *CrystEngComm* **2015**, *17*, 286.
- (34) Mao, H. K.; Xu, J.; Bell, P. M. *Journal of Geophysical Research: Solid Earth* **1986**, *91*, 4673.
- (35) Dong, Z. H.; Song, Y. *Applied Physics Letters* **2010**, *96*, 151903.
- (36) Mao, H.; Xu, J.; Hu, Y.; Huang, Y.; Song, Y. *Journal of Materials Chemistry A* **2015**, *3*, 11976.
- (37) Hanson, R. C.; Jones, L. H. *The Journal of Chemical Physics* **1981**, *75*, 1102.
- (38) Rood, J. A.; Noll, B. C.; Henderson, K. W. *Inorganic Chemistry* **2006**, *45*, 5521.
- (39) Phan, A.; Doonan, C. J.; Uribe-Romo, F. J.; Knobler, C. B.; O'Keeffe, M.; Yaghi, O. M. *Accounts of Chemical Research* **2010**, *43*, 58.
- (40) Zhuravlev, K. K.; McCluskey, M. D. *The Journal of Chemical Physics* **2002**, *117*, 3748.
- (41) Li, Q.; Li, S.; Wang, K.; Liu, J.; Yang, K.; Liu, B.; Zou, G.; Zou, B. *The Journal of Physical Chemistry C* **2014**, *118*, 5848.
- (42) Graham, A. J.; Banu, A.-M.; Duren, T.; Greenaway, A.; McKellar, S. C.; Mowat, J. P. S.; Ward, K.; Wright, P. A.; Moggach, S. A. *Journal of the American Chemical Society* **2014**, *136*, 8606.
- (43) Lapidus, S. H.; Halder, G. J.; Chupas, P. J.; Chapman, K. W. *Journal of the American Chemical Society* **2013**, *135*, 7621.

- (44) Fairen-Jimenez, D.; Moggach, S. A.; Wharmby, M. T.; Wright, P. A.; Parsons, S.; Düren, T. *Journal of the American Chemical Society* **2011**, *133*, 8900.
- (45) Cheng, Y.; Kajiro, H.; Noguchi, H.; Kondo, A.; Ohba, T.; Hattori, Y.; Kaneko, K.; Kanoh, H. *Langmuir* **2011**, *27*, 6905.
- (46) Kitaura, R.; Seki, K.; Akiyama, G.; Kitagawa, S. *Angewandte Chemie International Edition* **2003**, *42*, 428.
- (47) Neimark, A. V.; Coudert, F.-X.; Triguero, C.; Boutin, A.; Fuchs, A. H.; Beurroies, I.; Denoyel, R. *Langmuir* **2011**, *27*, 4734.

## Chapter 7

### 7 Summary and Future Work

#### 7.1 Summary

In this thesis, high pressure *in situ* IR and Raman spectroscopy were used to examine the stability as well as the CO<sub>2</sub> adsorption performance of a series of MOFs with different topology and structures. All the MOFs exhibited extraordinary stability at high pressures, retaining chemical connectivity and porosity for CO<sub>2</sub> storage. Additional CO<sub>2</sub> adsorption sites have been observed in these MOFs under high pressure, suggesting enhanced guest-host interactions between CO<sub>2</sub> and the frameworks. The porosity, flexibility of the framework and the existence of preferential CO<sub>2</sub> adsorption sites play an important role in the performance of the frameworks for CO<sub>2</sub> storage.

In *Chapters 2 and 3*, it was shown that the ZIF-8 framework sustained extreme compression up to 39 GPa without permanent breakdown; and experienced fully reversible structural modifications upon compression from 1.6 GPa. Upon CO<sub>2</sub> loading, strong interactions between CO<sub>2</sub> and the framework were apparent from the IR features of the framework in the C=C stretching region, providing key information about the possible adsorption site. As guest molecules, CO<sub>2</sub> substantially enhanced the structural stability of the ZIF-8 framework.

In *Chapter 4*, the MIL-68 (In) framework exhibited high stability under compression up to 9 GPa, while the pressure-induced structural modifications were found to be completely reversible for the as-made framework but irreversible for the activated framework. The difference in the reversibility of framework is attributed to the solvent

DMF molecules contained in the channels. More interestingly, the normally inaccessible triangular pores became available for CO<sub>2</sub> at elevated pressures (e.g., > 1.5 GPa). The unique adsorption behavior of CO<sub>2</sub> in the framework was associated with the OH units that were the primary binding sites through hydrogen bonding. In addition, the pressure-enhanced CO<sub>2</sub> storage behavior and the guest-host interaction mechanism were explored with the aid of Monte Carlo molecular mechanics simulations.

*Chapter 5* described a distinctly different CO<sub>2</sub> adsorption behavior in  $\alpha$ -Mg<sub>3</sub>(HCOO)<sub>6</sub> versus those in ZIF-8 or MIL-68 (In). At high pressures, the CO<sub>2</sub> molecules were highly confined inside the pores due to strong dipole-dipole interactions with the formate ligand of the framework. Moreover, the CO<sub>2</sub> loaded  $\alpha$ -Mg<sub>3</sub>(HCOO)<sub>6</sub> framework underwent a reversible crystalline-to-amorphous phase transformation at around 4.5 GPa, as evidenced by the Raman measurements.

*Chapter 6* revealed a remarkable affinity between CO<sub>2</sub> and the CaSDB framework, as multiple CO<sub>2</sub> adsorption sites in the framework were observed under high pressure in addition to the single interaction site at ambient pressure. In particular, the far-IR measurements suggested a CO<sub>2</sub>-metal interaction in CaSDB induced by pressure. As guest molecules, CO<sub>2</sub> substantially influenced the structure of CaSDB and triggered a reversible crystalline-to-crystalline phase transition of the framework at 5 GPa, involving the reorientation of the phenyl rings to allow accommodation for more CO<sub>2</sub> molecules.

## 7.2 Suggestions for future work

We now have a preliminary understanding of pressure effects on MOFs, their stabilities and CO<sub>2</sub> storage performance. Further experiments should help answer some unsolved questions from this work.

(1) *In situ* high pressure XRD would be a complimentary method to probe possible phase transitions of MOFs under high pressure. If single-crystal MOFs could be obtained, the single crystal XRD can not only monitor the structural changes of the frameworks, but also pinpoint the exact CO<sub>2</sub> adsorption sites in the frameworks at high pressures.

(2) More computational simulations can be performed to investigate the CO<sub>2</sub> storage in  $\alpha$ -Mg<sub>3</sub>(HCOO)<sub>6</sub> and CaSDB at high pressures to compare with the experimental work.

(3) All the current work was done under room temperature, at which CO<sub>2</sub> solidifies above 0.6 GPa. In the future, the MOFs loaded with CO<sub>2</sub> can be heated to higher temperatures to facilitate the diffusion of CO<sub>2</sub> at pressures higher than 0.6 GPa. As a result, even more CO<sub>2</sub> could be forced into the frameworks by pressure. A special heating device would be needed for the *in situ* high temperature measurements.



## Appendices: Copyright Permission

**RSC** | Advancing the  
Chemical Sciences

Royal Society of Chemistry  
Thomas Graham House  
Science Park  
Milton Road  
Cambridge  
CB4 0WF

Tel: +44 (0)1223 420 066  
Fax: +44 (0)1223 423 623  
Email: [contracts-copyright@rsc.org](mailto:contracts-copyright@rsc.org)

[www.rsc.org](http://www.rsc.org)

### Acknowledgements to be used by RSC authors

Authors of RSC books and journal articles can reproduce material (for example a figure) from the RSC publication in a non-RSC publication, including theses, without formally requesting permission providing that the correct acknowledgement is given to the RSC publication. This permission extends to reproduction of large portions of text or the whole article or book chapter when being reproduced in a thesis.

The acknowledgement to be used depends on the RSC publication in which the material was published and the form of the acknowledgements is as follows:

- For material being reproduced from an article in *New Journal of Chemistry* the acknowledgement should be in the form:
  - [Original citation] - Reproduced by permission of The Royal Society of Chemistry (RSC) on behalf of the Centre National de la Recherche Scientifique (CNRS) and the RSC
- For material being reproduced from an article *Photochemical & Photobiological Sciences* the acknowledgement should be in the form:
  - [Original citation] - Reproduced by permission of The Royal Society of Chemistry (RSC) on behalf of the European Society for Photobiology, the European Photochemistry Association, and RSC
- For material being reproduced from an article in *Physical Chemistry Chemical Physics* the acknowledgement should be in the form:
  - [Original citation] - Reproduced by permission of the PCCP Owner Societies
- For material reproduced from books and any other journal the acknowledgement should be in the form:
  - [Original citation] - Reproduced by permission of The Royal Society of Chemistry

The acknowledgement should also include a hyperlink to the article on the RSC website.

The form of the acknowledgement is also specified in the RSC agreement/licence signed by the corresponding author.

Except in cases of republication in a thesis, this express permission does not cover the reproduction of large portions of text from the RSC publication or reproduction of the whole article or book chapter.

A publisher of a non-RSC publication can use this document as proof that permission is granted to use the material in the non-RSC publication.



RightsLink®

Home

Create Account

Help



ACS Publications  
Most Trusted. Most Cited. Most Read.

**Title:** Evidence of Pressure Enhanced CO<sub>2</sub> Storage in ZIF-8 Probed by FTIR Spectroscopy  
**Author:** Yue Hu, Zhenxian Liu, Jun Xu, et al  
**Publication:** Journal of the American Chemical Society  
**Publisher:** American Chemical Society  
**Date:** Jun 1, 2013  
Copyright © 2013, American Chemical Society

LOGIN

If you're a [copyright.com](#) user, you can login to RightsLink using your [copyright.com](#) credentials. Already a [RightsLink](#) user or want to [learn more?](#)

#### PERMISSION/LICENSE IS GRANTED FOR YOUR ORDER AT NO CHARGE

This type of permission/license, instead of the standard Terms & Conditions, is sent to you because no fee is being charged for your order. Please note the following:

- Permission is granted for your request in both print and electronic formats, and translations.
- If figures and/or tables were requested, they may be adapted or used in part.
- Please print this page for your records and send a copy of it to your publisher/graduate school.
- Appropriate credit for the requested material should be given as follows: "Reprinted (adapted) with permission from (COMPLETE REFERENCE CITATION). Copyright (YEAR) American Chemical Society." Insert appropriate information in place of the capitalized words.
- One-time permission is granted only for the use specified in your request. No additional uses are granted (such as derivative works or other editions). For any other uses, please submit a new request.

BACK

CLOSE WINDOW

Copyright © 2015 [Copyright Clearance Center, Inc.](#) All Rights Reserved. [Privacy statement.](#) [Terms and Conditions.](#) Comments? We would like to hear from you. E-mail us at [customercare@copyright.com](mailto:customercare@copyright.com)

## Curriculum Vitae

**Name:** Yue Hu

**Post-secondary Education and Degrees:** The University of Western Ontario  
London, Ontario, Canada  
2010-2015 Ph.D. candidate (Chemistry)

Anhui University  
Hefei, Anhui, China  
2005-2009 B.Sc. (Materials Chemistry)

**Honours and Awards:** International Graduate Student Scholarship (UWO)  
2010-2015

Western Graduate Research Scholarship (UWO)  
2010-2015

Excellent Student Scholarship (Anhui University)  
2006-2009

**Related Work Experience** Teaching Assistant/Research Assistant  
The University of Western Ontario  
2010-2015

### Publications:

1. **Hu Y.**, Lin B., He P., Li Y., Huang Y., Song Y., The structural stability of and enhanced CO<sub>2</sub> storage in MOF MIL-68 (In) under high pressures probed by FTIR spectroscopy. *Chemistry - A European Journal*, **2015**, submitted.
2. Mao H., Xu J., **Hu Y.**, Huang Y., Song Y., The effect of high external pressure on structure and stability of MOF  $\alpha$ -Mg<sub>3</sub>(HCOO)<sub>6</sub> probed by in situ Raman and FTIR spectroscopy. *Journal of Materials Chemistry A*, **2015**, 3, 11976.
3. **Hu Y.**, Liu Z., Xu J., Huang Y., Song Y., Evidence of pressure enhanced CO<sub>2</sub> storage in ZIF-8 probed by FTIR spectroscopy. *Journal of the American Chemical Society*, **2013**, 135, 9287.
4. **Hu Y.**, Kazemian H., Rohani S., Huang Y., Song Y., In situ high pressure study of ZIF-8 by FTIR spectroscopy. *Chemical Communications*, **2011**, 47, 12694.

**Presentations:**

1. High-pressure study of CaSDB and its performance for CO<sub>2</sub> storage by vibrational spectroscopy; poster presentation, Ottawa, CSC **2015**.
2. The stability and enhanced CO<sub>2</sub> storage of MIL-68 (In) under high pressure; oral presentation, Niagara Falls, NANO-7, **2014**. / poster presentation, Quebec city, CSC **2013**.
3. CO<sub>2</sub> storage of ZIF-8 at high pressures; oral presentation, Calgary, CSC **2012**.
4. *In situ* high-pressure study of ZIF-8 by FTIR; oral presentation, Montreal, CSC **2011**.